INVESTIGATION OF CONVERTED-WAVE SEISMIC REFLECTION FOR IMPROVED RESOLUTION OF COAL STRUCTURES

ACARP PROJECT C10020

FINAL REPORT
October 2003

Prepared by

Velseis Pty Ltd

83 Jijaws Street, Sumner Park, Qld. 4074
P.O. Box 118, Sumner Park, Qld. 4074, Australia
Phone: (617) 3376 5544 **Fax:** (617) 3376 6939
Email: velseis@velseis.com.au
ABN 56 009 809 544

Velseis

Integrated Seismic Technologies

EXECUTIVE SUMMARY

Seismic reflection is widely recognised as a significant geophysical tool for remote imaging of sub-surface coal deposits. The technique is now often an integral part of mine planning, with positive contributions to mine productivity and safety. However, the desire to image increasingly subtle features is stimulating research into new seismic technologies which have the potential to enhance geological characterisation of the sub-surface.

One such novel technique is converted-wave (or PS-wave) seismic reflection. Theory and numerical modelling suggest that when a compressional (P) wave from a conventional seismic source (e.g. dynamite, Vibroseis, MiniSOSIE) strikes a coal seam, a significant fraction of the energy can be reflected back toward the surface as a shear (S) wave. Conventional seismic reflection ignores the occurrence of such P-to-S mode conversion, and records only the vertical component of ground motion to detect reflected P-wave energy. Consequently, this single-component mode of acquisition disregards the potential contaminating effects of PS waves, and ignores the additional information contained in the mode-converted energy.

Converted-wave seismic reflection aims to detect and exploit the available complementary S-wave information. The conventional vertical geophone is replaced with a multi-component geophone, capable of recording all incoming energy in a true vector sense. This provides the capability to discriminate between arriving P and PS waves. Over the past five years, converted-wave technology has been embraced by the petroleum seismic industry, with several striking successes including improved structural imaging, lithological classification, and fracture characterisation. To date there has been no significant practical assessment of the technology in the coal environment.

This ACARP project represents the first examination of converted-wave technology in the Australian coal context. Two field data trials have been conducted at sites having contrasting geological character. These multi-component seismic experiments have used a conventional dynamite source with purpose-built, high-resolution, multi-component sensors replacing the conventional arrays of vertical geophones. Specialised processing algorithms, designed to compensate for the highly-variable S-wave velocities in the near surface and the asymmetric raypaths of PS waves, have been implemented to yield PS images in parallel to conventional P images.

Trial Dataset #1 was acquired in an area with a shallow, thick coal seam. As predicted by theory, strong converted waves were detected. A number of significant processing issues were addressed to yield a viable converted PS image. The PS image validates structure seen on the standard P-wave image. Perhaps the most exciting result from Trial #1 is that the PS image shows an apparent improvement in vertical resolution when compared to the P-wave image. This significant result supports previous theoretical predictions that PS resolution advantages would be more likely in the shallow environment than at the petroleum scale.

Trial Dataset #2 was acquired over contrasting multi-seam geology. Here, the near surface was found to be much more attenuative, such that in this case no resolution advantage was seen on the PS image. Nevertheless, a viable PS image was extracted, providing additional control of structures interpreted on the P-wave image. Although the primary focus of this project has been on structural imaging, an interesting 'lithological' opportunity emerged via the integrated analysis of the P and PS

images from Trial #2. This has yielded a subsurface map of Poisson's Ratio. This attribute is believed to relate to lateral variations in lithology (e.g. sand vs. shale), and could prove significant for mine planning.

The overall objective of this research has been to demonstrate the viability of using converted-wave seismic technology in the coal environment, and to assess its potential in terms of enhanced sub-surface imaging. The results achieved in this first study provide a compelling argument that converted-wave reflection can evolve to be a cost-effective enhancement to conventional seismic imaging. From an acquisition viewpoint the technology is attractive in that relatively minor adjustments to current practice are needed. The development of a robust and cost-effective processing methodology is seen as a greater challenge. Prior geophysical history would, however, suggest that this will be achieved with further experience.

Future research should be aimed at understanding PS-wave propagation behaviour, tuning processing algorithms to improve PS image resolution, and demonstrating the practical implications of integrated P and PS interpretation. Such research will stimulate additional methodological advances, and ultimately lead to the use of converted-wave seismology as a standard coal-imaging tool.

Acknowledgements

Velseis Pty Ltd would like to acknowledge the following organisations for their support of this research:

- Australian Coal Association Research Program (ACARP)
- Anglo Coal Australia Pty Ltd
- Anglo Coal Capcoal Mine
- Bowen Basin Geologists Group (BBGG)
- MIM Exploration
- NCA Project - Newlands Coal Mine

Thanks must also go to the ACARP industry mentors – Greg Poole (BHP) and Andrew Willson (Anglo Coal) for their support of this project.

Velseis also acknowledges the Centre for Wave Phenomena, Colorado School of Mines for the development and distribution of Seismic Unix – a free research and seismic processing package.

TABLE OF CONTENTS

LIST OF FIGURES

LIST OF TABLES

CHAPTER ONE
INTRODUCTION

1.1 Introduction

Seismic reflection is becoming the preferred geophysical tool for accurate and cost-effective imaging of the coal seam (e.g. Greenhalgh et al., 1986; Henson and Sexton, 1991; Urosevic et al., 1992; Hatherly et al., 1998; Walton et al., 1999; Gochioco, 2000; Tselentis and Paraskevopoulos, 2002), and is of significant importance to the economics of longwall mining. Advances in 2D and 3D high-resolution seismic acquisition and processing technologies have seen significant improvements in the efficiency and reliability of coal seismic over the past two decades. However, the desire to locate and characterise increasingly subtle structures and lithological features continues to drive research into alternative seismic technologies, including multi-component seismology.

Multi-component seismology and associated converted-wave imaging methods have received considerable attention in the petroleum sector. Remarkable advances have been made in multi-component acquisition and processing in recent years, and there are a number of examples where converted-wave seismic techniques have proven more successful than conventional seismic imaging methods. For example, multi-component seismology has been used to map low acoustic impedance contrasts (e.g. Hanson et al., 1999; MacLeod et al., 1999), image through gas-filled sediments (e.g. Barkved et al., 1999; Granli et al., 1999) or beneath salt and basalt bodies (e.g. Li et al., 1998; Kendall et al., 1998), improve lithology/fluid classification (e.g. Rognø, 1999; Engelmark, 2001), detect reservoir fracture systems (e.g. Lewis et al., 1991; Potters et al., 1999) and enhance the resolution of relatively-shallow seismic data (e.g. Dasios et al., 1999; Harris et al., 2000; Begay et al., 2000).

In contrast, there has been little effort devoted to converted-wave imaging in the coal sector. This is despite the early synthetic modelling work of Fertig and Müller (1978) which highlighted the potential of coal seams to generate strong converted waves. The existence of converted waves in the coal environment has been confirmed by more recent wave-propagation investigations in the Sydney Basin (Greenhalgh et al., 1986; Urosevic and Evans, 1996), and computer modelling based on realistic geological models of Bowen Basin coal prospects (Hearn and Hendrick, 2000). The broad aim of this project is to assess the feasibility of using converted-wave technology as a standard tool for improving sub-surface imaging in the coal environment.

This chapter provides a brief review of reflection seismology, and introduces a number of fundamental concepts associated with converted-wave seismic exploration. The project's primary objectives are identified, and an outline of the methodology used to complete this research is provided.

1.2 Review of Reflection Seismology

1.2.1 Seismic Waves

Seismic waves are sound waves. There are several types of seismic waves, including body waves, surface waves and air waves. In terms of seismic imaging of the sub-surface, the most important and useful seismic waves are body waves. Both compressional (P) and shear (S) waves are seismic body waves. P waves are longitudinal waves that have particle motion in the direction of travel. In contrast, S waves are transverse waves that have particle motion perpendicular to the direction of travel. Figure 1.1 is a schematic illustrating the ground vibrations associated with P and S seismic waves.

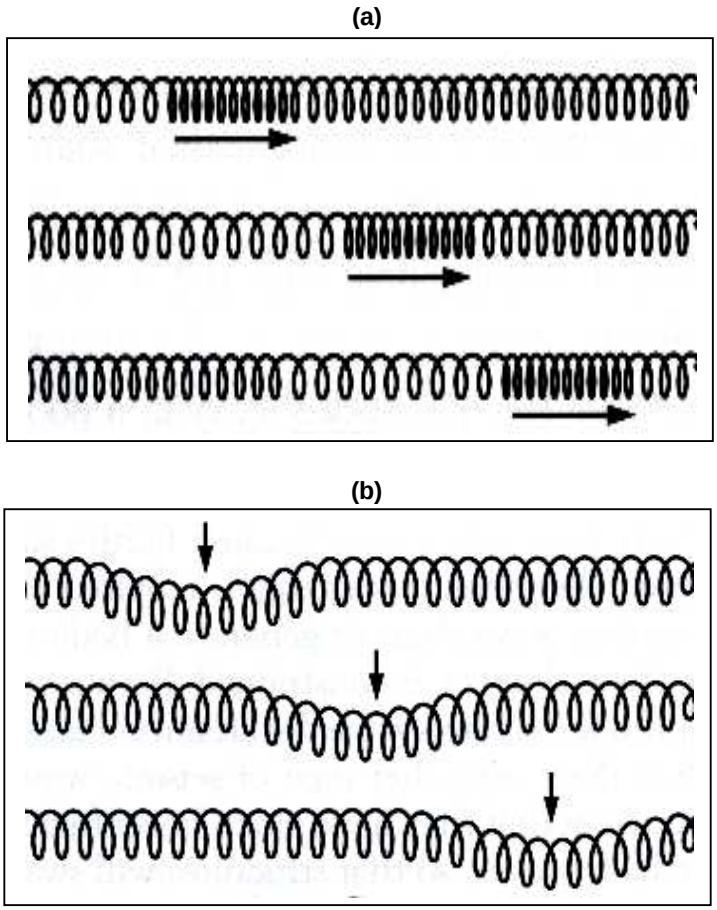

Figure 1.1 Ground vibrations associated with (a) P-waves and (b) S-waves. In this schematic, the seismic waves are travelling from left to right. The particle motion of the P wave is in the direction of travel. The particle motion of the S wave is perpendicular to the direction of travel.

Because of their different modes of propagation, P and S waves travel at different speeds through the earth, and respond differently to various geological situations. For example, S waves typically travel at about half the speed of P waves and hence may have shorter wavelengths. Unlike P waves, S waves only travel in solid materials, and hence are not influenced by pore space and/or fluid saturation. Such differences in behaviour make integrated use of P- and S-wave information potentially valuable for helping better understand sub-surface geology.

1.2.2 Conventional Coal-Seismic Reflection

In brief, seismic reflection involves imaging the sub-surface using artificially-generated sound waves. Typically, small dynamite explosions or vibratory sources (e.g. MiniSOSIE; Vibroseis) are used to generate seismic waves for coal exploration. Arrays of receivers (geophones) on the surface are used to detect the seismic energy that originates from the seismic source, travels down into the earth and gets partially reflected back to the surface at geological boundaries. Figure 1.2 illustrates the seismic reflection technique. The seismic waves recorded from a single seismic source make up a shot record. Figure 1.3 shows a typical coal-seismic shot record. Measuring the arrival times of the various seismic waves recorded by the surface geophones enables the sub-surface structure to be mapped. Further details on the conventional seismic reflection method can be found in standard texts (e.g. Sheriff and Geldhart, 1995).

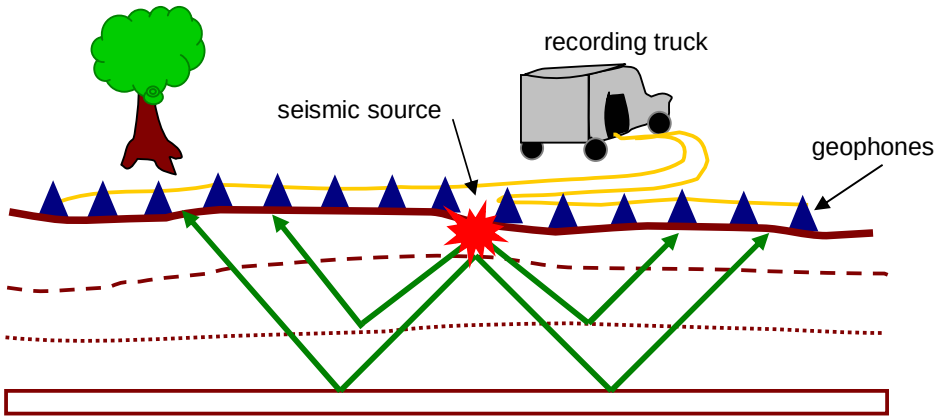

Figure 1.2 Schematic of the seismic reflection method. Artificially generated sound waves propagate down through the sub-surface, and get partially reflected back to the surface at geological boundaries. Arrays of receivers (geophones) detect the seismic energy at the surface.

The conventional approach to coal-seismic acquisition incorrectly assumes that typical coal-seismic sources will result in only P waves arriving at the surface. Recall that the particle motion of a P wave is in the direction of propagation. Hence a P-wave reflection travelling upwards from a geological boundary will have particle motion with a strong vertical component (Figure 1.4). Conventional seismic acquisition records only the vertical component of seismic energy arriving back at the receiver. This type of seismic recording can be referred to as single-component recording.

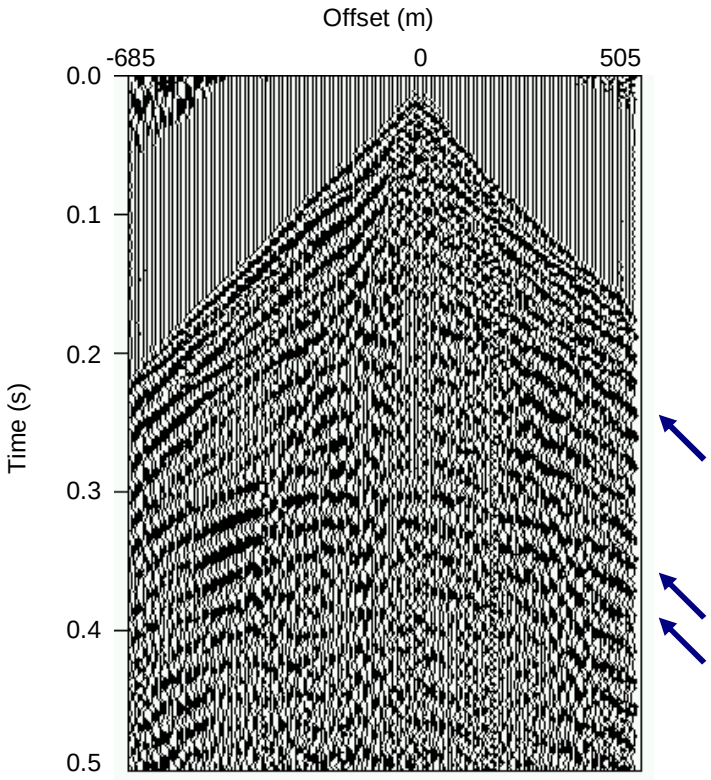

Figure 1.3 Typical coal-seismic shot record. The vertical axis is a measurement of the time it takes for the seismic energy to travel from the seismic source, down to a geological boundary and back to the surface (also referred to as two-way time). The horizontal axis represents offset, the distance between the source and each receiver station. Note that seismic energy travelling straight down from the source and back to the surface arrives earlier than energy that travels obliquely to receivers at far offsets. A number of representative reflection events (hyperbolic events) are indicated by the blue arrows.

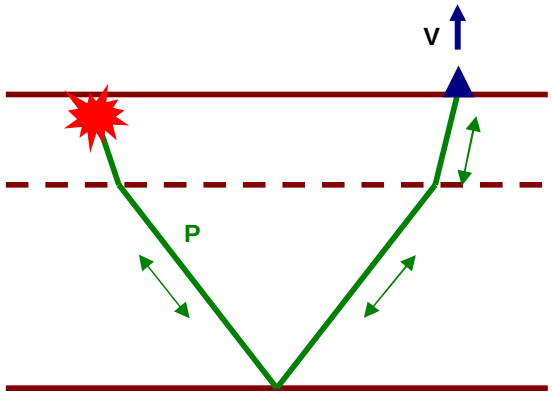

Figure 1.4 Conventional seismic reflection assumes that only P waves arrive at the surface. Since the particle motion of an upward travelling P wave is largely vertical (indicated by the green arrows), a vertically-oriented geophone responds well to reflected P waves. This type of recording is also known as single-component recording.

1.3 Fundamental Concepts of Converted-Wave Seismology

1.3.1 Multi-Component Recording

Converted-wave seismic technology takes advantage of the fact that, in reality, both reflected P and S waves typically arrive at the surface during a seismic survey. Since coal-seismic sources dominantly produce P-wave energy, most of the S energy arriving at the surface is in fact mode converted PS energy. That is, energy from a wave that travels down to a geological boundary as a P wave, gets partially converted to S energy at the boundary, and then travels back to the surface as an S wave. Any S-wave energy arriving at the surface will have a strong horizontal component of particle motion since the particle motion of an S wave is approximately perpendicular to its propagation direction (Figure 1.5). Multi-component seismic recording measures both the vertical and horizontal components of ground motion to enable exploitation of both P waves and PS waves arriving at the surface. Note that, multi-component recording may also be referred to as three-component (3-C) recording since the vertical and two orthogonal horizontal components (inline and crossline components) of ground motion are generally recorded.

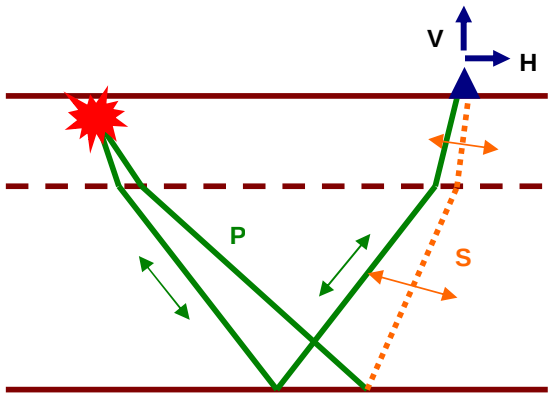

Figure 1.5 Multi-component seismic recording recognises that both P and mode-converted PS waves will arrive at the surface. The particle motion of an upward travelling S wave is largely horizontal (indicated by the orange arrows). Thus both the vertical and horizontal components of ground motion must be recorded to take advantage of both wave types.

1.3.2 Modelling of Converted-Wave Coal Seismic

Synthetic seismic modelling exercises (e.g. Fertig and Müller, 1978; Hearn and Hendrick, 2000) demonstrate that coal seams are efficient converters of P waves to S waves. Figure 1.6 illustrates the theoretically predicted amplitude of P and PS energy reflected back up from the top of a coal seam as a function of the angle of incidence of the downgoing P wave. For P-waves travelling almost vertically through the earth (i.e. small angles of incidence), very little conversion to PS energy occurs. Thus the amplitude of PS reflections from any geological boundary will be small. For angles of incidence in the range of 30° to 60°, the amplitude of the PS reflections from the top of a coal seam will theoretically be stronger than the amplitude of any reflected P energy. Converted energy of this magnitude can be expected on the mid- to far-offsets of a typical coal-seismic survey, and suggests that converted-wave acquisition in the coal environment should be particularly relevant.

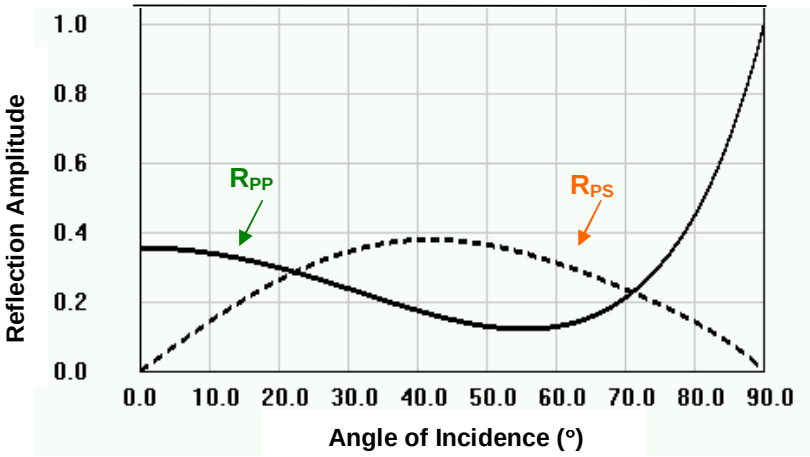

Figure 1.6 Theoretically predicted amplitude of P (R_{PP} - solid line) and converted PS (R_{PS} - dashed line) energy reflected from the top of a coal seam as a function of the angle of incidence of the downward propagating P wave. The parameters used to produce this modelled response are: upper layer – density = 2.0 g/cc; *Vp* = 3000 m/s; *Vs* = 1600 m/s; lower layer – density = 1.3 g/cc; *Vp* = 2200 m/s; *Vs* = 1050 m/s. These results have been generated using the CREWES Zoeppritz Explorer (www.crewes.org).

An alternative approach for studying the expected behaviour of P and PS reflections from the top of a coal seam is via synthetic seismic modelling. Figure 1.7 shows the vertical and inline components of a shot record generated for a simple, single-seam geology. As expected based on the discussion above, the P reflection from the top of the seam dominates the vertical-component record, while the converted PS reflection from the top of the seam dominates the horizontal-component record. Note that, as predicted by Figure 1.6, the P reflection from the top of the coal seam is very strong for offsets ranging from 0 m – 150 m (which, for this particular geological model, is equivalent to angles of incidence in the range of approximately 0° – 30°). In contrast, the PS reflection from the top of the coal seam has high amplitudes for offsets in the range 50m – 250m (which, for this particular geological model, is equivalent to angles of incidence in the range of approximately 15° – 50°). The earth model used to produce the synthetic data shown in Figure 1.7 is based on the known geology of the area in which our Trial Dataset #1 has been acquired. A comparison of the synthetic data in Figure 1.7 with a representative real shot record from this dataset (Figure 1.8) suggests that the P- and PS-wave behaviour predicted by numerical modelling is realistic.

Note that in both Figures 1.7 and 1.8, the PS energy arrives later than the P energy from the same geological boundary. This is because S waves travel slower than P waves along the upward raypath. This delay in arrival of S energy is potentially beneficial when mapping very shallow reflectors since the S reflection event may arrive after near-surface noise that is typically recorded on a real shot record.

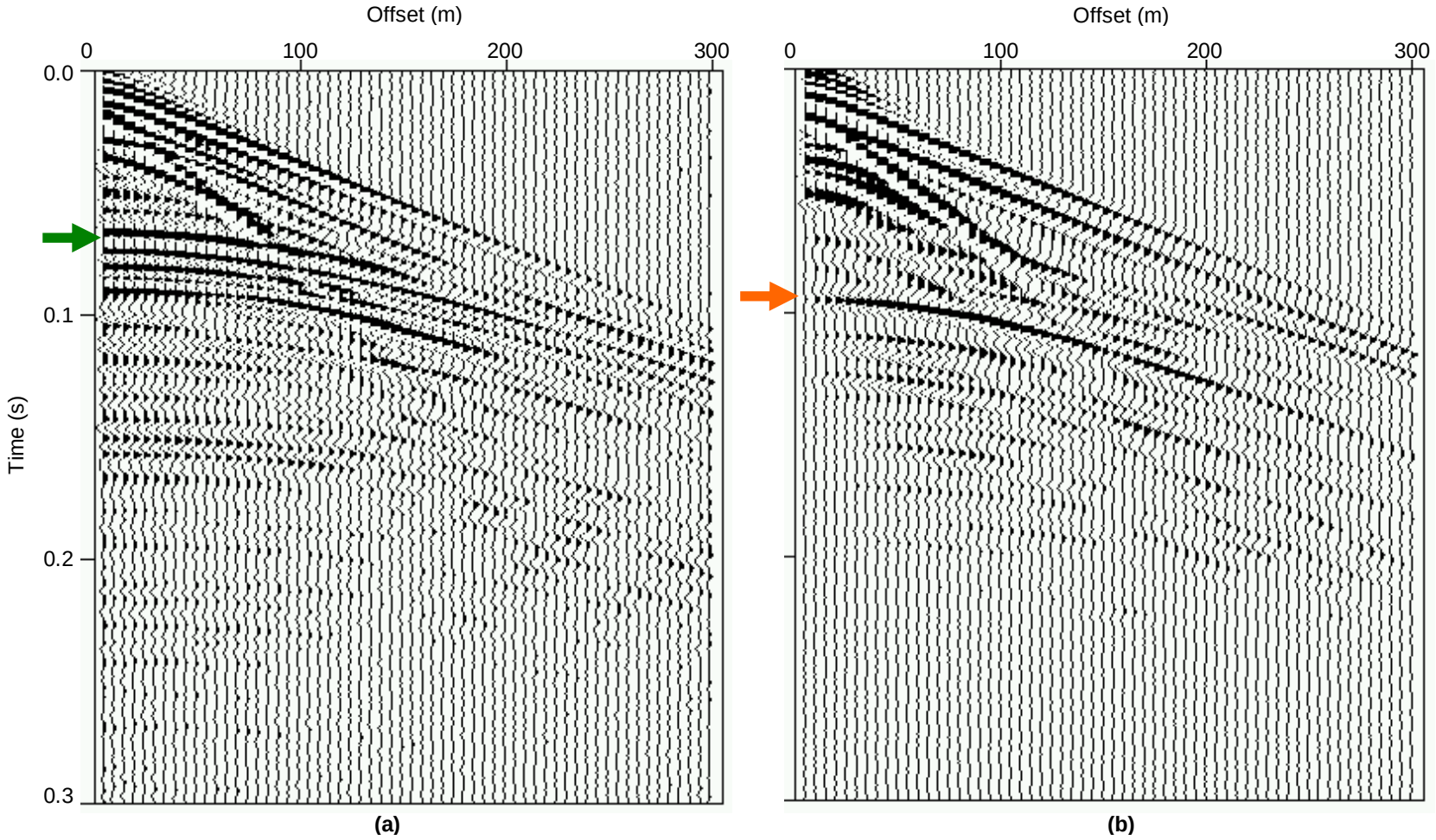

Figure 1.7 (a) Vertical component, and (b) inline component (horizontal component parallel to line of recording) of a synthetic shot record generated for a simple, single-seam geology. The P energy reflected from the top of the coal seam (green arrow) dominates the vertical component. The corresponding PS reflection event (orange arrow) dominates the horizontal component of data. The relative amplitudes of the P and PS reflection events as a function of offset are in agreement with those predicted by Figure 1.6.

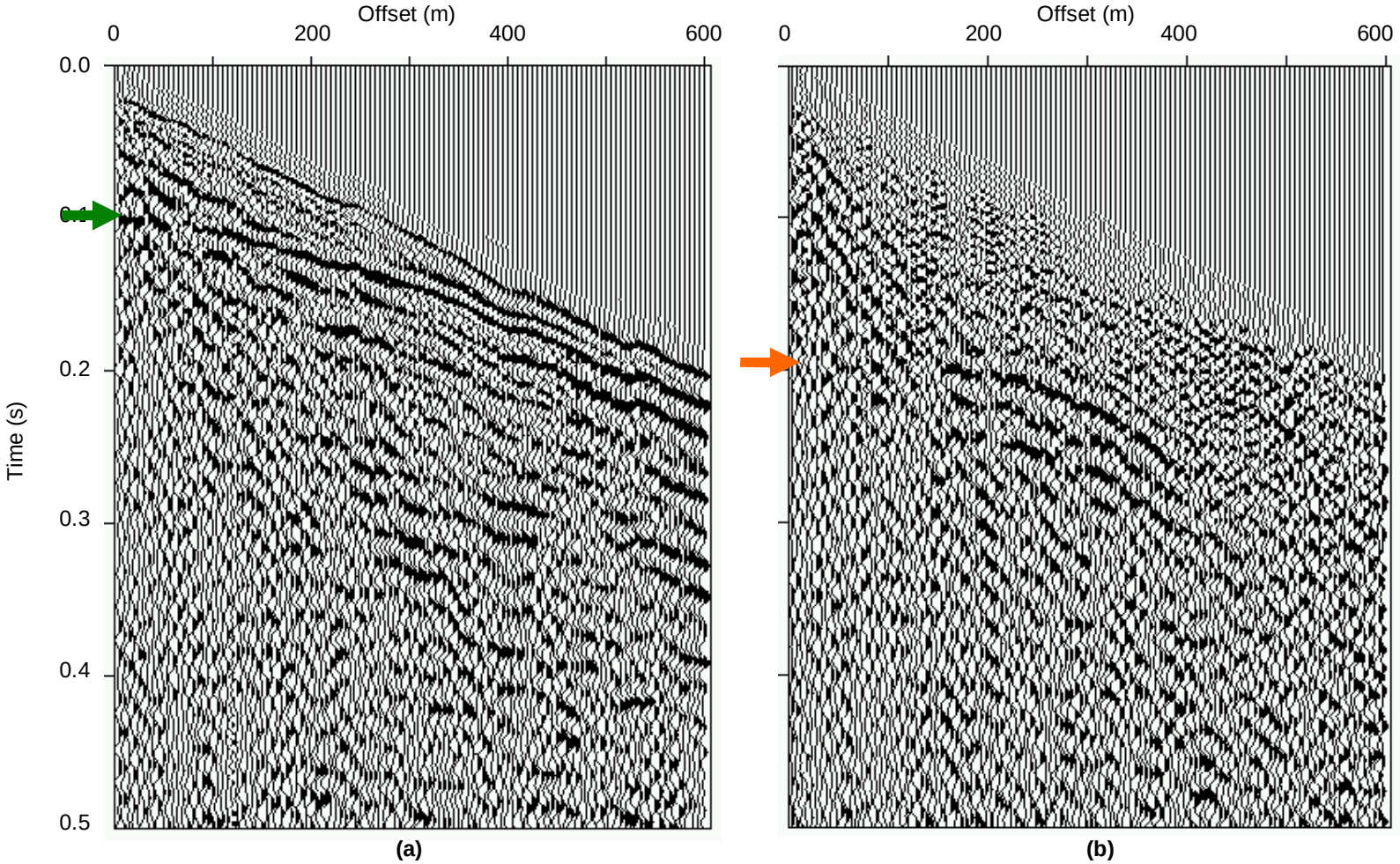

Figure 1.8 (a) Vertical component and (b) inline component of representative real shot record acquired in Trial Area #1, with a similar geology to that used to construct the synthetic shot record given in Figure 1.7. As predicted by numerical modelling, the P reflection from the top of the seam (green arrow) dominates the vertical component. The corresponding PS reflection event (orange arrow) dominates the inline component. The PS reflection energy has significant amplitudes between offsets 120 m – 400 m.

In some situations, cross-contamination of P energy onto the horizontal component and PS energy onto the vertical component can occur. There is evidence of weak wavefield cross-contamination in Figure 1.7. This generally occurs at far offsets where seismic raypaths are more oblique, and particle motion of P and S waves becomes more horizontal and vertical, respectively. Such cross-contamination is a source of interference, and could potentially degrade real P and PS seismic images. Multi-component seismic recording provides the opportunity for wavefield cross-contamination to be identified and eliminated (via vector-processing technology), leading to potentially cleaner seismic images.

1.3.3 Applications of Converted-Wave Seismology

The previous section has already highlighted the potential of converted-wave seismology to more accurately image very shallow targets and potentially produce cleaner images via removal of wavefield cross-contamination. In addition, the integrated interpretation of P and PS images has the potential to yield richer geological characterisation of the sub-surface. Modern seismic interpretation has two key objectives. '*Structural* interpretation' involves the mapping of geological interfaces and discontinuities (such as faults). PS images provide the opportunity to independently validate structures interpreted on conventional P-wave sections. In certain situations converted waves may even produce clearer or more coherent reflections than P waves to assist with structural interpretation. There is also potential for PS waves to have shorter wavelengths, and hence greater vertical-resolving power, than P waves at typical coal depths. This would enhance delineation of small features. The term '*Lithological* interpretation' is used here to describe efforts to extract more detailed geological character in terms of lithology, fluids, fractures etc. PS waves are typically more influenced by 'lithological' factors. This sensitivity has been exploited in the petroleum industry, where integrated interpretation has produced predictions of lithology, porosity, fracturing and the presence of fluid. By analogy, these applications suggest interesting possibilities for the coal environment, such as gas detection, mapping of sandstone lenses or channels, and detection of fracture swarms associated with very small faults or flexures.

1.4 Project Objectives and Methodology

This ACARP-sponsored project represents the first attempts in Australia to utilise shallow, high-resolution multi-component seismic data and converted-wave technology to image coal seams. Based on the above discussion, it is apparent that there are many aspects of converted-wave seismology that require testing in the coal environment. However, the logical starting point is to focus on demonstrating that acquisition of converted waves is viable in the coal environment, and PS images can be successfully produced and interpreted to provide independent structural information. It is envisaged that future research will need to be devoted to more advanced processing and lithological interpretation, to assess the full potential of converted-wave seismology for coal-seismic imaging.

Note that it is expected that converted-wave technology will ultimately be exploited as an enhancement to current 3D coal-seismic surveys. However, the geophysical concepts of converted-wave seismology can be most economically tested via 2D experiments, and this is the approach that has been taken here.

The specific objectives of this project have been to:

(i) demonstrate the viability of acquiring converted-wave data in one or more major Australian coalfields using a conventional dynamite source and three-component geophones;
(ii) demonstrate that the horizontal component(s) of seismic data can be processed to produce a converted-wave seismic image;
(iii) investigate the application of the converted-wave data in terms of validating coal structures seen on the conventional P-wave image;
(iv) investigate the removal of interfering converted-wave energy recorded on the vertical geophone so as to obtain a cleaner, conventional P-wave image.

These objectives have been achieved using the following methodology:

(i) construction of high-resolution, three-component geophones, and modification of field instrumentation for multi-component recording;
(ii) acquisition of two trial 2D multi-component datasets from coal mines exhibiting different geological characters;
(iii) implementation and testing of converted-wave processing software;
(iv) converted-wave processing of the two trial 2D multi-component datasets;
(v) investigation of wavefield separation techniques (including vector-processing technology) designed to remove PS-wave cross-contamination for cleaner conventional P-wave images.

A number of Velseis Pty Ltd staff and a University of Queensland student have been involved in conducting this research. The research team members who have contributed to this project are listed in Appendix A.

The practical aspects of acquiring the two trial multi-component datasets are discussed in Chapter 2 of this report. A brief review of basic converted-wave processing techniques is presented in Chapter 3. Additional mathematical details on converted-wave processing algorithms are included in the relevant appendices. Results from the investigation into using wavefield separation techniques for removal of interfering converted-wave energy to produce cleaner P-wave images are also summarised in Chapter 3. Work on this latter topic has been completed as a University of Queensland Honours Project. Analyses of the two trial multi-component datasets are described in Chapters 4 and 5. Practical procedures required to optimise basic converted-wave processing for these shallow, high-resolution datasets are discussed. In addition, preliminary observations regarding the interpretability of the resultant converted-wave sections are included. The significant conclusions drawn from this research, together with recommendations for future research and development, are presented in Chapter 6. A list of references and a glossary of terms complete the report.

CHAPTER TWO
MULTI-COMPONENT SEISMIC ACQUISITION

2.1 Introduction

Multi-component seismic acquisition typically involves recording the seismic wavefield with tri-axial sensors whose elements are oriented in mutually orthogonal directions. This enables the geophone to respond to ground vibrations from both P and S waves. A brief history of multi-component surface seismic acquisition methodology is given by Garotta (1999) and Stewart et al. (2002). This chapter provides a summary of the work undertaken to construct the high-resolution, multi-component geophones used for this project, as well as discussing practical issues associated with acquiring good-quality 2D multi-component seismic data. Note that many of these field practices will translate directly to 3D multi-component seismic acquisition.

2.2 Field Equipment

Converted-wave seismology is an efficient acquisition strategy which can accommodate both P-wave and PS-wave recording through use of conventional P-wave seismic sources (e.g. dynamite). In this way only minimal changes to conventional recording equipment and procedures are required to take advantage of PS energy arriving at the surface. The primary difference is the receiver device.

As part of this project, a total of 175 prototype three-component (3-C) geophones have been constructed by re-packaging a number of conventional high-resolution, high-output (40 Hz / 420 ohm) Geospace GS40D geophone elements. Initially, two different package designs were considered. The first of these was constructed as a hollow steel box structure, onto which the geophone elements were bolted. Although viable, this system was quite large, and relatively expensive. The preferred design (Figure 2.1) incorporates a solid module made from Delryn plastic with the three orthogonal geophone elements inserted into precision machined recesses. A total of three planting spikes have been incorporated into the design to make field deployment easier and to improve ground coupling.

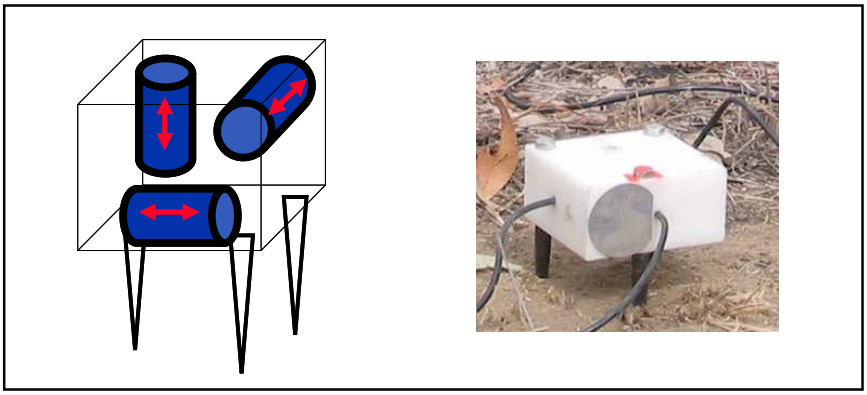

Figure 2.1 Final design for the prototype high-resolution three-component geophone. The design incorporates a solid module made from Delryn plastic with three orthogonal geophone elements inserted into precision-machined recesses. Three planting spikes on the base of the geophone ensure good surface coupling and torque resistance.

The prototype three-component geophones satisfy the '*multi-component acquisition polarity standard*' proposed by Brown et al. (2002). This is founded on a right-handed coordinate system: *z* positive downward; *x* (inline) positive in the forward line direction for a 2D survey; and *y* (crossline) positive in the direction 90° clockwise from *x*.

Velseis' VELCOM/348 recording system has been used to record the three-component seismic data. To facilitate use of the available conventional recording equipment, the vertical, inline and crossline components of the geophones were connected to separate lines, such that three coincident seismic lines were acquired simultaneously during recording. Note that for both trial 3-C surveys, an additional (fourth) line was used to record conventional seismic data. This provided the opportunity to compare P-wave data acquired using conventional geophone arrays versus single geophones. Although not formally a part of this project, results from one of these experiments are presented in Section 5.4.1.

2.3 Practical Acquisition Methodology

2.3.1 Geophone Planting

There are a number of key concepts that must be considered for acquisition of good-quality multi-component data. First, since multi-component geophones are designed to respond to ground vibrations in both the vertical and horizontal directions, the geophones must be aligned and planted carefully to ensure optimum recording. Our practical procedure involves planting geophones firmly using shock-proof hammers following removal of loose top soil. Bull's eye spirit levels ensure correct vertical orientation (Figure 2.2). The inline horizontal component is aligned manually along the direction of the 2D seismic line. Where seismic lines deviate from being straight, the inline horizontal component follows the actual seismic line. A true inline component (shot-receiver direction) can be derived during processing, if necessary, by mathematical rotation of the two horizontal components.

Figure 2.2 Planting of the multi-component geophones requires accurate alignment in both the vertical and horizontal sense to ensure optimum acquisition of both P and PS waves. Geophones are planted firmly using a shock-proof hammer following removal of any loose top soil. Bull's eye spirit levels are used to ensure correct vertical orientation.

2.3.2 Arrays versus Single-Geophone Recording

Conventional seismic acquisition uses receiver arrays to record the seismic energy arriving at the surface. This involves summing the seismic signals recorded by all geophones within the array. Traditionally, receiver arrays have been used to attenuate unwanted surface waves and boost the signal-to-noise ratio during recording. Typically, array lengths must be of the order of 20m – 30m to achieve optimum surface-noise attenuation. However, due to the varying effects of NMO and near-surface statics over the array length, such summation of the discretely sampled seismic wavefield can potentially degrade the recorded signal (Hearn and Hendrick, 2001). In contrast, single-geophone recording samples the propagating seismic energy at a single point.

Figure 2.3 illustrates the recording geometries associated with array and single-geophone recording. Synthetic seismic responses for the simple models shown in Figure 2.3 are given in Figures 2.4 and 2.5. For the situation modelled here, the distortion introduced by the long array (22m) may be acceptable, providing signal bandwidth lies below 100 Hz. These observations suggest that surface-wave attenuation via geophone arrays may be viable for petroleum seismic surveys. On the other hand, for high-resolution seismic exploration, where signal is expected up to 300Hz, geophone arrays cannot be used for surface-wave attenuation. It is common practice, however, for conventional high-resolution seismic exploration to use shorter geophone arrays simply to boost the signal-to-noise ratio. Figures 2.4 and 2.5 suggest that this will not compromise seismic resolution providing the geophone array length is less than or equal to 5m.

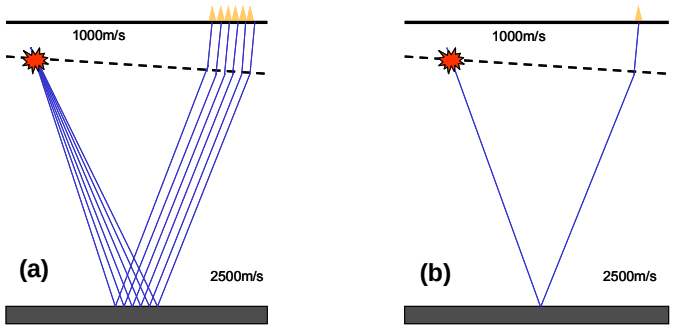

Figure 2.3 Schematic illustrating (a) conventional array recording and (b) single-geophone recording geometries. The simple two-layered earth model shown here has been used to generate the numerical results given in Figures 2.4 and 2.5. The near-surface layer is approximately 15 m thick, with the base of the layer dipping at approximately 10°. The target-reflector depth and receiver offset are 200 m.

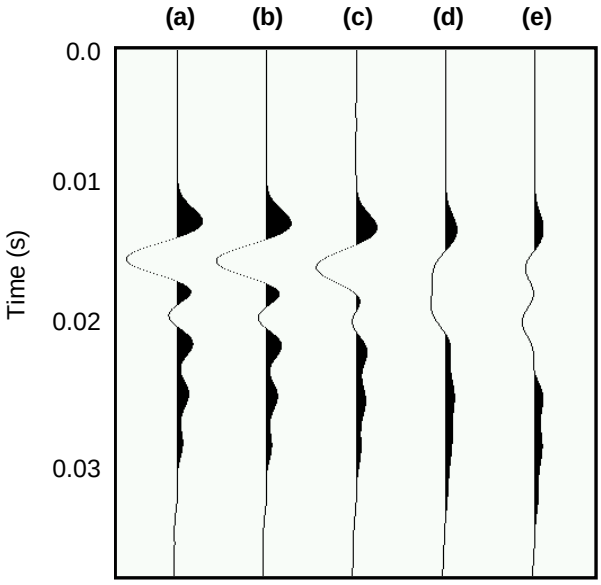

Figure 2.4 Synthetic modelling of the seismic response recorded by (a) a single geophone; (b) a group of 6 geophones over 2 m; (c) a group of 6 geophones over 5 m; (d) a group of 12 geophones over 11 m; and (e) a group of 12 geophones over 22 m. The two-layered earth model given in Figure 2.3, and a minimum-phase source wavelet of 15/30 Hz – 250/350 Hz, have been used to produce these synthetic results.

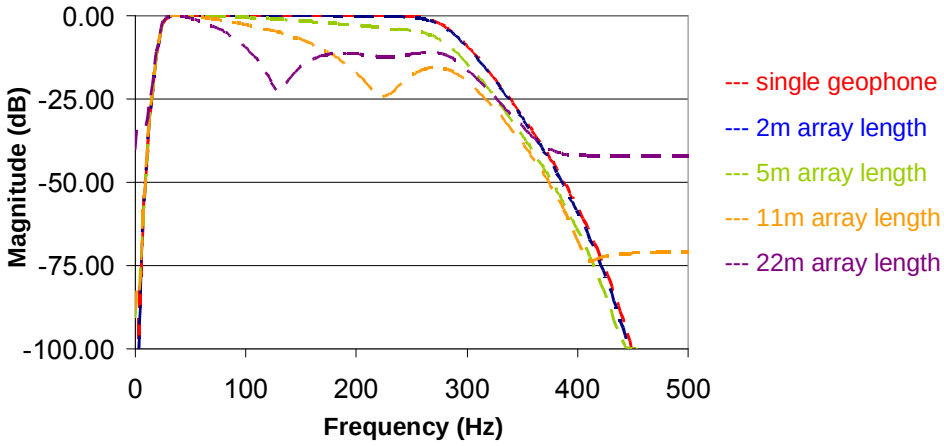

Figure 2.5 Magnitude spectra of the synthetic seismic responses given in Figure 2.4. The longer arrays introduce unacceptable distortion for typical coal-seismic applications which utilise frequencies up to 300 Hz.

The preceding analysis suggests that, for conventional P-wave recording, either single geophones or short arrays are viable. On the other hand, it is known that S waves are much more sensitive to lateral variations in the near surface. Hence, geophone arrays of any length can severely distort the S-wave energy arriving at the surface (e.g. Hoffe et al., 2002). Consequently, for acquisition of the trial multi-component datasets, only single 3-C geophones have been planted at each receiver station. As will be discussed further in Section 5.4.1, this single-geophone acquisition approach has not compromised the corresponding P-wave data. The response from high-output single geophones has been found to be comparable to that recorded using short geophone arrays.

2.3.3 Record Length

Due to the slower propagation of S waves in the sub-surface, it is necessary to increase the record length of multi-component data beyond what would typically be needed to image a target horizon using only P waves. For this project, 1 second of data at 1 ms sample interval has been acquired for target depths ranging from 150 m to 500 m.

2.3.4 Offset Range

Recall that Figure 1.6 demonstrates that P-to-S conversion at the top of a coal seam does not produce significant PS energy until the angle of incidence of the downgoing P wave increases beyond approximately 30°. Thus, to ensure optimum recording of PS energy, the multi-component seismic survey must be designed to record offsets for which the approximate angle of incidence extends well beyond 30°, and preferably beyond 60° (at which point the amplitude of the PS energy is expected to decrease). A general rule of thumb is that a maximum recording offset of at least one-and-a-half times the depth of the target seam should allow detection of any PS conversions.

CHAPTER THREE
CONVERTED-WAVE SEISMIC PROCESSING

3.1 Introduction

Processing of converted-wave seismic data involves a number of steps that are substantially different from, and significantly more challenging than, conventional P-wave processing. This chapter gives an overview of those converted-wave processing steps that differ most from conventional P-wave methods. A basic understanding of conventional P-wave processing is assumed (see Yilmaz (1987) for details of P-wave processing). Mathematical details of critical PS processing steps are given in Appendix C. Any data-specific processing idiosyncrasies and details of the full PS processing sequences used for the real-data trials will be discussed in Chapters 4 and 5. Further information regarding all aspects of converted-wave processing can be found, for example, in Harrison (1992), Garotta (1999) and the CREWES Research Collection (2002).

Note that prior to commencing processing of any converted-wave data it is assumed that a corresponding conventional P-wave section has been produced from the vertical component of data. Details of the conventional P-wave processing sequence are not discussed here. However, a flowchart outlining the general approach to P-wave processing, together with a flowchart summarising the approach taken here for converted-wave processing, are given in Appendix B.

For this project, processing of the multi-component data has been undertaken on Linux PCs and software has been implemented within the Seismic Unix framework (Cohen and Stockwell, 2002).

3.2 Converted-Wave Processing

3.2.1 Horizontal Component Rotation

In an isotropic earth with flat, homogeneous layers, all mode-converted S-wave energy would be recorded only on the inline component, with perhaps some cross-contamination onto the vertical component (see Section 3.3 for further discussion regarding P/PS wavefield cross-contamination). In reality the earth is anisotropic (e.g. thin-layered sedimentary sequences, or near-vertical fractures striking at an angle to the seismic line). Some forms of anisotropy may lead to rotation and/or splitting of the S-wave energy, which in turn can cause the S energy to be recorded on both the inline and crossline components of data. In addition, any misalignment of the 3-C geophones during acquisition can also result in S energy being recorded on both the inline and crossline components of data. Mathematical rotation of the 3-C data can be performed to compensate for these effects and essentially force the desired PS energy back onto the inline component. See, for example, Thomsen (1988), and MacBeth and Crampin (1991) for more in-depth discussions.

3.2.2 Polarity Reversal of Trailing Spread

For an isotropic earth with flat, homogeneous layers, the particle-motion of any PS mode conversions will exhibit radial symmetry about the source location. Consequently, any S-wave

energy recorded by geophones positioned on opposite sides of a split-spread will have opposite polarity. To compensate for this, the polarity of the inline data recorded on one side of the spread, typically the trailing direction, is reversed for each shot record.

3.2.3 Static Corrections

Statics are the time delays introduced in the seismic data due to the varying thickness of the low-velocity weathering layer. The recorded seismic wave will pass through the weathering layer twice – once on the way down as a P wave, and once on the way up, as either a P or S wave.

Source static corrections are required to compensate for delays associated with the P wave travelling down through the weathering layer from the source. Since the source statics will be the same for both the P wave and PS wave data, source static corrections for the inline data are computed using the vertical component of data and conventional P-wave static techniques (e.g. Yilmaz, 1987).

In the processing of converted-wave data, receiver statics are required to compensate for delays associated with the S wave travelling up through the weathering layer to the surface (Figure 3.1). The S receiver statics are generally not related in any way to the conventional P-wave receiver statics. This is largely due to the difference in effective thickness of the near-surface low-velocity layer that the P and S waves 'see', and the fact that S velocities in the surface layer can be up to ten times smaller than for P waves. In practice, not only will S receiver statics typically be much larger than P-wave receiver statics, they can also vary more from location to location.

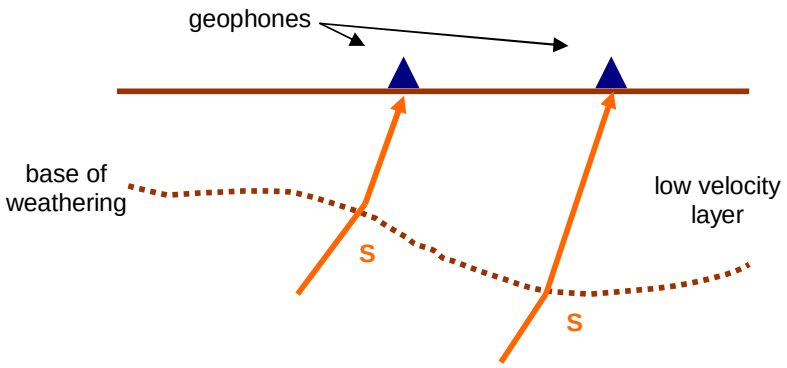

Figure 3.1 S-wave receiver statics are delays introduced at each receiver due to the varying thickness of the low-velocity weathering layer. For the situation illustrated here, the S energy arriving at the right-hand geophone will arrive at a later time than the energy at the left-hand geophone since it must travel through a thicker layer of low-velocity material to reach the surface. The S-wave receiver statics generally differ from the P-wave receiver statics due to the significantly lower S-wave velocities in the weathering layer, and the influence of any near-surface water table. Recall that S waves will only travel through solids, and are therefore not influenced by fluid saturation. P waves, on the other hand, will have their propagation speeds influenced by the presence of ground water.

Two different approaches to computing S-wave receiver statics have been trialed in this project. Both use the common-receiver gather (CRG) stack generated from the inline component of data. The CRG stack is created using a brute *Vp*/*Vs* function (where *Vp* = P-wave velocity and *Vs* = S-wave velocity) and the non-hyperbolic PS normal moveout (NMO) equation (discussed in Section 3.2.4 below). Since the shot statics are negligible after applying the conventional P-wave shot static correction, the CRG stack can give a very clear indication of any receiver statics. Any time delay associated with the S energy travelling through the weathering layer to a particular receiver will be common to all traces in the related CRG. Thus the time shift between traces on the CRG stack will be representative of the relative receiver statics. The first approach for computing these statics is to simply hand pick the time shifts along the CRG stack. The second approach uses the automatic CRG stack-power optimisation method of Cary and Eaton (1993). While the automated approach is more desirable, it has been revealed through the course of this research that it is quite susceptible to cycle-skipping in noisy data. Hence, despite being labour intensive, the hand picking method for computing receiver statics is now our preferred approach.

Note that both of these approaches to receiver static computation make the assumption that there is very little structure and/or dip along the PS reflection event being used to pick the receiver statics from the CRG stack. This is not always the case for coal-seismic data. Consequently, the approach used here has been to include an additional step when constructing the CRG stack. The two-way time structure from the conventional P-wave image, scaled by a suitable average *Vp*/*Vs*, is used to remove all known structure and dip from the PS-wave CRG stack prior to any static computations. In this way, structure and dip within the PS section can be preserved.

3.2.4 PS Velocity Analysis and Normal Moveout (NMO) Correction

Normal moveout (NMO) is the offset-dependent variation of traveltime for any given reflection event. NMO corrections compensate for this variation in traveltime to ensure reflection energy from each geological boundary is properly aligned prior to stacking. The significant difference between conventional P-wave NMO and PS-wave NMO relates to the non-hyperbolic moveout of PS reflection events (see Appendix C for further details). In addition, some knowledge of both the P-wave and S-wave velocity is necessary to apply PS NMO corrections. P-wave velocities (*Vp*) are extracted from conventional P-wave processing of the vertical component of data (e.g. Yilmaz, 1987). Velocity analysis of converted-wave data is focused on recovering S-wave velocities (*Vs*), or equivalently the P-wave to S-wave velocity ratio (*Vp*/*Vs*). Note that since all subsequent converted-wave processing stages are generally formulated in terms of *Vp*/*Vs*, velocity analyses of the two trial datasets considered here involve the direct recovery of *Vp*/*Vs*. Once the relevant equations for NMO have been substituted into the velocity analysis software, the practical methodologies used for picking *Vp*/*Vs* are the same as those used for picking the P-wave velocity. Methods such as semblance analysis and constant *Vp*/*Vs* stacks (analogous to constant-velocity stacks) (e.g. Yilmaz, 1987) have been used in this project.

3.2.5 Common-Conversion Point (CCP) Binning

Regardless of whether P-wave or PS-wave data are being processed, the final stacked section is produced by summing together all traces originating from the same sub-surface reflection point.

P-wave raypaths are approximately symmetric and so the reflection point for each vertical-component trace is the midpoint between its corresponding shot and receiver locations. Thus the collection of P data into common-reflection point gathers is termed common-midpoint (CMP) binning. In contrast, the raypath of a PS wave through the sub-surface is asymmetric. This is due to the fact that the upcoming S wave travels more steeply than the downgoing P wave as a result of Snell's Law (e.g. Sheriff and Geldart, 1995) having to be satisfied at the conversion boundary. Consequently the reflection point of a PS wave is offset from the midpoint of the shot and receiver, towards the receiver. The precise location of this reflection point is actually a function of *Vp*/*Vs*. Furthermore, the location of the reflection point will vary with the depth of the reflector (Figure 3.2). As a result of this asymmetry, a different trace-binning technique is required to sort PS data into common reflection point gathers – also know as common-conversion point (CCP) gathers. The mathematical expression for determining the PS CCP is given in Appendix C.

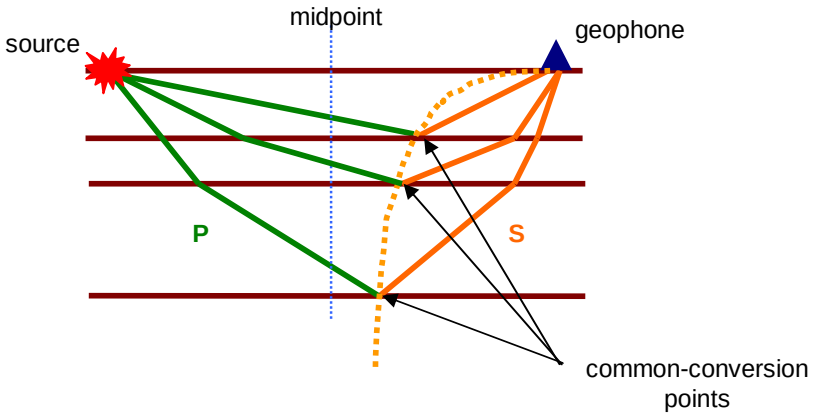

Figure 3.2 The reflection (or conversion) points of a PS wave travelling between a given source and receiver will vary with velocity and reflector depth.

Two different approaches to binning the PS data have been trialed in this project. The first, here referred to as 'horizon-based CCP binning', assumes that there is only one target horizon for which the traces must be optimally binned. The binning algorithm scans for the supplied two-way time of the target reflection event and the *Vp*/*Vs* at that two-way time on each trace, and computes the CCP for those specific parameters. Shallower and deeper reflectors will inevitably be smeared and mispositioned by this approach. The second approach to binning is more suitable when multiple reflection events must be accurately imaged, and is here referred to as 'dynamic CCP binning'. This latter approach bins each sample down each trace according to its two-way time and the local *Vp*/*Vs* value. Thus portions of seismic traces can be assigned to different CCP bin locations, and contribute to different traces in the final stacked section.

3.3 Vector Processing

The converted-wave processing steps discussed in the previous section make the assumption that the vertical component of data contains only P-wave energy, and the horizontal component(s) of data contain only PS-wave energy. However, as discussed in Section 1.3.2, there is potential for P waves to leak onto the horizontal components and S waves to leak on to the vertical component.

This is particularly evident when upcoming seismic raypaths are non-vertical (e.g. when recording far-offsets that are greater than the target depth). As mentioned previously, such cross-contamination might be expected to degrade the final P and PS images. One of the objectives of this project has been to investigate the removal of such interfering energy so as to obtain a cleaner seismic image. A University of Queensland Honours Project (Metcalfe, 2002) has investigated vector-processing techniques and assessed their potential for attenuating wavefield cross-contamination to improve P and PS imaging. Vector-processing methods make no assumptions about the particle motion of a seismic wavefield, and use the actual recorded particle-motion information to distinguish between P and PS waves. Vector-processing techniques are designed to be used prior to all other processing algorithms. In this way, pure P energy can be passed through the conventional P-wave processing sequence, and pure PS energy can be passed through the PS processing sequence.

Metcalfe's (2002) study has involved using the reflectivity modelling technique (e.g. Kennett, 1991) to construct a series of coal-specific synthetic seismic shot records. The conventional component-selection approach to multi-component wavefield separation is then compared to the vector-processing results, both before and after stacking of the data. For this study, a vector-processing technique referred to as Parametric Inverse Modelling (PIM) (Hendrick, 2001) has been used. In brief, the study found that vector processing is generally able to reduce wavefield cross-contamination and produce cleaner P- and PS-wave gathers compared to the corresponding vertical and inline gathers. This observed improvement in the gathers suggests that vector processing should improve the interpretability of any pre-stack seismic analysis, such as velocity analysis or amplitude-versus-offset (AVO) analysis. However, it transpires that the common-reflection point binning and stacking process is a very powerful tool for suppressing P- and S-wave cross-contamination. Thus, despite the vector-processed gathers appearing much cleaner than the corresponding vertical and inline gathers, the stack results show very little difference.

Representative results from this study are summarised in Figures 3.3, 3.4 and 3.5. Synthetic vertical and inline shot records are given in Figure 3.3. The top coal P reflection event dominates the near-offset traces of the vertical component of the data. The corresponding PS reflection event is dominant on the near- to mid-offset traces of the inline component. For this particular model, however, there is evidence of cross-contamination of P and PS energy onto the horizontal and vertical components, respectively. The pure P and PS wavefields extracted via vector-processing are shown in Figure 3.4. A comparison of Figures 3.3 and 3.4 demonstrates that vector processing has successfully attenuated wavefield cross-contamination. The resultant stacked traces from the gathers shown in Figures 3.3 and 3.4 are given in Figure 3.5. Despite differences observed in the pre-stack gathers, there is no significant difference between the pure P and PS stacks, and the vertical and horizontal component stacks. Thus, since the objectives of this project are focused on structural interpretation of stacked images, vector processing has not been incorporated into the processing sequences used in this project. It is likely, however, that the vector-processing approach may be relevant in future studies designed to extract lithological information from integrated P and PS interpretation, since pre-stack analysis could play a more vital role.

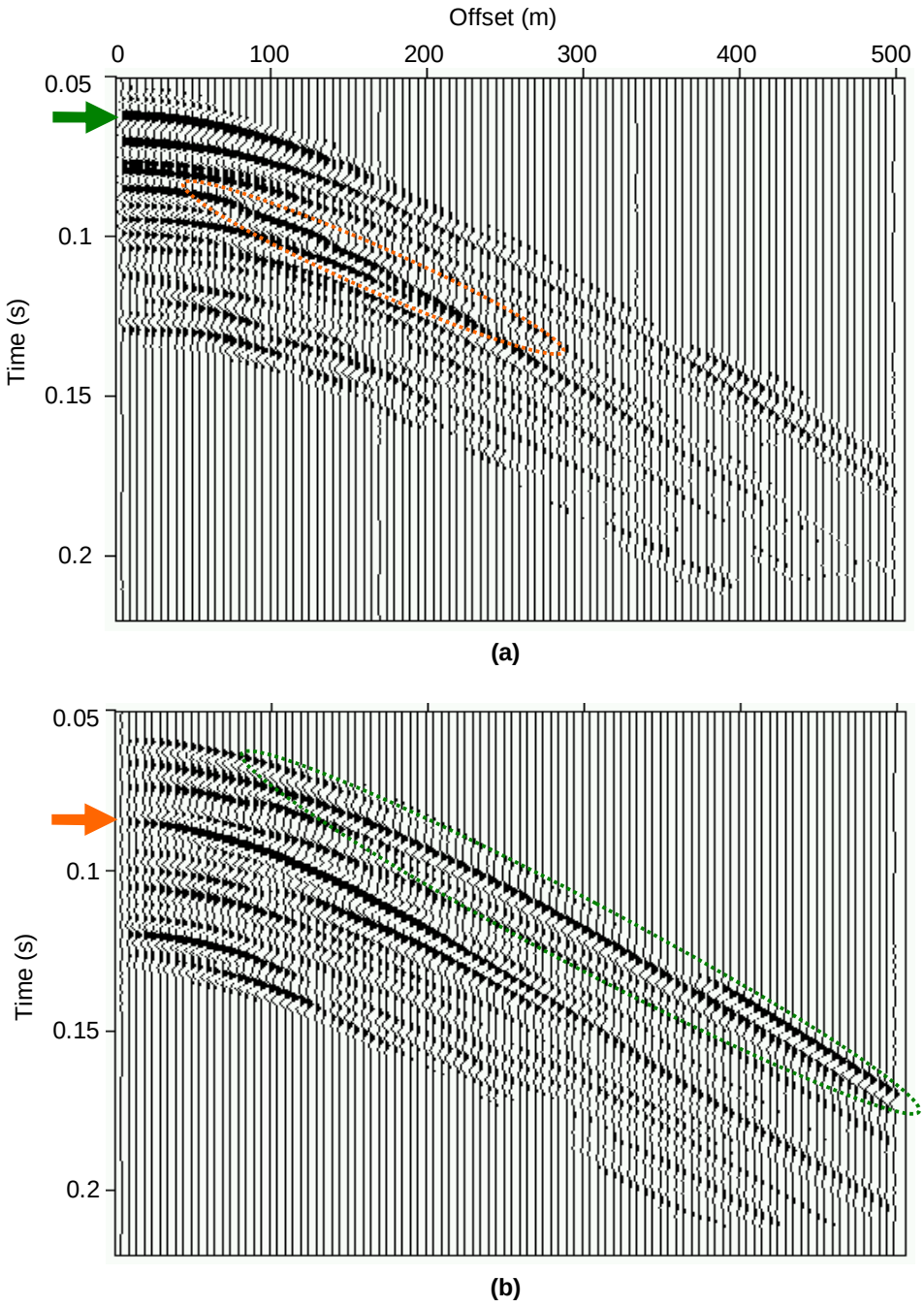

Figure 3.3 (a) Vertical component and (b) inline component of a synthetic shot record generated via the reflectivity method using a simple, single-seam geological model. Only reflection events about the time zone of interest are shown. The P reflection energy from the top of the seam (green arrow) is a dominant event on the near-offset traces of the vertical component. However, there is also significant P energy (green ellipse) on the far-offset traces of the inline component. Similarly, the top-coal PS reflection event (orange arrow) dominates the inline component on the near- to mid-offset traces. However, there is also weak contamination of PS energy (orange ellipse) on the mid-offset traces of the vertical component.

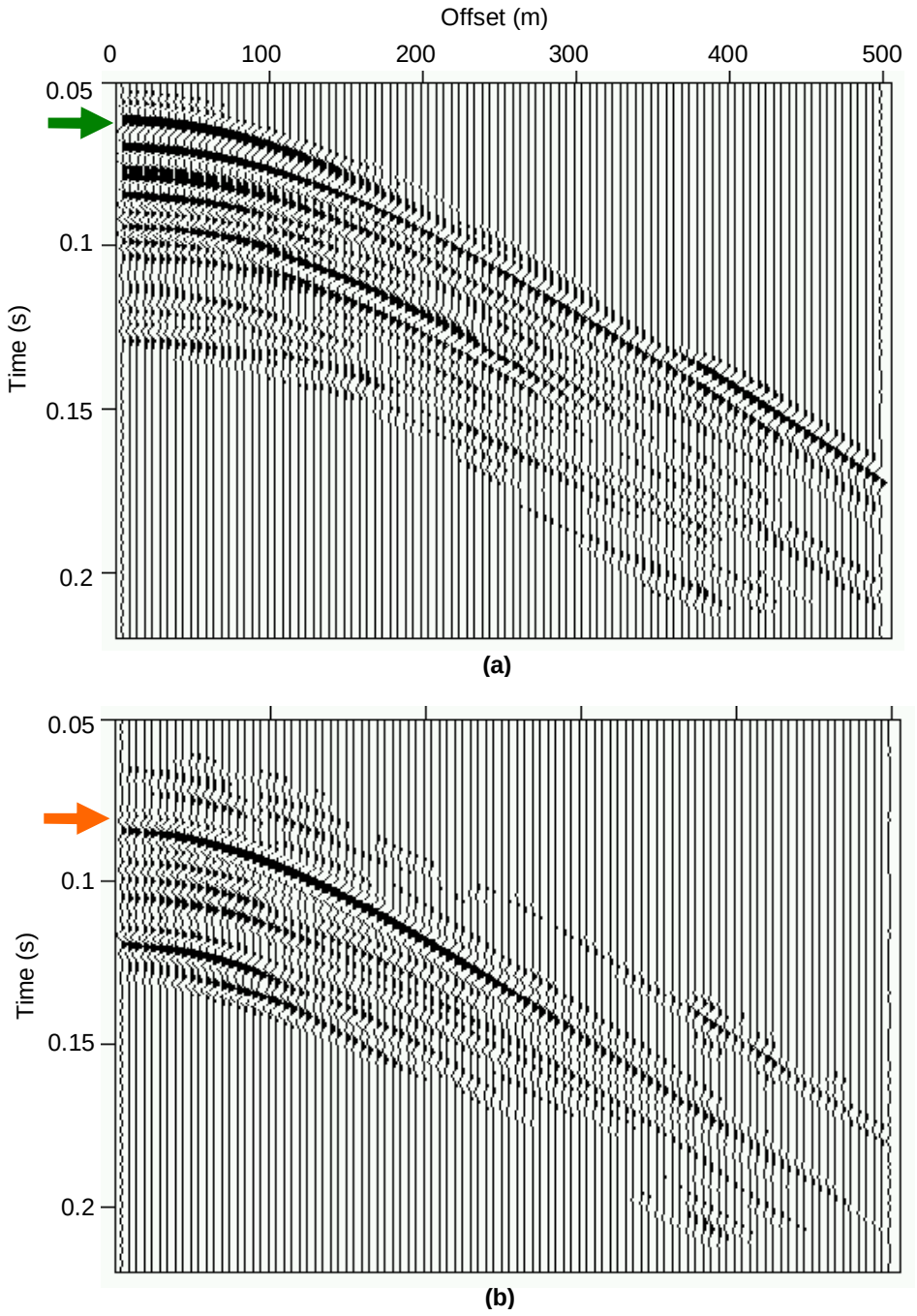

Figure 3.4 (a) Pure P-wave record and (b) pure PS-wave record extracted from the synthetic multi-component data given in Figure 3.3 via a vector processing method referred to as Parametric Inverse Modelling (Hendrick, 2001). The P and PS top coal reflection events are marked by the green and orange arrows, respectively. The cross contamination seen on Figure 3.3 has been successfully attenuated.

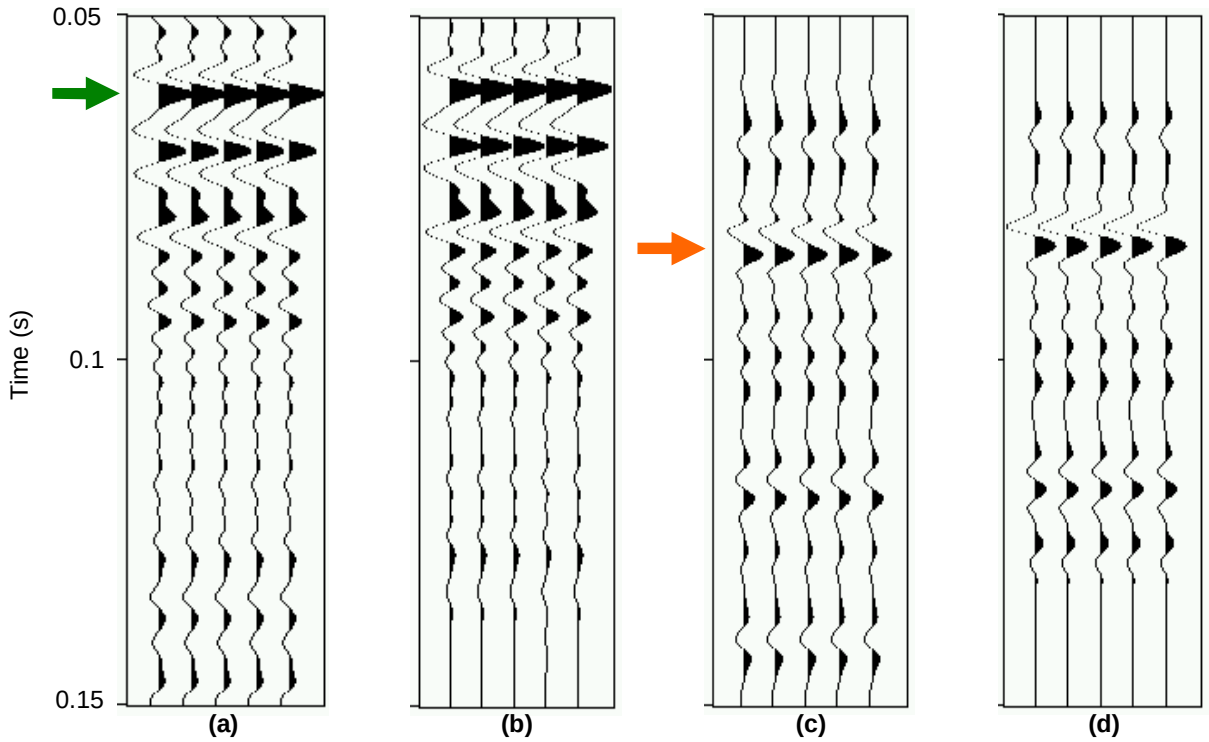

Figure 3.5 (a) Stacked image generated from the vertical component of the synthetic shot record shown in Figure 3.3(a); (b) stacked image generated from the extracted P-wave energy given in Figure 3.4(a); (c) stacked image generated from the inline component of data shown in Figure 3.3(b); and (d) stacked image generated from the extracted S-wave energy given in Figure 3.4(b). The P and PS top coal reflection events are marked by the green and orange arrows, respectively. The stacking process is a powerful tool for suppressing P/S cross contamination. Following stacking, there are no significant differences between the pure P and PS images and those generated from the vertical and horizontal components of data.

CHAPTER FOUR
REAL-DATA TRIAL #1

4.1 Introduction

The first multi-component field trial undertaken as part of this project represents the first attempt to record and process shallow, high-resolution, converted-wave data in the Bowen Basin, Queensland. The data have been acquired in an area that has a single, thick coal seam at relatively shallow depths. This test site was selected based on a comprehensive analysis of numerical modelling results. Synthetic multi-component records for this particular style of geology provided a high level of confidence for a successful PS imaging experiment. This chapter describes details of the acquisition and processing methodology used to produce the converted-wave section from this trial area. In addition, interpretation of the final P-wave and PS-wave sections is discussed.

4.2 Data Acquisition

Acquisition of Trial Dataset #1 was undertaken by Velseis Pty Ltd during September 2001 (Figure 4.1). The recording parameters are given in Table 4.1.

Table 4.1: Field acquisition parameters for Trial Dataset #1.

Recording System	Velcom 348
Line Length	1.2 km
Source	Dynamite 400g Booster
Source Depth	15-30 m
First / Last Shotpoint	124.5 / 364.5
Shotpoint Interval	10 m
Geophone	Conventional – SM4/7 30 Hz / 375 ohm Three-Component – GS40D 40Hz / 420 ohm
Receiver Array	Conventional – 6 geophones over 5m Three-Component – single geophone
Receiver Interval	5 m
Spread	Conventional – 120 channels split spread Three-Component – 120 channels x3 split spread
Near Trace	2.5 m
Far Trace	297.5 m
Nominal Fold	24
Data Format	SEGY
Sample Interval	1 ms
Record Length	1 s

Note that, as indicated in Table 4.1, conventional seismic data using single-component geophone arrays have been acquired in parallel to the multi-component data for this field trial. This provided opportunity to compare P-wave data derived from short-array and single-geophone recording. The integration of multi-component recording into standard seismic surveying practices is more favourable if single-geophone acquisition does not compromise the quality of the conventional P-wave data. The same experiment was conducted during the acquisition of the second trial dataset,

and a more detailed presentation of the results is given in Section 5.4.1. However, in summary, the P-wave data acquired via short-array and single-geophone recording are comparable.

Figure 4.1 Field acquisition of Trial Dataset #1 – laying out recording equipment (left) and a three-component receiver station (right).

Figure 4.2 illustrates representative vertical and inline shot records from the first trial multi-component dataset. It is immediately apparent that strong P-to-S conversion is occurring at the target coal seam. Note however, that the event coherency seen on this inline record is not typical. More typically, the raw inline shot records show poor reflection coherency due to severe receiver-related statics. Note also, that the inline record suffers from greater surface-related noise compared to the vertical record. As a consequence, it is expected that the final PS image may have a lower signal-to-noise ratio than the corresponding P-wave image. This is consistent with prior experience in the petroleum sector.

It is also of interest to examine the frequency content of the raw P and S recordings. Previous experiments, largely from the petroleum sector, suggest that S-wave reflection energy generally exhibits significantly lower frequencies than the corresponding P energy. Figure 4.3 shows a number of sample frequency spectra from the shot records given in Figure 4.2. The dominant frequency of the raw P signal is approximately 75 Hz, with the signal bandwidth extending from 35 – 180 Hz. The dominant frequency of the raw PS signal is approximately 60 Hz, and the converted-wave bandwidth extends from 35 – 150 Hz. That is, these PS data do exhibit reduced dominant frequency compared to the P data. Nevertheless, the frequency reduction appears less than is typically observed. Acquisition of this dataset occurred during an extended period of drought, and the surface layer was very dry and hard. The high degree of compactness of the surface layer is thought to be one of the reasons the PS data in this area exhibit relatively high frequency energy. This has favourable implications in the context of vertical resolution (Appendix D) as will be discussed in Section 4.4.

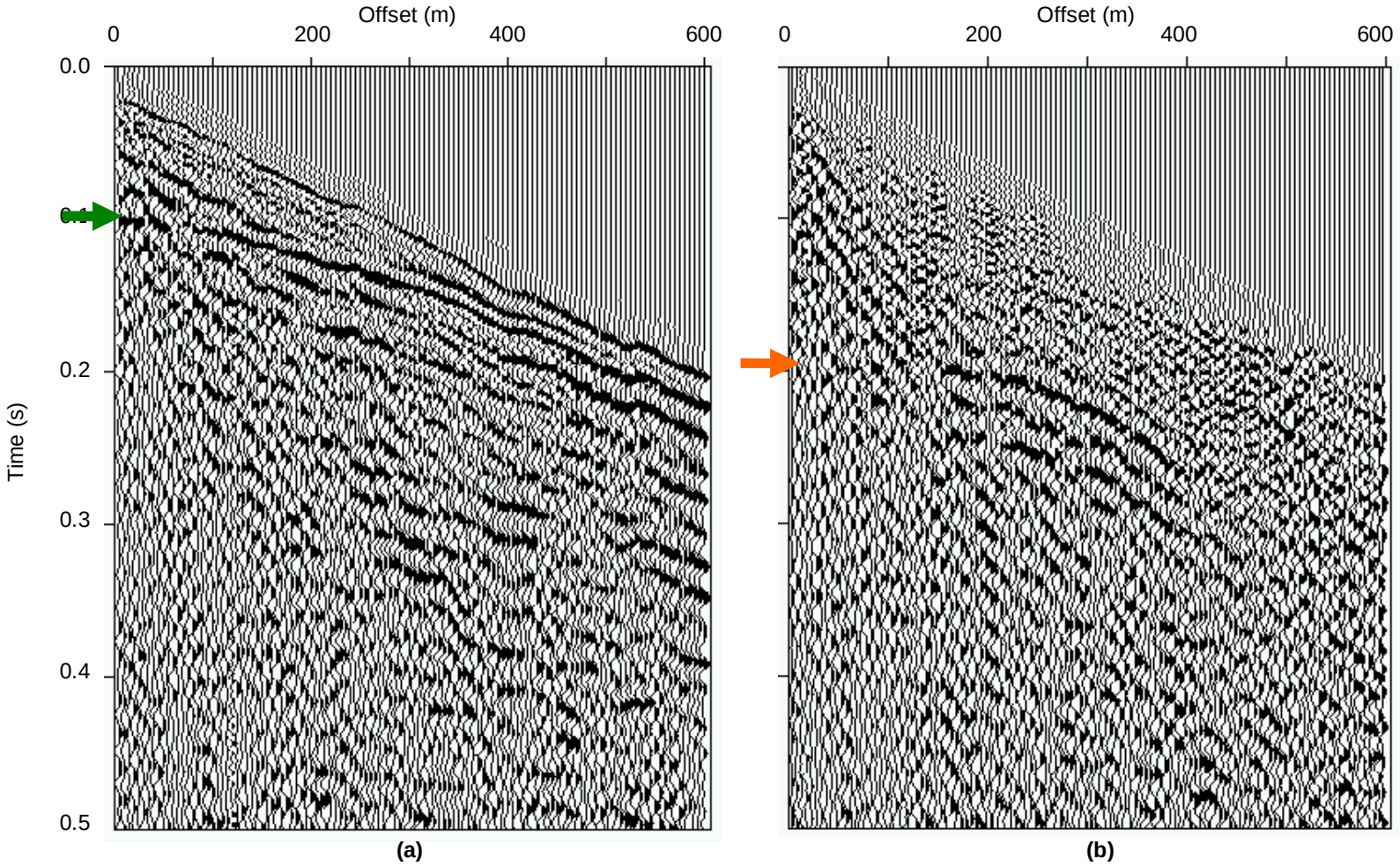

Figure 4.2 (a) Vertical component and (b) inline component of a representative shot record from the first trial multi-component dataset. The target P and PS reflection events are indicated by the green and orange arrows, respectively.

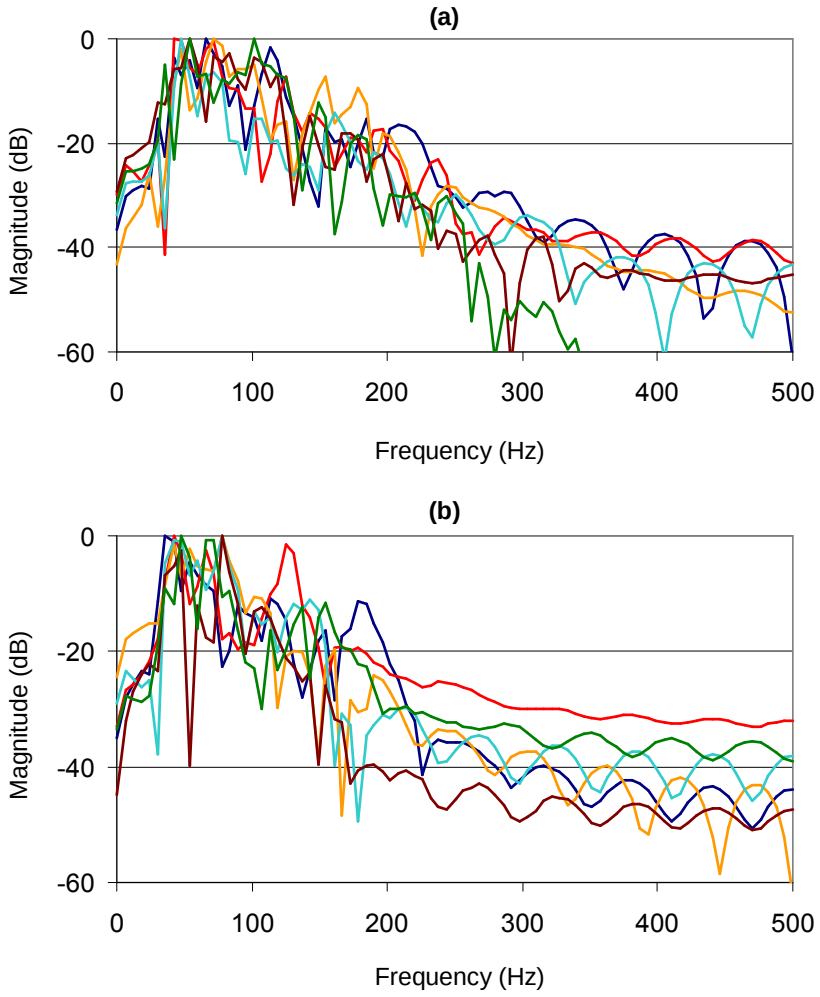

Figure 4.3 Representative trace spectra from the (a) vertical component and (b) inline component shot records given in Figure 4.2. These magnitude spectra have been computed over short time windows centred about the target reflection events. The P-wave energy has a signal bandwidth of approximately 35 – 130 Hz. The PS-wave energy has a signal bandwidth of approximately 35 – 100 Hz.

4.3 Converted-Wave Processing

The processing sequence used to extract a PS image from the first trial dataset has been quite experimental since no work on converted-wave processing of high-resolution onshore seismic data has previously been published. The experience gained from working with this dataset has contributed to better processing practices for the second trial dataset (Chapter 5). Details of the processing sequence used to generate the first PS image are given below. See Chapter 3 for in-depth discussion on the theory and methodology behind the specific PS processing algorithms listed here.

Reformat

Field data were reformatted from SEGY to the Seismic Unix internal C-binary format.

Geometry

Geometry details, including source and receiver locations, elevation, shot depths, uphole times, offsets, P-wave CDP numbers and P-wave source statics, were assigned to trace headers.

Trace Editing

Dead or noisy traces were removed from field records.

Horizontal Component Rotation

Horizontal component rotation has not been performed since no significant energy was immediately obvious on the crossline component of data. Further analysis is required to determine whether the crossline component of data can contribute to the converted-wave image. All subsequent PS processing has been undertaken using only the inline component of data.

Polarity Reversal

The polarity of all inline traces with negative offsets was reversed.

Amplitude Recovery

A time-varying scale factor was applied to each trace to help compensate for the effects of amplitude loss due to geometric spreading. The gain function $t^{0.7}$ was applied to each sample in the data, where t is the two-way time.

P-Wave Source Statics + Residual Source Statics Corrections

P-wave source statics, together with residual source statics, computed as part of the conventional P-wave processing sequence, were applied to the inline data.

Brute Vp/Vs Analysis

Initially a constant *Vp*/*Vs* (where *Vp* = P-wave velocity and *Vs* = S-wave velocity) was approximated for the entire line. The optimum *Vp*/*Vs* value was selected via a series of constant *Vp*/*Vs* common-receiver gather (CRG) stacks.

S-Wave Receiver Statics Corrections – 1st Iteration

First-pass receiver statics were computed using the CRG stack-power optimisation method (Section 3.2.3). A correlation window of 60 ms and a trace window width of 15 were used.

Horizon-Based CCP Binning and Vp/Vs Analysis

Constant *Vp*/*Vs* common-conversion point (CCP) stack panels were used to produce a spatially- and time-variant *Vp*/*Vs* function following the first iteration of receiver statics. (This approach is analogous to the conventional CVS velocity analysis approach (e.g. Yilmaz, 1987).) Note that for each trial *Vp*/*Vs* value, the CCP gathers were regenerated via the horizon-based method of CCP binning to optimise velocity analysis. For this, and all other stages of processing involving CCP binning, the binning horizon was allowed to vary laterally, tracking the target coal seam.

S-Wave Receiver Statics Corrections – 2nd Iteration

A second iteration of automated receiver statics (Section 3.2.3) was found necessary to remove further time shifts in the CRG stack subsequent to updating the *Vp*/*Vs* function. Again a correlation window of 60 ms and a trace window width of 15 were used. Figure 4.4 shows the CRG stack before and after application of receiver statics. There is significant improvement in the coherency of the target reflector following the application of receiver statics. The final PS-wave receiver statics for these data are compared to the corresponding P-wave receiver statics in Figure 4.5. As expected, the PS receiver statics are larger and more variable than the P-wave statics. Note however, that while the high-frequency variation in receiver statics observed in Figure 4.5 is plausible, it is suspected that these S-wave receiver statics are contaminated with some spurious static jumps associated with cycle-skipping.

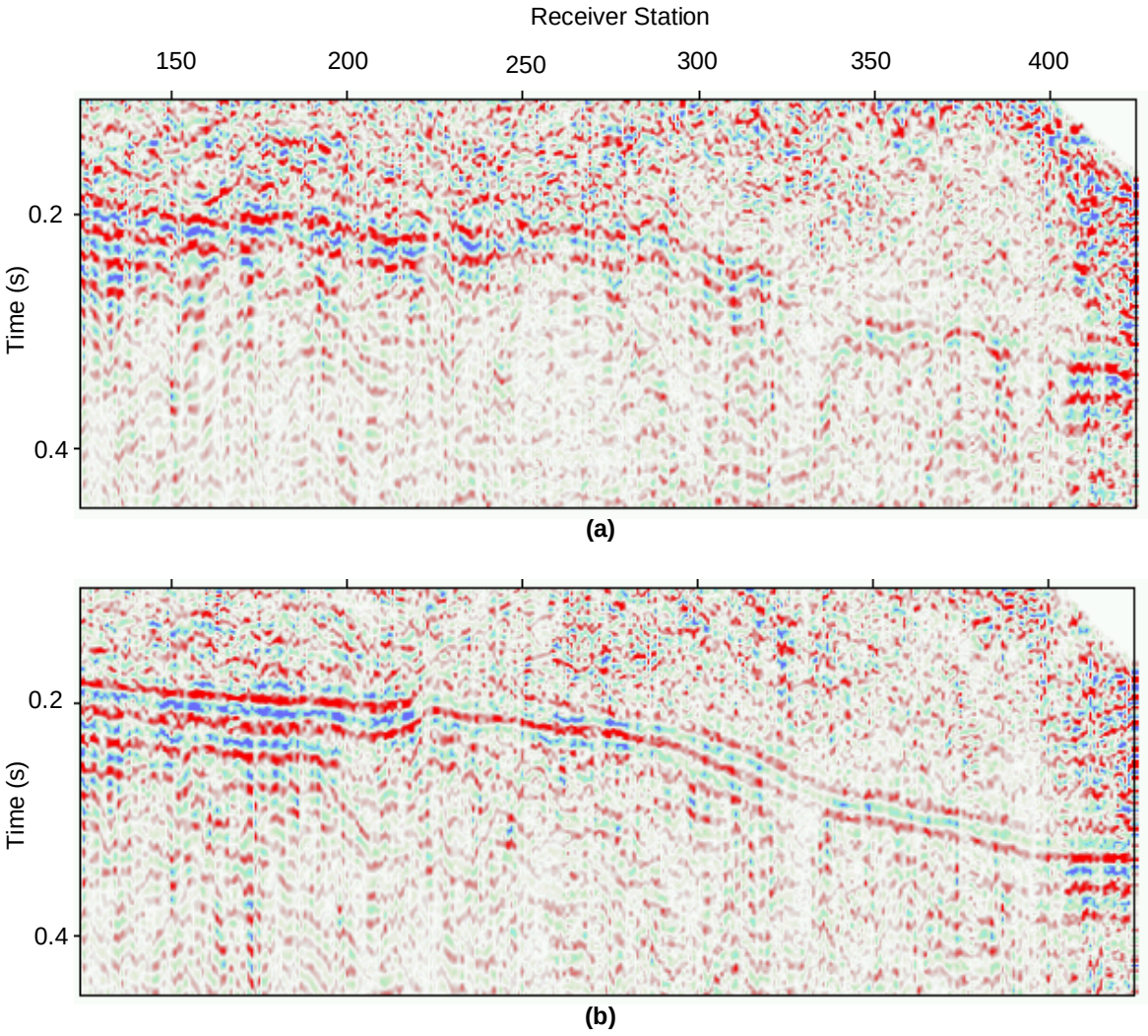

Figure 4.4 Inline common-receiver gather (CRG) stack for Dataset #1 (a) before application of PS receiver static corrections and (b) after application of PS receiver static corrections. The coherency of the target reflection event is improved by static corrections.

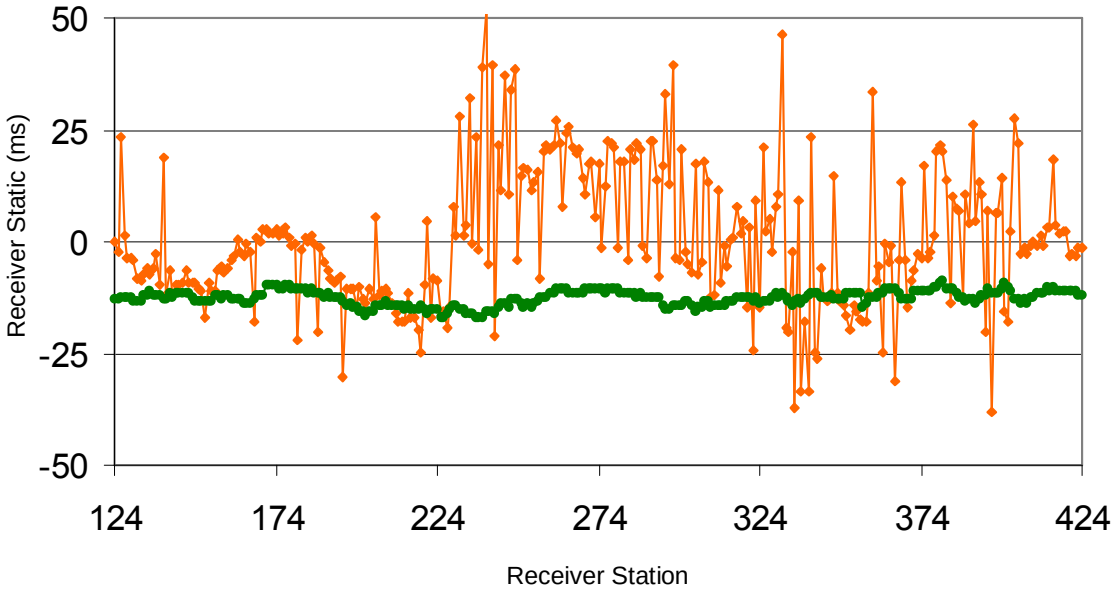

Figure 4.5 Comparison of P receiver statics (green) and PS receiver statics (orange) for the first trial multi-component dataset. The PS receiver statics are larger and more variable than the P-wave statics. Note however, that while high-frequency variations in PS receiver statics are plausible, some of the rapid jumps in these PS statics are believed to be anomalies introduced by the CRG stack-power optimisation approach to static calculation.

Horizon-Based CCP Binning and Final Vp/Vs Analysis

Again, constant *Vp*/*Vs* CCP stack panels were used to produce a spatially- and time-variant *Vp*/*Vs* function following the second iteration of receiver statics. For each trial *Vp*/*Vs* value, the CCP gathers were regenerated via the horizon-based method of CCP binning to optimise velocity analysis. Note that for this, and all previous, stages of velocity analysis, only traces with positive offsets were considered. This was necessary because of the extreme diodic (i.e. non-symmetric) moveout observed in the CCP gathers. This behaviour is believed to be caused by inhomogeneities in the sub-surface (Thomsen, 2002). Further investigation into such anomalous wave propagation behaviour is warranted.

Horizon-Based CCP Binning and NMO Correction

Following calculation of the final *Vp*/*Vs* function, CCP gathers were recreated using the optimum spatially- and time-variant velocity information, and the relevant normal moveout (NMO) correction was applied.

CCP Trim Statics

CCP trim statics were computed to ensure optimum alignment of the target reflection event within each CCP gather following NMO. This process involves the correlation of each trace within the CCP gather with a pilot trace for that gather. The pilot trace was the resultant stacked trace for that CCP

gather following removal of all traces with offsets less than 160 m (including those traces with negative offsets). The correlation window was 20 ms about the target reflection event. The maximum trim static shift allowed was 10 ms. Note that, while trim statics successfully resulted in a sharper target reflection pulse from each CCP gather, the process introduced subtle time shifts into the final CCP stack. This could not be remedied using a multi-CCP pilot trace for the trim static calculation. Instead a running nine-trace correlation smoothing filter was applied to the final stack.

Bandpass Filter

The pre-stack CCP gathers were filtered using a zero-phase bandpass filter: 30/40 Hz – 150/220 Hz.

Pre-Stack AGC

Prior to stacking of the CCP gathers, an automatic gain function (AGC) was applied using a 300 ms window to help strengthen the amplitude of target reflection event with respect to background noise.

Offset Mute

Very little converted-wave energy was observed on the near-offset traces of the inline data. This is consistent with PS amplitudes predicted by theory (Figure 1.6). In addition, these near-offset traces were often affected by surface-wave noise. Consequently a mute was applied to eliminate all traces with offsets less than 120 m.

Stack

All traces sharing a CCP location were summed. Note that only traces with positive offsets contributed to the final stack for this dataset. This stacking method works around the diodic (i.e. non-symmetric) moveout observed in the converted-wave records. Note that each sample in the stacked trace is scaled by the number of non-zero samples that contributes to that stacked sample.

Post-Stack Correlation Smoothing Filter

A running nine-trace correlation smoothing filter was applied to the final CCP stack. This was found to be necessary to compensate for the side effects of the pre-stack CCP trim statics process. The smoothing filter involved correlating each trace in the CCP stack with a pilot trace constructed by the summation of the nine preceding traces in the stack. The correlation window was 20 ms about the target reflection event. A maximum time shift of 6 ms was allowed. Note that to preserve dip and structure in the PS section, the time shifts associated with dip and structure were removed prior to applying the running trace smoothing filter.

FX Deconvolution

Coherent seismic reflection events in the PS stack were enhanced using fx deconvolution to attenuate random noise. Relevant processing parameters are as follows:

Frequency bandwidth	20 – 400 Hz
Number of traces in analysis window	50
Window Length	0.5 s
Number of traces in filter	5

4.4 Final Results

The final P-wave and PS-wave images derived from the first multi-component trial are shown in Figure 4.6. Note that it is common practice when comparing P and PS sections to compress the PS section time such that the two sections show the same effective depth (see Appendix E for details on correlating P and PS sections). The time axis of the PS image in Figure 4.6 has been adjusted to provide this comparable depth perspective.

As is typically observed, the PS image has a lower signal-to-noise ratio than the P image. Nevertheless, Figure 4.6 demonstrates that PS imagery is possible in the shallow, high-resolution environment. A significant fault has been interpreted at approximately CDP/CCP 450, with a throw of the order of 10 m. This fault is imaged successfully by both the P and PS data. No other structural features have been interpreted on either the P or PS images. There are however, a couple of other points of interest immediately obvious in Figure 4.6.

First, the target reflector in the PS section tends to drop in amplitude along the eastern end of the line. This is highlighted in Figure 4.7 which shows the P and PS amplitudes of the interpreted top coal reflection event. It is unclear at this time whether this loss of amplitude in the PS reflection energy is associated with the relative depth of the seam, a zone of poor receiver statics or S-wave velocity analysis (and hence poor stack), the relatively steeper dip of the target seam in the east, or some other 'lithological' change (e.g. change in seam thickness, roof geology etc). No such variation in amplitude of PS reflection events is observed in the PS image from the second trial area (Section 5.4.2).

The second feature of interest in Figure 4.6 is that, on a purely visual level, the PS section appears to exhibit greater vertical resolution than the P image. Measurements of resolution are discussed in detail in Appendix D. Essentially, since S-wave velocities are less than P-wave velocities, for waves with approximately the same frequency bandwidth, S waves will have shorter wavelengths, and hence greater vertical resolving power. Figure 4.8 illustrates representative trace spectra from the P and PS sections in Figure 4.6. It is apparent that the PS image suffers from a slightly reduced frequency bandwidth. However, the frequency content of the PS data is sufficient to yield greater vertical resolution along the entire length of the line (Appendix D). This is in contrast to previous petroleum-sector results which have consistently found that PS images have reduced dominant frequencies when compared to P-wave images such that no net resolution improvement is observed. The results obtained here support previous predictions (e.g. Garotta, 1999) that PS resolution improvements are theoretically more likely in the shallow environment than for petroleum-scale seismic applications.

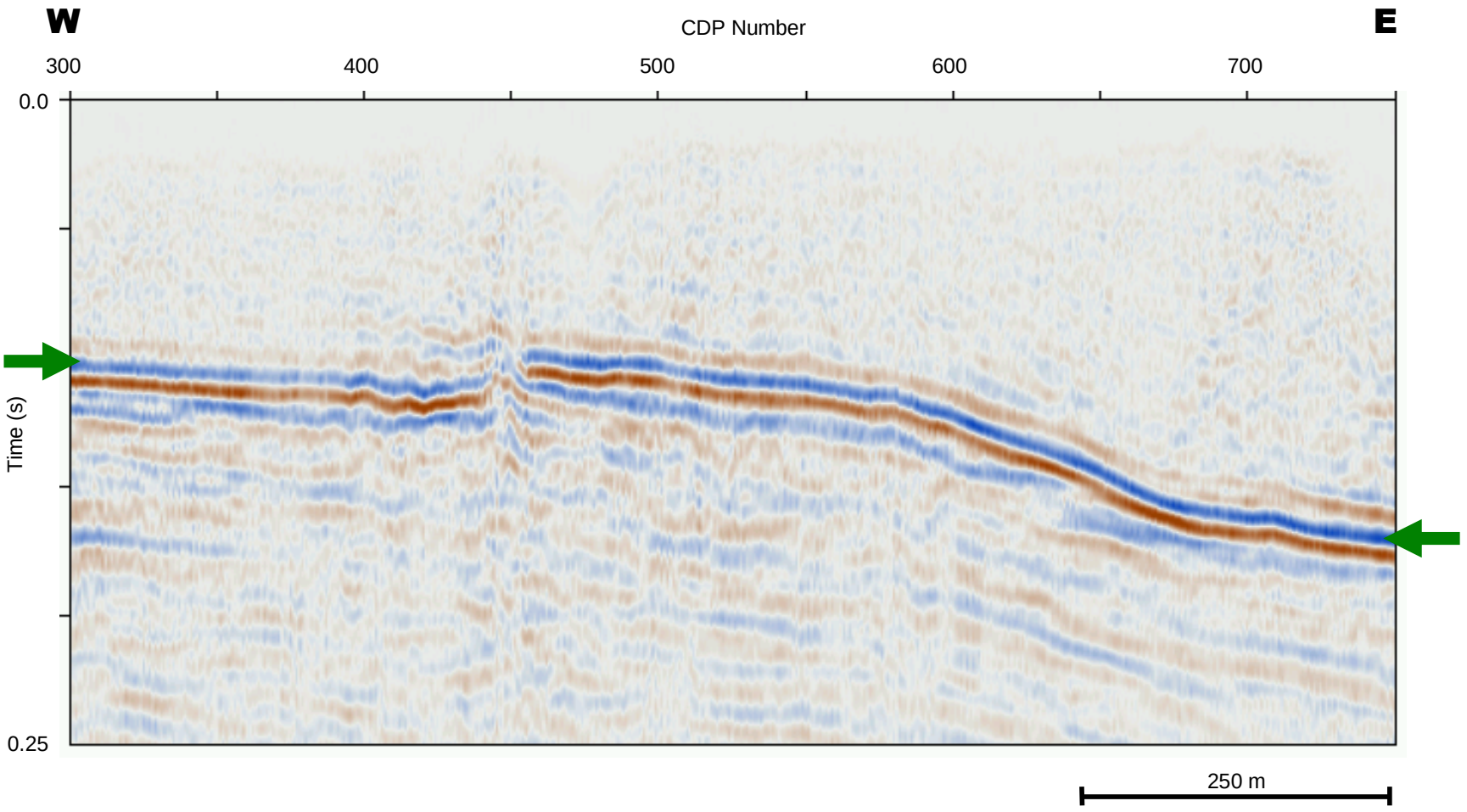

Figure 4.6 (a) Conventional P-wave image derived from the vertical component of the 3-C data acquired in the first trial area. The target coal-seam reflection event is indicated by the green arrow.

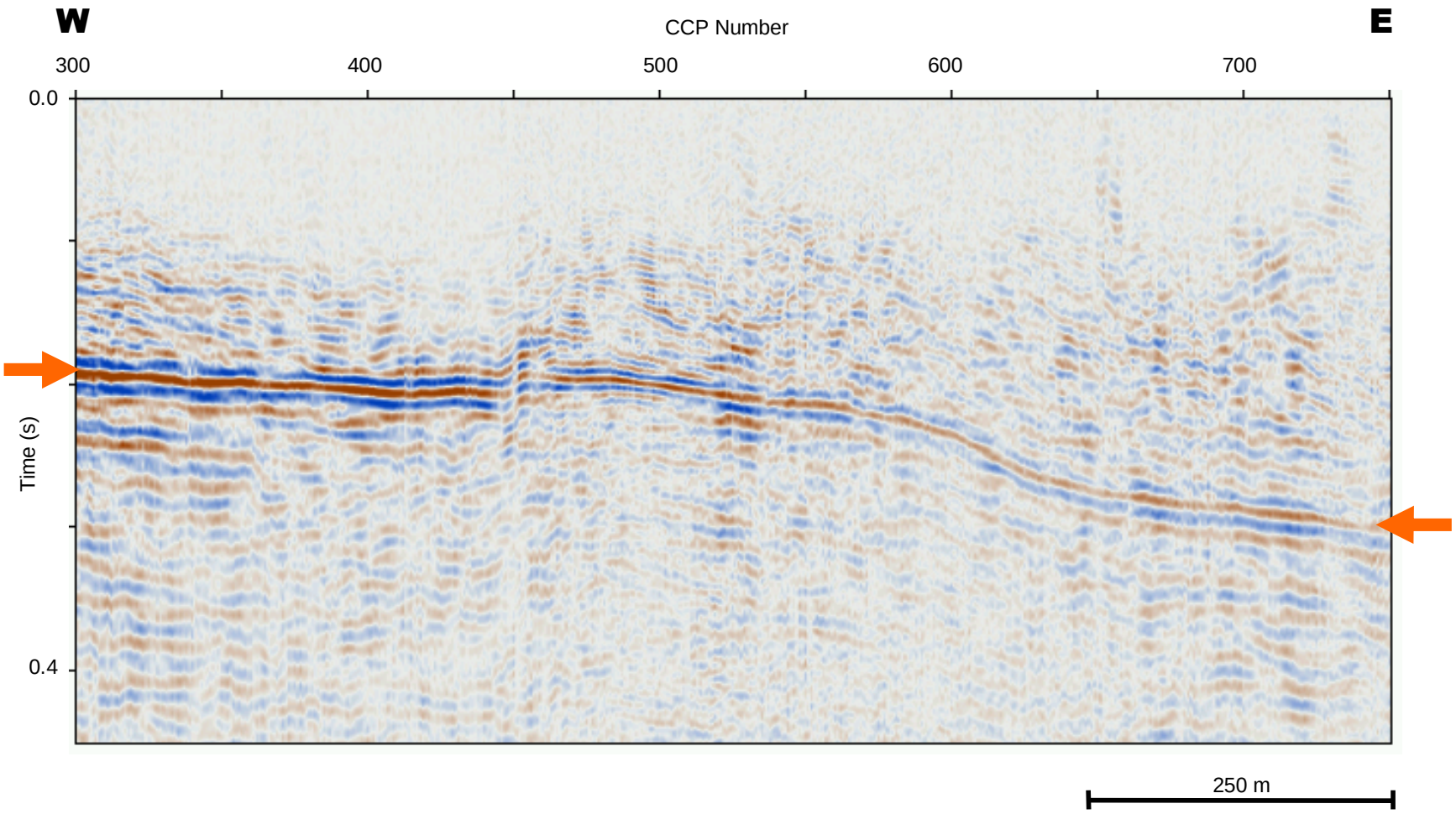

Figure 4.6 (b) Converted-wave (PS) image derived from the inline component of the 3-C data acquired in the first trial area. The target coal-seam reflector is indicated by the orange arrows.

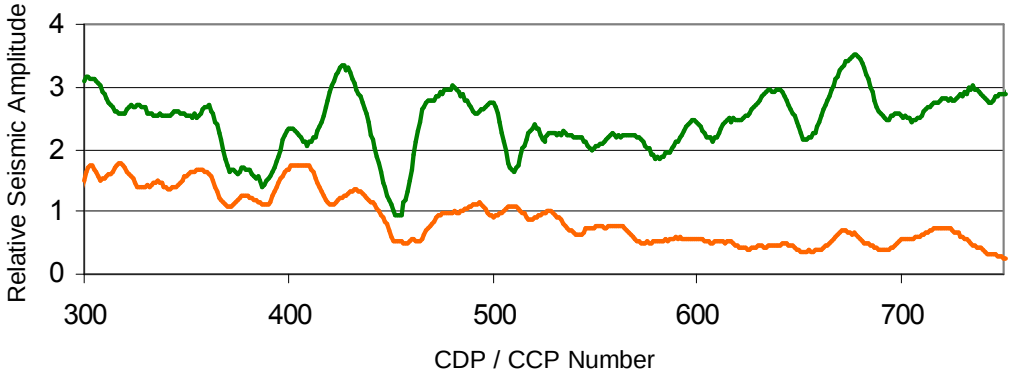

Figure 4.7 Comparison of P (green) and PS (orange) reflection amplitudes along the interpreted top-coal seismic reflection event imaged in Figure 4.6.

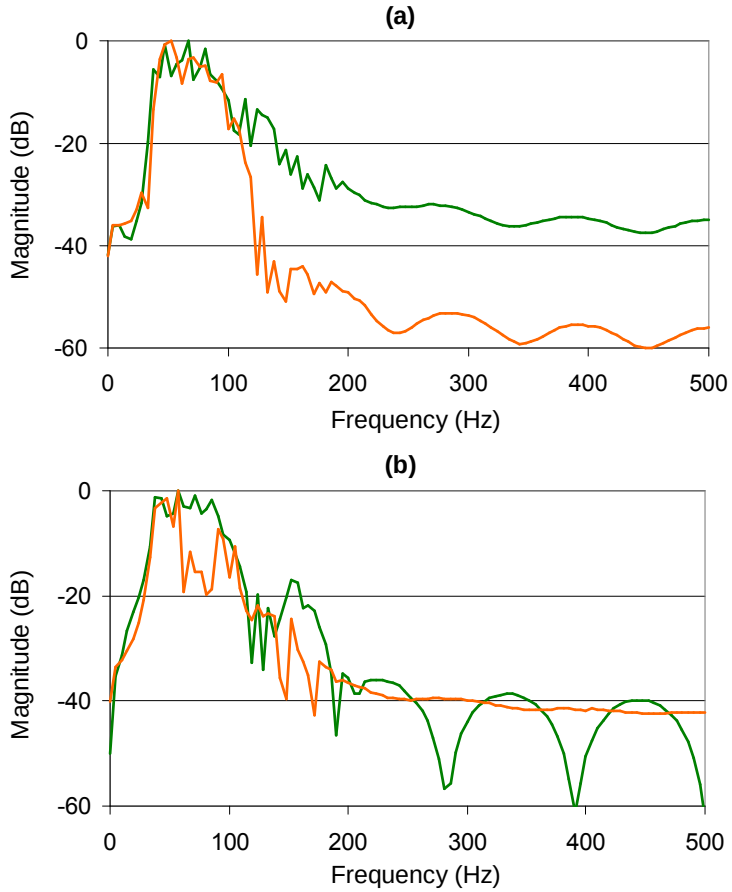

Figure 4.8 Comparison of trace spectra from the final P and PS sections shown in Figure 4.6 – (a) from the western end of the line; and (b) from the eastern end of the line. Magnitude spectra for the P-wave data are shown in green. Magnitude spectra for the corresponding PS data are shown in orange.

CHAPTER FIVE
REAL-DATA TRIAL #2

5.1 Introduction

Given the high dependency of the propagation of converted waves on lithology, and therefore the likelihood that trial results could be site specific, it was proposed that a second three-component dataset be acquired as part of this research project. This has added significantly to the validation of the converted-wave seismic concept. The second trial dataset is from a location in the Bowen Basin, Queensland that exhibits quite different geological character than that observed in the first trial area. Here the geology is characterised by multiple coal seams, and a thin, deeper target seam. This chapter provides details on the acquisition and processing parameters used to produce the converted-wave section from this trial area, and presents the final P-wave and PS-wave images. Note that this second trial dataset was acquired in parallel with a regular 2D seismic line. A comparison of the P-wave sections produced by the regular array recording, and single vertical geophone recording is also included.

5.2 Data Acquisition

Acquisition of Trial Dataset #2 was undertaken by Velseis Pty Ltd during December 2002 (Figure 5.1). The recording parameters are given in Table 5.1. Note that while the regular 2D seismic line recorded in parallel with the three-component experiment extends for a length of 3.25km, the three-component data have only been acquired along the eastern 2.05 km of the line.

Table 5.1: Field acquisition parameters for Trial Dataset #2.

Recording System	Velcom 348
Line Length	Conventional – 3.25 km Three-Component – 2.05 km
Source	Dynamite 400g Booster
Source Depth	12-40 m
First / Last Shotpoint	Conventional – 100.5 / 425.5 Three-Component – 220.5 / 425.5
Shotpoint Interval	20 m
Geophone	Conventional – SM4/7 30 Hz / 375 ohm Three-Component – GS40D 40Hz / 420 ohm
Receiver Array	Conventional – 6 geophones over 2m Three-Component – single geophone
Receiver Interval	10 m
Spread	Conventional – 120 channels split spread Three-Component – 120 channels x3 split spread
Near Trace	5 m
Far Trace	595 m
Nominal Fold	30
Data Format	SEGY
Sample Interval	1 ms
Record Length	1 s

Figure 5.1 Field acquisition of Trial Dataset #2 - clockwise from top left: recording truck; moving recording equipment to front of line; and a three-component receiver station.

Surface conditions and elevation varied along the seismic line. Figure 5.2 illustrates that the line can be roughly divided into three zones. The western end of the line is characterised by a slightly eastward-dipping topography with a thick layer of very loose, gritty bulldust on the surface. The centre of the line traverses a relatively low-lying creek floodplain with a muddy soil surface. The eastern portion of the line is characterised by a higher topography and a more compact, sandy surface layer. These changing conditions influence the relative receiver statics along the line, as will be demonstrated in Section 5.3.

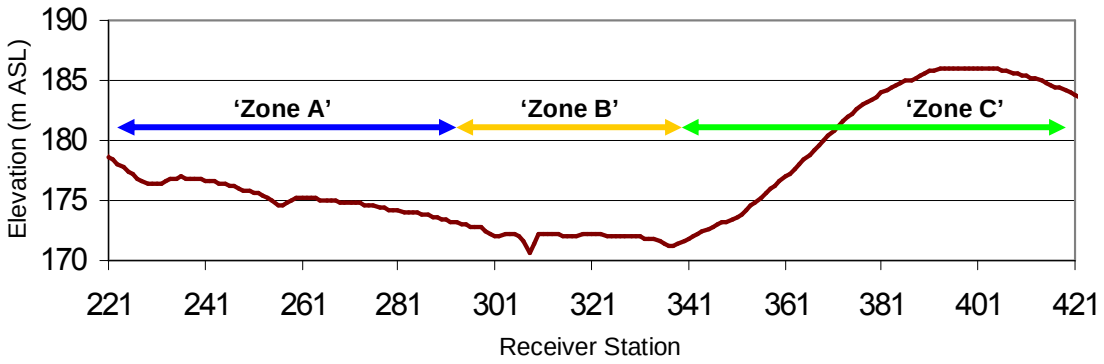

Figure 5.2 Surface elevation along the second 2D multi-component seismic trial line. The surface conditions and elevation roughly divide the line into three characteristic zones.

Representative vertical and inline common-receiver gathers (CRGs) from the second trial dataset are shown in Figure 5.3. (Note that due to severe S-wave receiver statics, PS reflection events are not coherent on raw shot records. Hence, CRGs are examined here.) It is apparent that P-to-S wave conversion is occurring at multiple horizons in the geological sequence, with several dominant converted-wave reflections present in the inline data. These results, together with those from the first trial, demonstrate that acquisition of shallow PS data is viable in a range of geological environments.

Figure 5.4 illustrates frequency panels for the vertical and inline common-receiver gathers shown in Figure 5.3. The raw P-wave signal extends up to approximately 160 Hz, with signal dominantly in the 40 – 110 Hz frequency bandwidth. The PS-wave signal only extends up to approximately 90 Hz, with signal dominantly in the 30 – 50 Hz bandwidth. The significant reduction in the PS frequency bandwidth has implications in the context of vertical resolution of the PS image, as will be discussed in Section 5.4.2. Note that no significant variation in frequency content is observed along the line, despite the changing surface conditions. Ground roll is apparent in the records shown in Figure 5.3. Spectral analysis indicates that the groundroll noise has energy up to at least 90 Hz. Thus it is potentially damaging for any converted-wave imaging.

5.3 Converted-Wave Processing

The processing sequence used to extract a converted-wave image from the Dataset #2 differs somewhat to that used to process the first trial dataset. This is partly a result of experience gained in working with the first dataset, and partly due to the significantly different data characteristics associated with the multi-seam environment. Details of the processing sequence are given below. See Chapter 3 for in-depth discussion on the theory and methodology behind the specific PS processing algorithms listed here.

Reformat
Field data were reformatted from SEGY to the Seismic Unix internal C-binary format.

Geometry
Geometry details, including source and receiver locations, elevation, shot depths, uphole times, offsets, P-wave CDP numbers and P-wave source statics, were assigned to trace headers.

Trace Editing
Dead or noisy traces were removed from field records. Note corrections were also made for incorrectly connected three-component geophones (see Table 5.2).

Table 5.2 Summary of incorrect three-component geophone connections observed in the field during acquisition of Trial Dataset #2.

Receiver Station	Comment
244	Crossline connected to vertical line; Vertical connected to inline line; Inline connected to crossline line
294	Vertical and inline connections swapped
297	Inline and crossline connections swapped

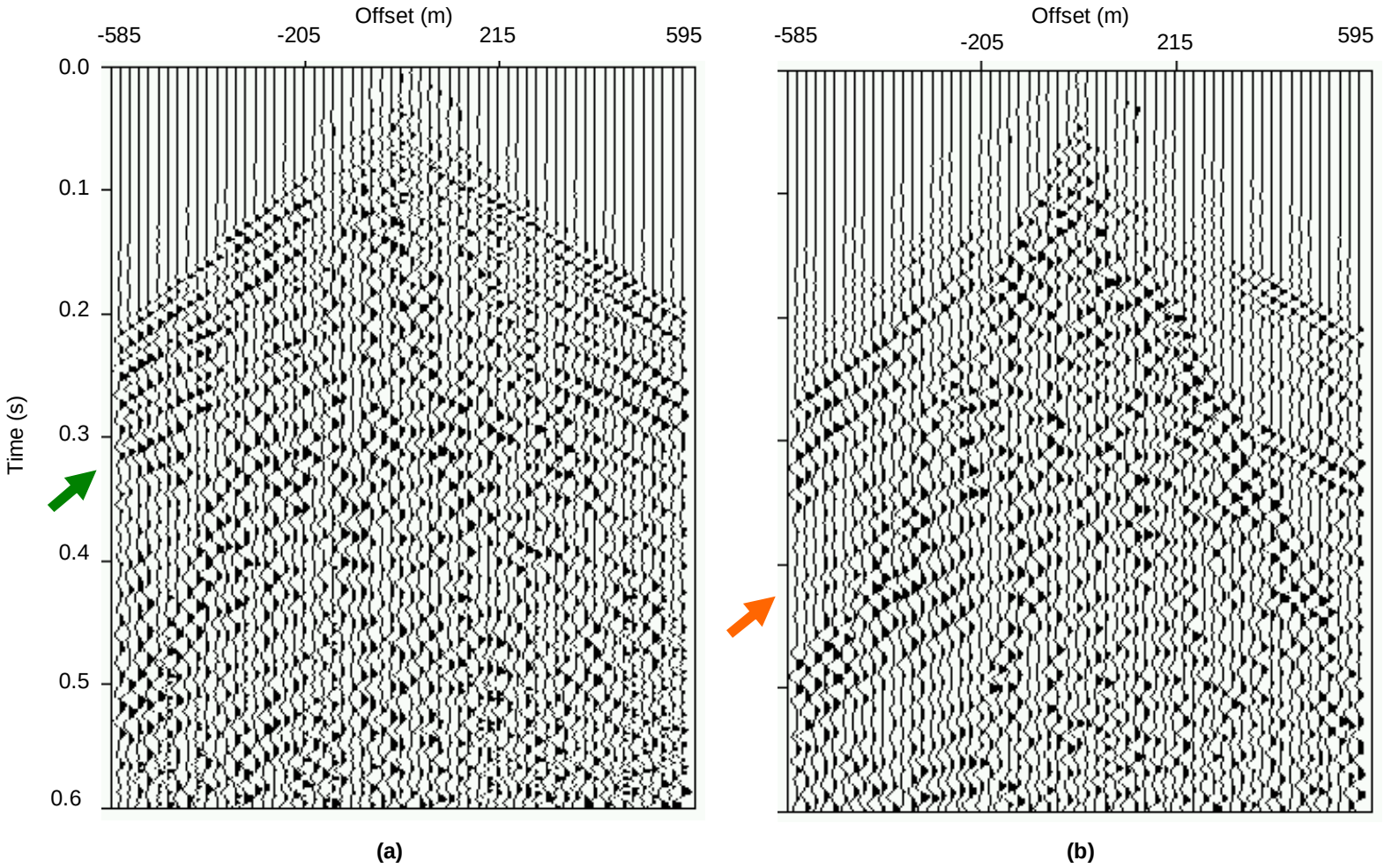

Figure 5.3 Representative vertical (a) and inline (b) common-receiver gathers (CRGs) from Trial Dataset #2. The target P and PS reflection events are indicated by the green and orange arrows, respectively.

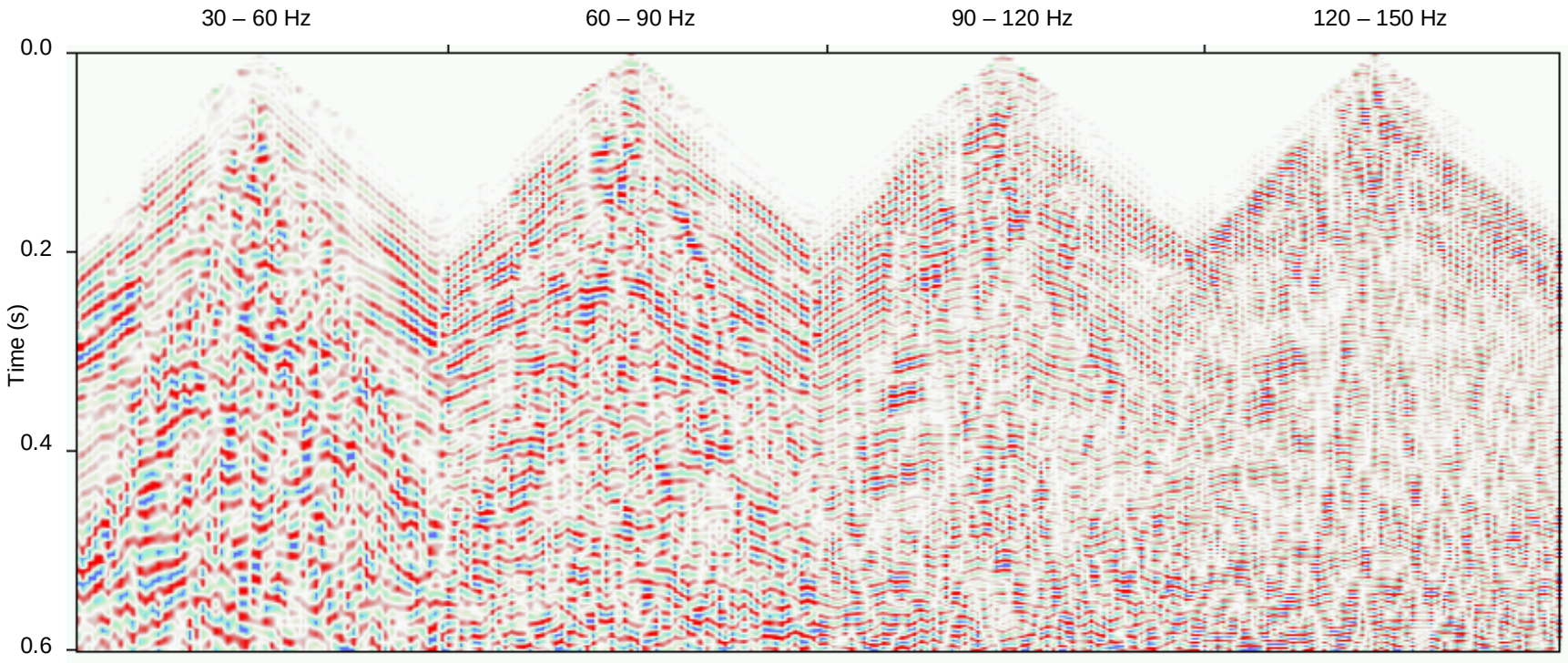

Figure 5.4 (a) Frequency bandwidth panels for the vertical component CRG shown in Figure 5.3(a). The P energy has a maximum signal frequency of approximately 160 Hz, with most signal in the range 40 – 100 Hz.

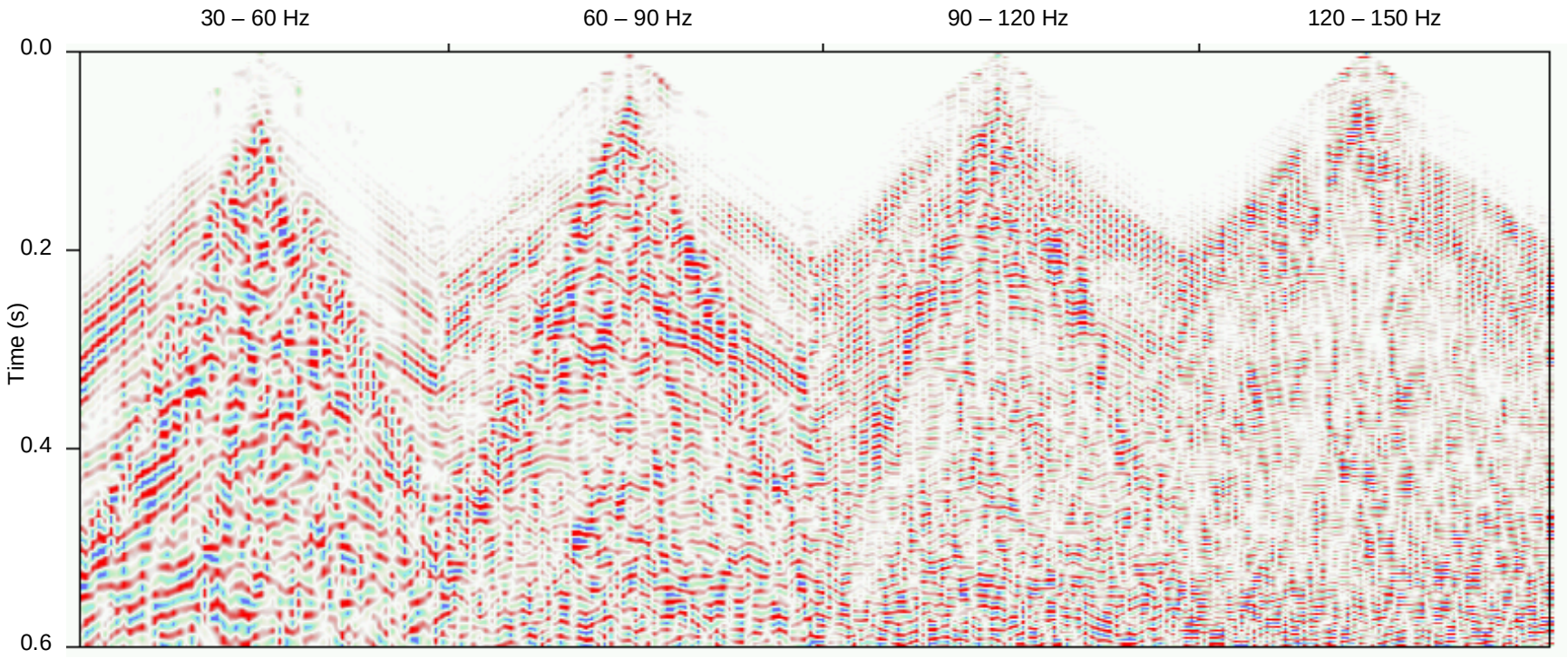

Figure 5.4 (b) Frequency bandwidth panels for the inline component CRG shown in Figure 5.3(b). The PS energy has a maximum frequency of approximately 90 Hz, with most signal in the range 30 – 60 Hz. Groundroll energy is significant on the inline component, and has frequencies up to at least 90 Hz.

Horizontal Component Rotation

Note that horizontal component rotation has not been performed since no significant energy was immediately obvious on the crossline component of data. Further analysis is required to determine whether the crossline component of data can contribute to the converted-wave image. All subsequent PS processing has been undertaken using only the inline component of data.

Polarity Reversal

The polarity of all inline traces with negative offsets was reversed.

Amplitude Recovery

A time-varying scale factor was applied to each trace to compensate for the effects of amplitude loss due to geometric spreading. First, the conventional P-wave spherical divergence correction $[t \times V \times V]^{-1}$ (where t is the two-way time and V is the average P-wave stacking velocity at that time) was applied to each sample in the data. To compensate for not using a gain function designed to specifically compensate for geometric spreading of PS data, the gain function $t^{0.7}$ was subsequently applied to each sample in the data.

P-Wave Source Static + Residual Source Static Corrections

P-wave source statics, together with residual source statics, computed as part of the conventional P-wave processing sequence, were applied to the inline data.

Brute Vp/Vs Analysis

A preliminary *Vp*/*Vs* ratio (where *Vp* = P-wave velocity and *Vs* = S-wave velocity) was approximated along the line using pre-existing P-wave stacking velocities and PS-NMO semblance analysis for common-receiver gathers. Some difficulties were encountered in analysing the inline data, particularly in areas of strong groundroll contamination, and for very shallow data where it is suspected that significant P-wave cross-contamination is occurring.

S-Wave Receiver Static Corrections – 1st Iteration

Receiver statics were hand-picked from the common-receiver gather (CRG) stack. Hand-picked statics were favoured (in contrast to the automatic CRG stack-power optimisation statics used for the first trial dataset) because of the very large, abrupt static shifts that occurred between the 'acquisition zones' discussed in Section 5.2, and because of the demonstrated potential of the automated approach to produce static corrections contaminated by cycle-skipping.

Vp/Vs Analysis

A series of constant *Vp*/*Vs* CRG stacks were used to produce an improved S-wave velocity function prior to a second-pass of receiver statics. This was necessary due to the very large static shifts that were applied as a result of the first iteration of receiver statics. Note that this method of *Vp*/*Vs* analysis was preferred over PS-NMO semblance analysis due to the complications mentioned above regarding calculation of the brute *Vp*/*Vs* function.

S-Wave Receiver Static Corrections – 2nd Iteration

Two iterations of receiver static computation were required to produce the optimum CRG stack. Figure 5.5 shows the CRG stack before and after the application of receiver statics.

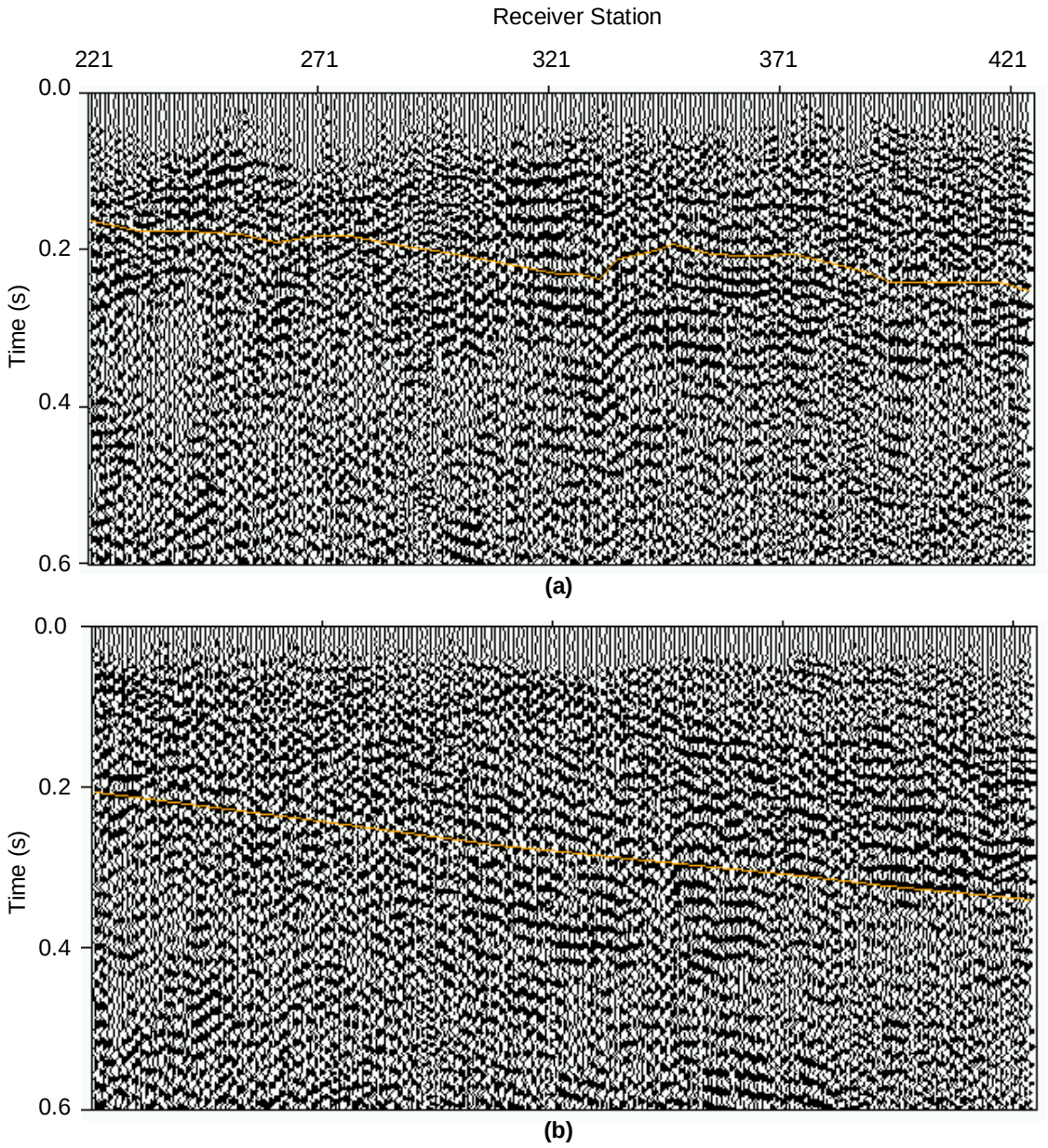

Figure 5.5 Inline common-receiver gather (CRG) stack for Dataset #2 (a) before application of PS receiver static corrections and (b) after application of PS receiver static corrections. The PS reflection event used to design the static corrections is marked in orange. The coherency of the target reflection event is improved by receiver static corrections.

Figure 5.6 compares the P-wave and PS-wave receiver statics for these data. As expected, the PS receiver statics are very much larger than the conventional P-wave statics. Note, also, that the variation in amplitude of the PS receiver statics approximately corresponds to the observed changes in surface conditions. The various surface geologies along the 2D seismic line change the speed with which the S-wave energy can reach the 3-C receivers. For example, the western end of the line, where the surface layer is considered to be the least consolidated, suffers from the largest statics.

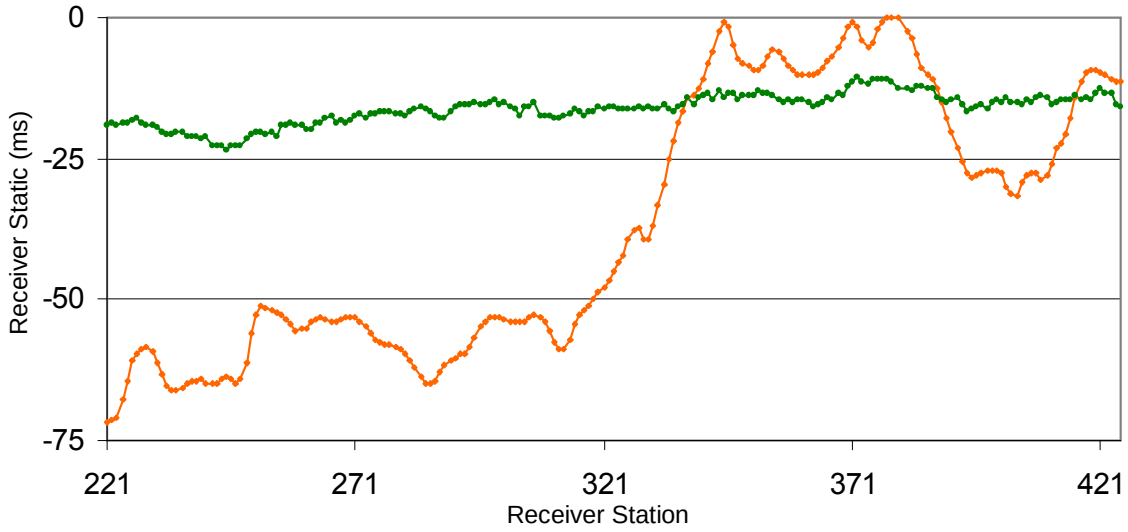

Figure 5.6 Comparison of P receiver statics (green) and PS receiver statics (orange) for Trial Dataset #2. The PS receiver statics are much larger than the corresponding P-wave receiver statics. Note that the sharp jump in receiver statics at approximately Station 330 is associated with the transition from a poorly consolidated weathering layer to a more compact weathering layer. This change corresponds to observed changes in surface elevation and surface conditions (Figure 5.2).

Final Vp/Vs Analysis

A series of constant *Vp*/*Vs* common conversion point (CCP) stacks were computed to determine the final *Vp*/*Vs* function for optimum processing of the inline data. In contrast to the first trial dataset, where horizon-based binning was used to produce the CCP gathers, here the best results were achieved using dynamic binning (Section 3.2.4). This is largely due to the presence of multiple coal-seam reflectors at this site. For each trial *Vp*/*Vs* value, the CCP gathers were regenerated via dynamic CCP binning. Relevant parameters for binning the data into CCP gathers are as follows:

First/Last P-wave CDP	441 / 850
Location of first CDP	2207.5 m
CDP spacing	5 m
Number of offsets	119
First offset	-1195 m
Offset spacing	20 m
Any samples with an NMO stretch exceeding 10 ms were muted.	

The final *Vp* and *Vp*/*Vs* functions are shown in Figure 5.7. Note that, while the *Vp*/*Vs* function (Figure 5.7(b)) can give a general idea of the distribution of S velocities in the subsurface, there is some potential error associated with the receiver statics only applying relative shifts to the inline data. The converted-wave data may in fact be bulk shifted with respect to the real recording surface (and the P-wave data). The optimum stacking *Vp*/*Vs* will compensate for this. Furthermore, stacking velocities are typically smoothly varying to optimise stacking, and don't necessarily provide accurate details about the sub-surface. Another approach for determining more detailed *Vp*/*Vs* information that is more closely related to lithological variations in the sub-surface is introduced in Section 5.4.2.

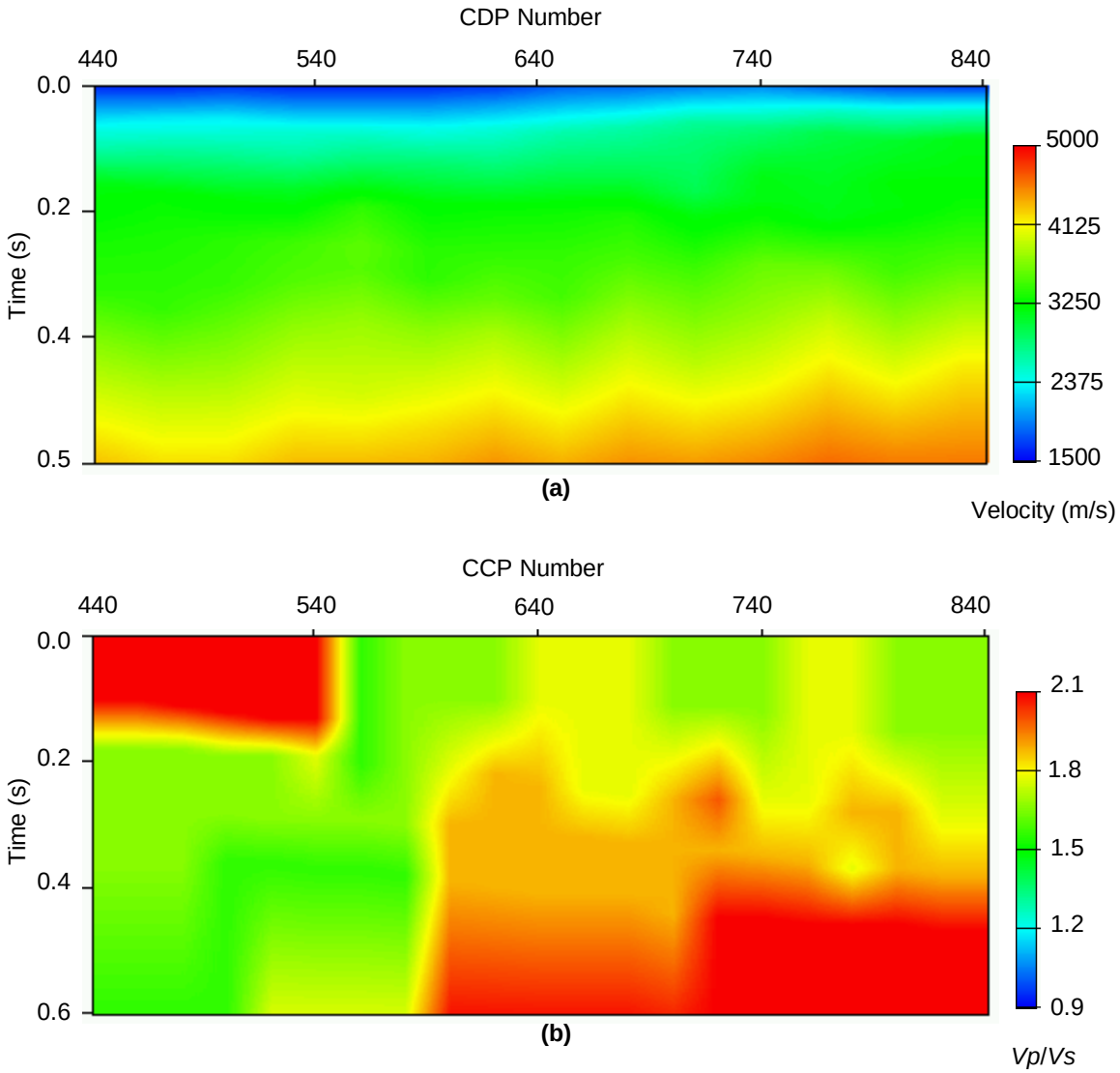

Figure 5.7 (a) P-wave stacking velocity function derived via conventional P-wave processing; and (b) *Vp/Vs* function derived via converted-wave velocity analysis.

Dynamic Binning and NMO Correction

Following calculation of the final *Vp*/*Vs* function, CCP gathers were created using the optimum spatially- and time-variant velocity information, and the relevant normal moveout (NMO) correction was applied. The processing parameters used to dynamically bin the data are the same as used previously.

Deconvolution

Gapped predictive deconvolution was applied to the pre-stack CCP gathers to help enhance reflector resolution via wavelet compression, and reduce multiple noise in the section. Relevant processing parameters are as follows:

Deconvolution gap	20 ms
Design window	0 – 800 ms
Filter length	100 ms
White noise	0.1%

Note however, that due to the fact that the geology imaged here by the seismic data is non-random (i.e. cyclic), deconvolution did little to remove multiple energy, and was only partially successful in compressing the intrinsic seismic pulse to give greater vertical resolution.

Bandpass Filter

The pre-stack CCP gathers were filtered using a zero-phase bandpass filter: 20/30 Hz – 90/140 Hz.

Pre-Stack AGC

Prior to stacking of the CCP gathers, an automatic gain function (AGC) was applied using a 250 ms window to help strengthen the amplitude of reflection events with respect to background noise.

Offset Mute

Very little converted-wave energy was observed on the near-offset traces of the inline data. This is consistent with PS amplitudes predicted by theory (Figure 1.6). Consequently a mute was applied to eliminate the near-offset traces (inside mute given below). In addition, muting was used to remove suspected P-wave cross-contamination on the shallow far-offsets (outside mute given below). Note that the same mute was applied to both positive and negative offset traces.

Inside Trace Mute	
0.0 s	0 m
0.1 s	0 m
0.15s	50 m
0.2 s	150 m
0.8s	150 m

Outside Trace Mute	
0.0 s	150 m
0.0 s	230 m
0.15 s	400 m
0.3 s	500 m
0.4 s	800 m
0.5 s	1200 m

Stack

All traces that share a CCP location were summed. Note that for CCPs up to 579, only traces with negative offsets were summed. For CCPs greater than 579, only traces with positive offsets were summed. This stacking method works around the diodic (i.e. non-symmetric) moveout observed in the converted-wave records that is believed to be caused by inhomogeneities in the sub-surface (Thomsen, 2002). Note that each sample in the stacked trace is scaled by the number of non-zero samples that contributes to that stacked sample.

FX Deconvolution

Coherent seismic reflectors in the PS stack were enhanced using fx deconvolution to attenuate random noise. Relevant processing parameters are as follows:

Frequency bandwidth	20 – 200 Hz
Number of traces in analysis window	100
Window Length	0.4 s
Number of traces in filter	30

Median Filter

A nine-trace median filter, designed to preserve the dominant dip of the data, was used to attenuate steeply dipping artifacts (attributable to remnant groundroll contamination) remaining in the PS section.

Post-Stack AGC

A 300 ms AGC was applied to the final stack for display purposes.

5.4 Final Results

5.4.1 Single Geophone versus Array Recording

The P-wave sections from this trial area, derived via the conventional 2 m geophone array recording and the single three-component geophone recording, are given in Figure 5.8. Representative shot records and associated frequency spectra from the two datasets are given in Figures 5.9 and 5.10. As predicted by numerical modelling of array versus single geophone recording (Section 2.3.2), the frequency content of these two datasets is very similar. The raw array data (Figure 5.9) may have a marginally better signal-to-noise ratio. However, the final sections in Figure 5.8 demonstrate that comparable seismic sections can be produced using short-array and single-geophone acquisition. That is, single-geophone recording is not compromising the quality of the conventional P-wave section. This suggests that multi-component receivers can be easily and cost-effectively integrated into standard seismic surveying practices, and can simultaneously satisfy both conventional and converted-wave imaging requirements.

5.4.2 Converted-Wave Recording

The final P-wave and PS-wave images derived from the three-component data are shown in Figure 5.11. Note that the time axes on these sections have been adjusted to provide a comparable depth perspective (see Appendix E for details on correlating P and PS sections). The ability to successfully produce a converted-wave image from this second trial data area suggests that the concept of PS imaging is generally viable in the shallow, high-resolution coal environment. However, experience gained from processing and interpreting the two trial datasets does indicate that there are some site-specific characteristics of the resultant PS images. For example, it is obvious from Figure 5.11 that this converted-wave stack does not provide any additional vertical resolution over the conventional P-wave image. This is in contrast to the results of the first trial, where the PS section exhibited better vertical resolution than the conventional P-wave section. Recall that any improvement in vertical resolution occurs because S-wave velocities are less than P-wave velocities, so that for waves of the same frequency, the S waves will have shorter wavelengths and greater vertical resolving power (Appendix D). Figure 5.12 clearly shows, however, that for this trial the PS image has a significantly reduced frequency bandwidth compared to the P image. As a result, the PS image yields reduced net vertical resolution, when compared to the P-wave section (Appendix D).

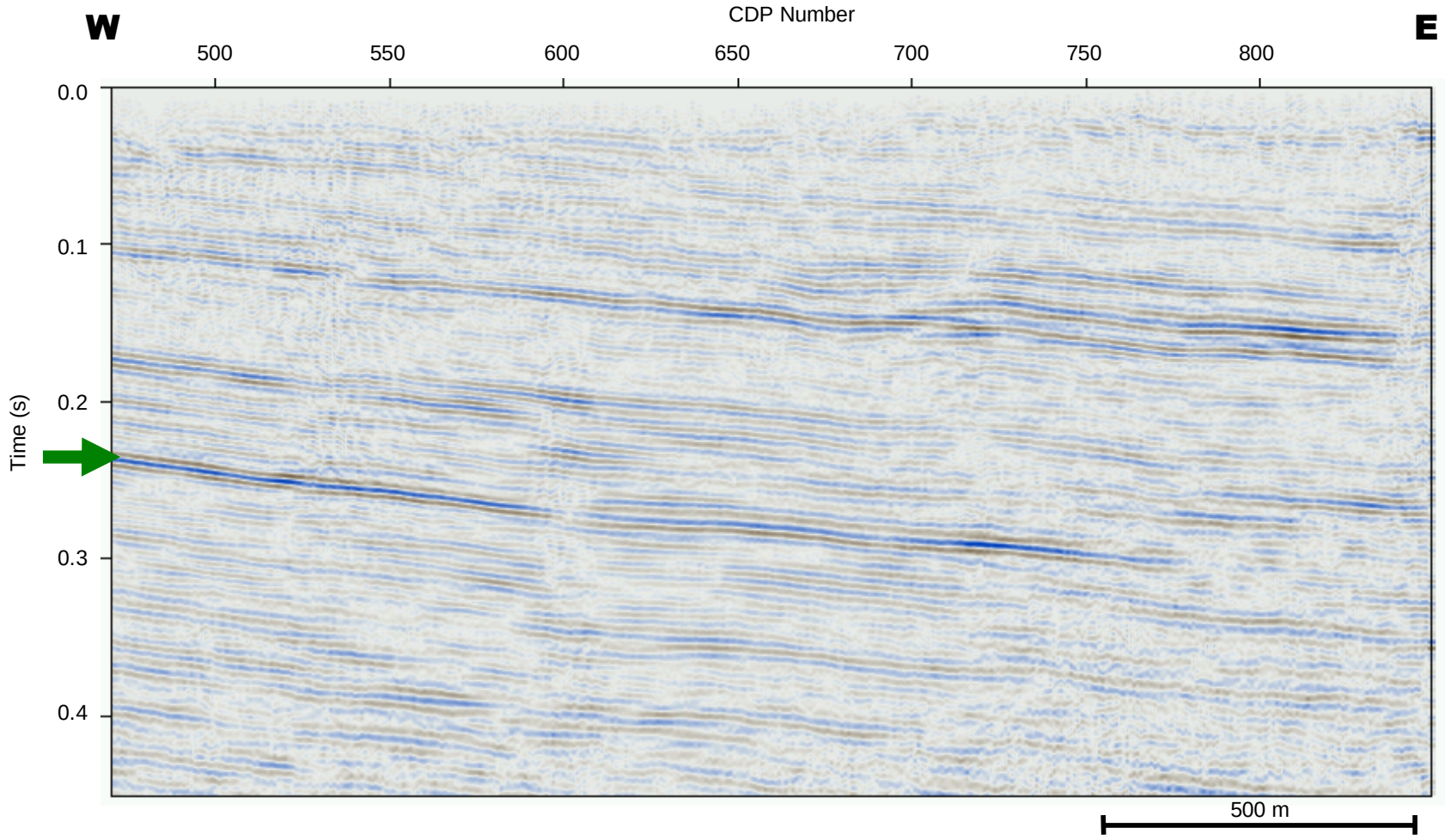

Figure 5.8 (a) P-wave seismic image derived from short-array data acquired in parallel to multi-component Trial Dataset #2. The target coal-seam reflector is indicated by the green arrow.

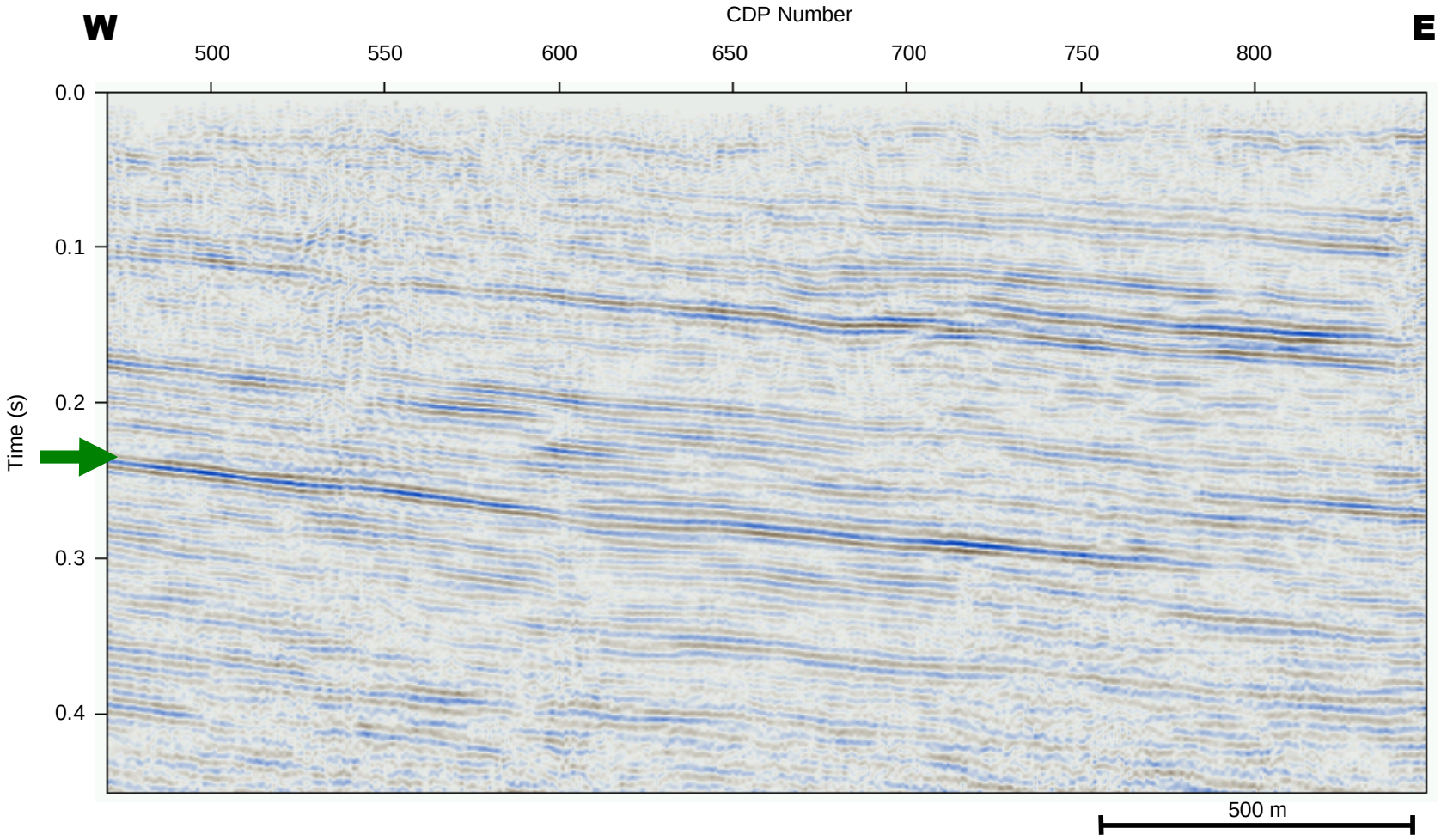

Figure 5.8 (b) P-wave image for the second trial site derived from the vertical component of the multi-component data. The target coal-seam reflector is indicated by the green arrow.

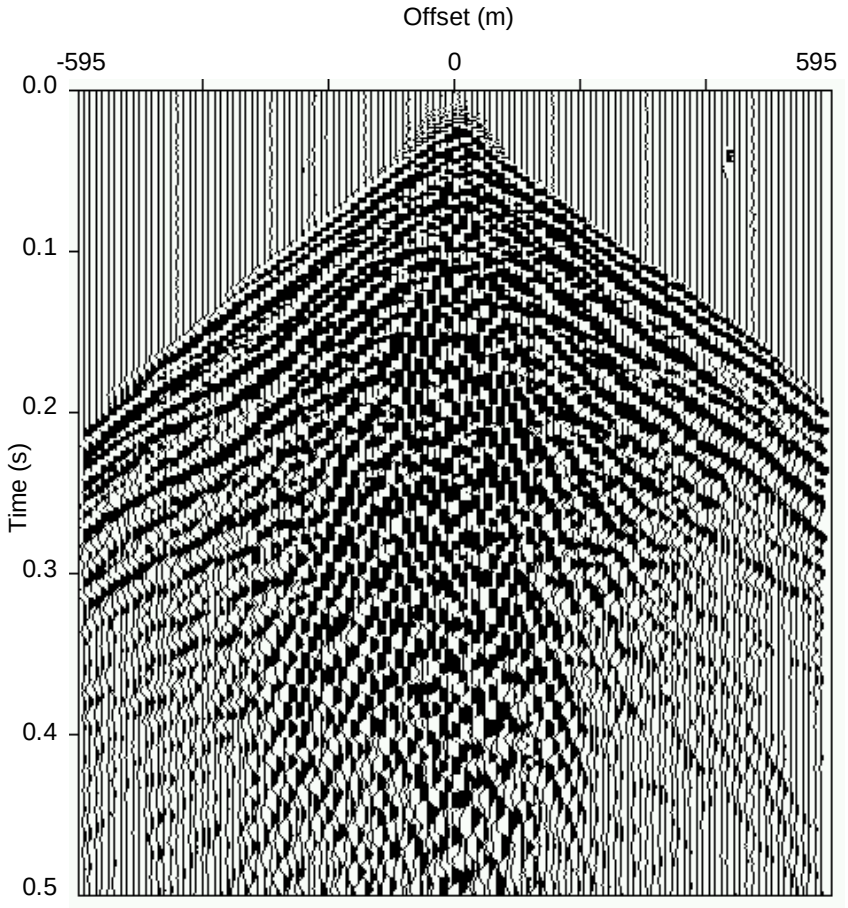

(a)

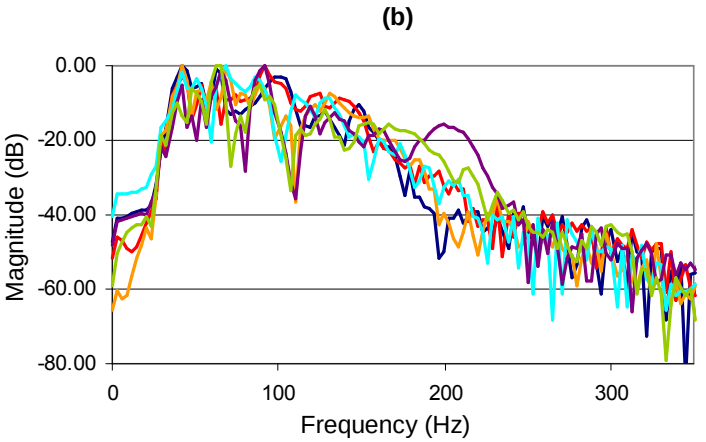

(b)

Figure 5.9 (a) Seismic field record acquired using an array of six 30 Hz / 375 ohm geophones over 2m; and (b) magnitude spectra of the first six channels of the displayed field record.

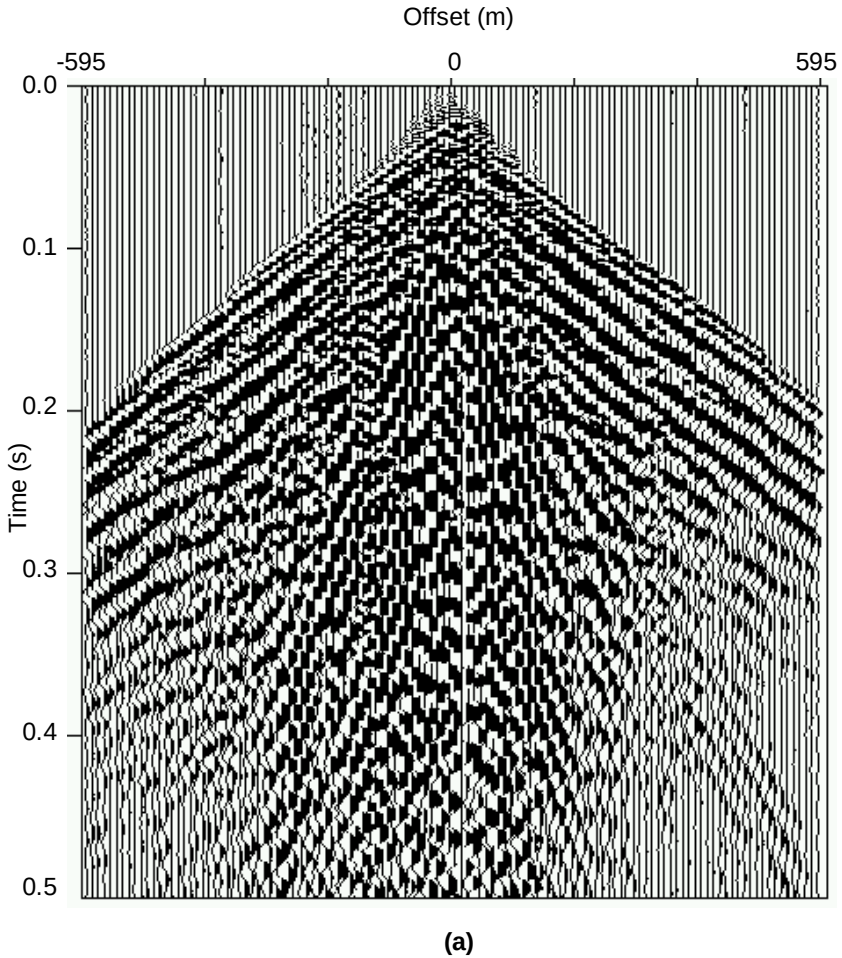

(a)

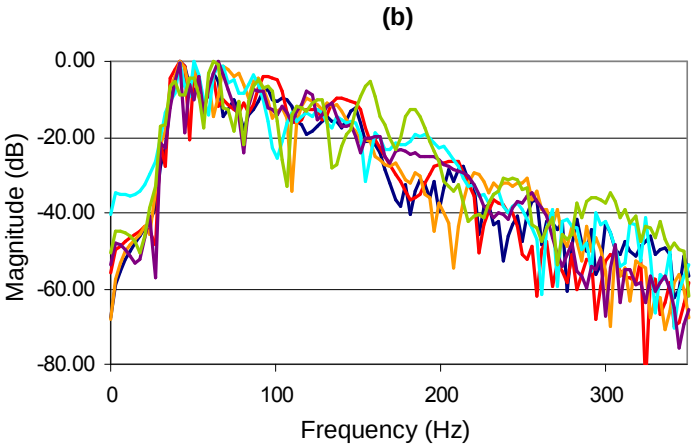

(b)

Figure 5.10 (a) Seismic field record acquired using the vertical component of single 3-C geophones (40 Hz / 430 ohm); and (b) magnitude spectra of the first six channels of the displayed field record.

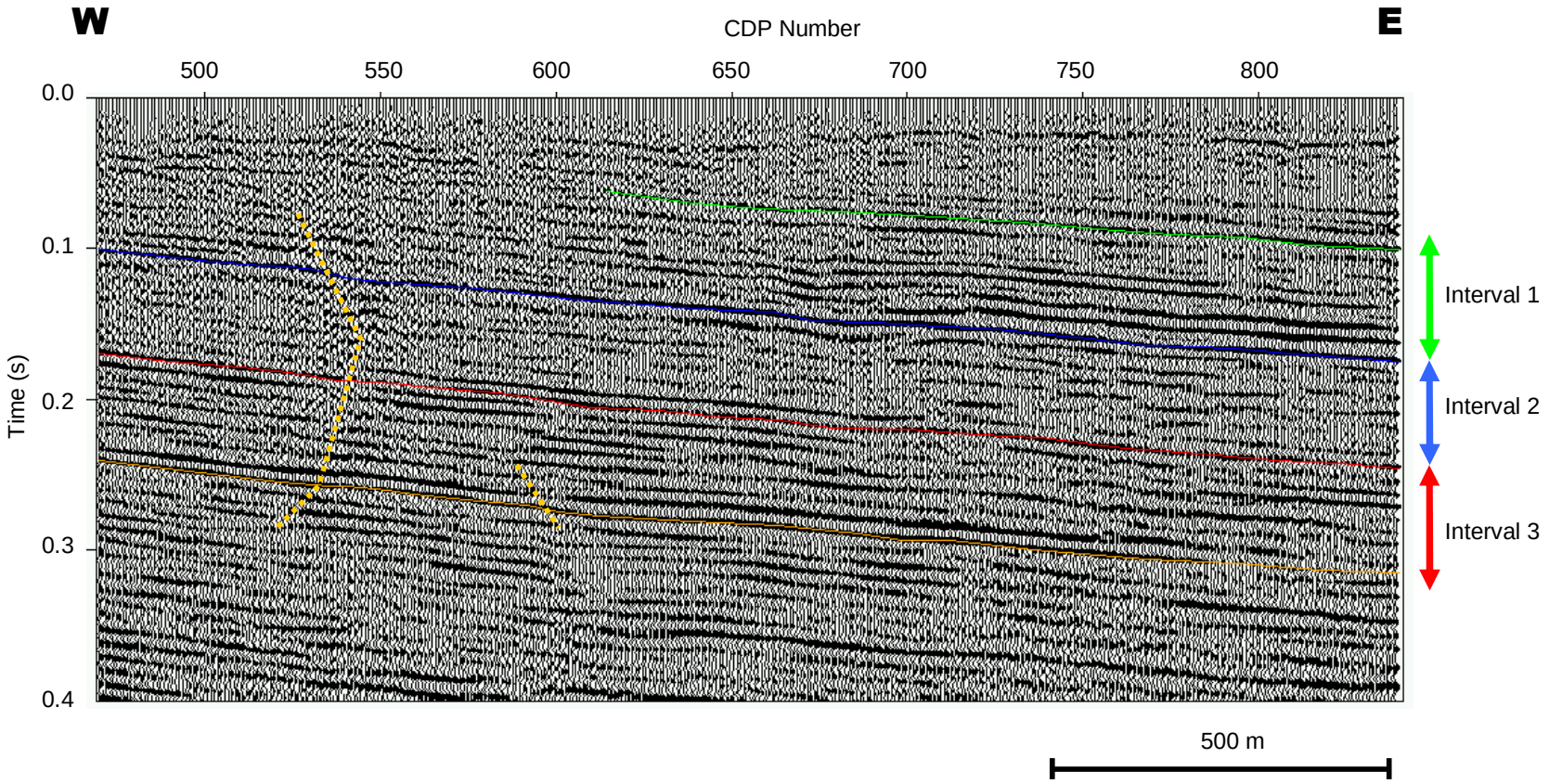

Figure 5.11 (a) Conventional P-wave image derived from the vertical component of the 3-C data acquired in the second trial area. The target coal-seam reflection event is marked in orange. Three shallower horizons have also been interpreted. The geological interval between the green and blue reflection horizons is believed to contain the thick band of interbedded high-ash coal, shales and mudstones affecting signal frequencies in the area. Interpreted faults are approximately marked.

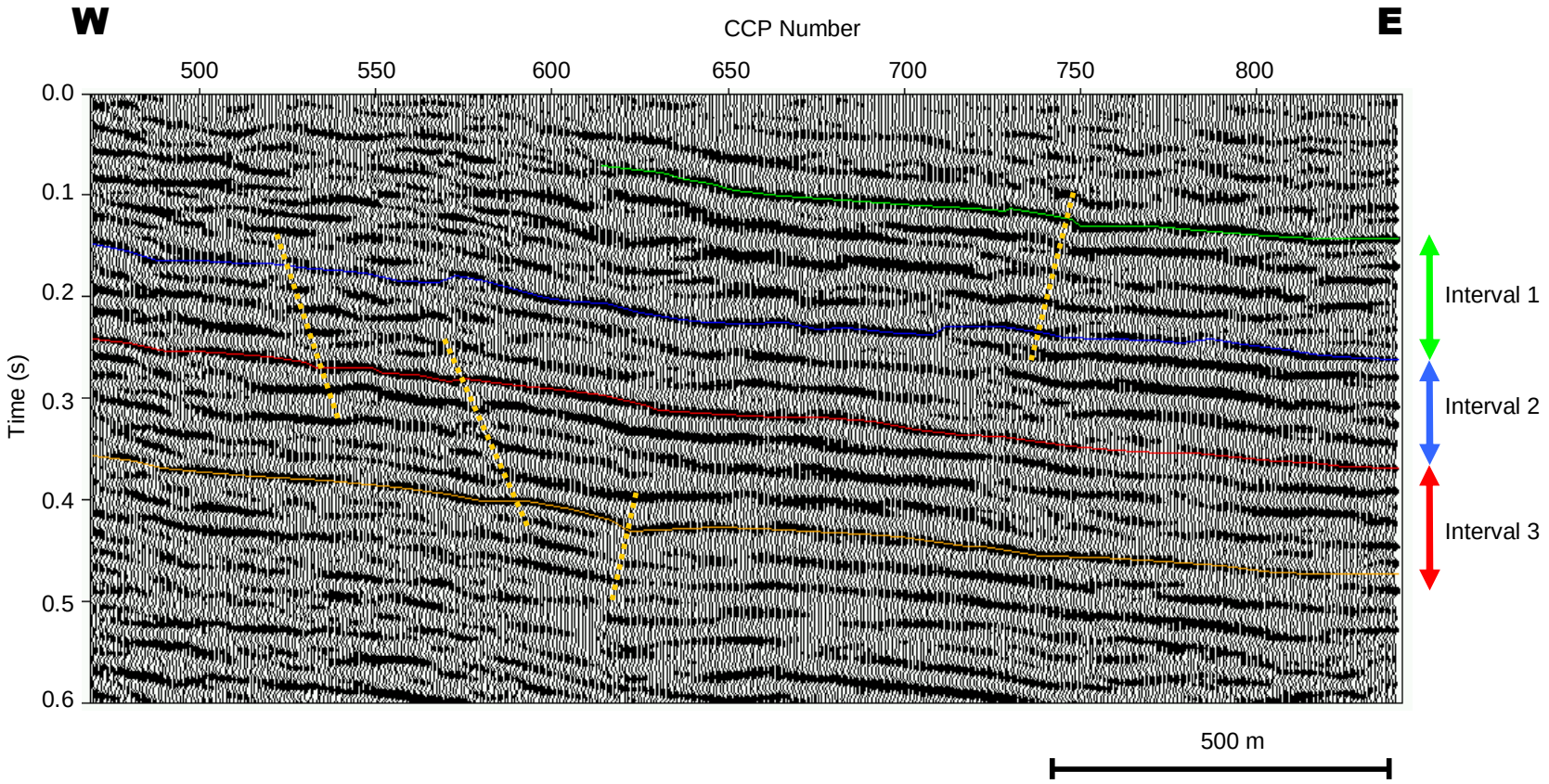

Figure 5.11 (b) Converted-wave (PS) image derived from the inline component of the 3-C data acquired in the second trial area. The target coal-seam reflection event is marked in orange. Three shallower horizons have also been interpreted. The geological interval between the green and blue reflection horizons is believed to contain the thick band of interbedded high-ash coal, shales and mudstones affecting signal frequencies in the area. Interpreted faults are approximately marked.

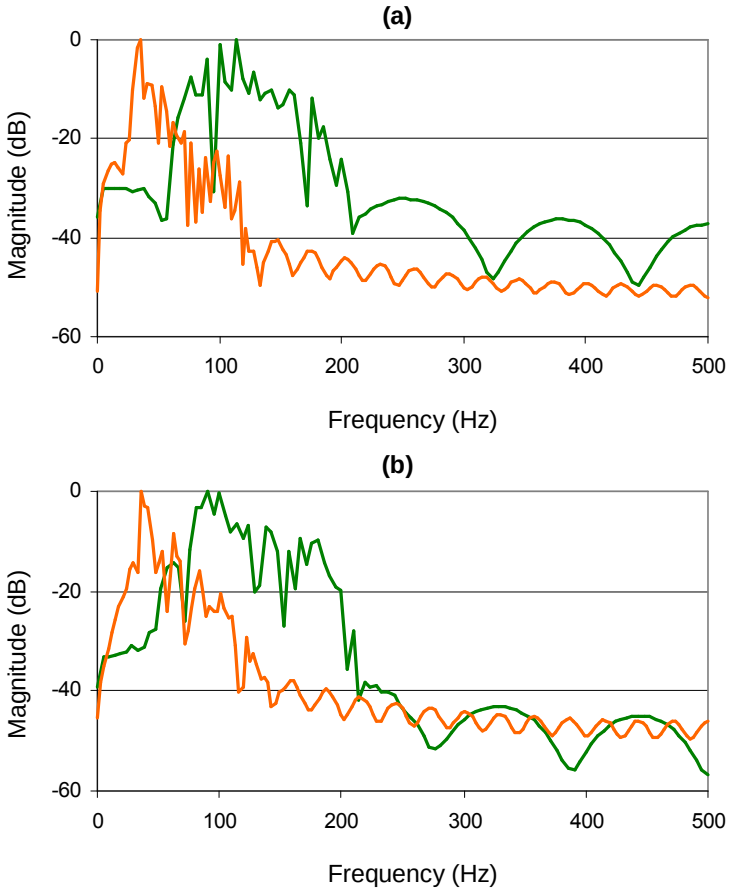

Figure 5.12 Comparison of trace spectra from the final P and PS sections shown in Figure 5.11 – (a) from the centre of the line; and (b) from the eastern end of the line. Magnitude spectra for the P-wave data are shown in green. Magnitude spectra for the corresponding PS data are shown in orange.

Note that the 'ringiness' of the final PS-wave section (Figure 5.11(b)) is related to the fact that the dominant frequency of the PS stack is approximately 40 Hz (Figure 5.12), and the three-component geophones used to acquire these data have a natural frequency of 40Hz. The geophones have effectively damped frequencies below 40Hz, resulting in a very narrow PS-energy frequency bandwidth. In this instance, since higher frequency S waves are not successfully reaching the surface, the only remedy for reducing 'ringiness' in the section would be to record the PS waves using geophones with a lower natural frequency. This would effectively broaden the frequency bandwidth of the converted waves at the lower end of the frequency spectrum, and should perhaps be considered for future multi-component acquisition in areas where significant loss of high-frequency S energy could be expected.

There are a variety of reasons that PS waves in this trial area may suffer significantly more high-frequency losses compared to those recorded in the first trial area. Geophone coupling and surface conditions could be expected to have an impact on the bandwidth of any recorded S waves. However, in this trial area, despite three 'zones' of surface conditions being recognised (Section 5.2), recall that no related variations in the PS frequency content along the line have been observed.

Consequently, it is believed that a thick sedimentary sequence located quite close to the surface (within 80m – see interpretation in Figure 5.11), and extending the full length of the line, is the primary reason for the observed loss of high-frequency S energy. This package of sedimentary material consists of thick bands of high-ash coal interbedded with layers of low-density / low-velocity carbonaceous shales and mudstones, and is thought to be significantly attenuating and scattering high-frequency energy from the upward travelling S waves. It is likely that this geological formation is also having similar effects on the P energy, although not to quite the same degree since the P and S waves propagate differently through the sub-surface (Section 1.2.1). Note that confirmation of this near-surface geological sequence being the cause of the high-frequency S-energy losses would only be possible with the acquisition of P- and S-wave sonic logs or a multi-component vertical seismic profile (VSP) along the seismic line.

Despite the fact that the PS image (Figure 5.11(b)) for this trial area does not provide greater vertical resolution than the P image (Figure 5.11(a)), the converted-wave data still have the potential to provide additional or complementary information about the sub-surface. For example, a number of very small faults have been interpreted on the conventional P-wave image. After correlating the dominant P and PS reflection horizons (Appendix E), structural interpretation of the PS image can validate or add to the structural information recovered from the P section. In this case, while the very small faults interpreted on the PS-wave stack do not align directly with those interpreted on the P section, they are supporting the notion that there are some structural ambiguities in the vicinity of CDPs 520 to 620. Some of these small discontinuities are more apparent on the PS section. However, these interpreted structures are pushing the lower boundaries of the resolution limit for both the P and PS data, and cannot be interpreted with any great confidence. Note also, that the PS section gives some indication of a small thrust structure in the shallow part of the section on the eastern end of the line. There is no evidence of this structure on the conventional P-wave section.

Recall that the discussion presented in Section 1.3 indicated that integrated P and PS interpretation, in addition to potentially enhancing structural interpretation, may also yield a richer geological characterisation of the sub-surface. While not the primary focus of this research project, here a preliminary attempt to extract additional lithological information from Trial Dataset #2 has been undertaken. Using the two-way times of the dominant seismic reflectors shown in Figure 5.11 it is possible to compute *Vp*/*Vs* (or equivalently, Poisson's Ratio) for various intervals down the geological section. A low *Vp*/*Vs* indicates a sequence with high sand content, while a high *Vp*/*Vs* indicates a shale or coal rich sequence. The former is also a potential indicator of the presence of gas. Figure 5.13 shows the computed *Vp*/*Vs* values for various geological intervals. As expected, the top interval, identified as the thick geological formation causing the loss of high frequency S energy, has a very high *Vp*/*Vs*. The interval between this formation and the first interpreted coal-seam reflection (Interval 2) shows a significant variation in *Vp*/*Vs* along the line. This interval appears to have an extremely high sand content along the western two-thirds of the line. The third interpreted interval (above the target coal seam) has a more consistent *Vp*/*Vs*, indicative of a shale-rich sequence. Note that at CCP 620, the *Vp*/*Vs* for the third interval increases abruptly for a short distance. This corresponds to the location of a small fault interpreted in the PS image (Figure 5.11(b)). Lateral variations in the *Vp*/*Vs* seismic attribute indicate the potential this method has for mapping lithology away from boreholes.

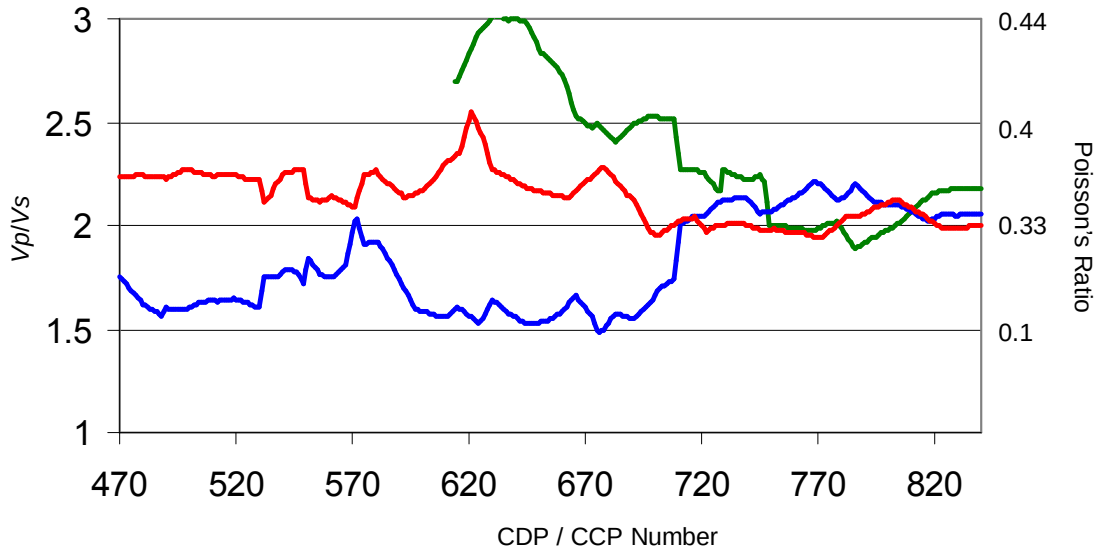

Figure 5.13 *Vp/Vs* for Interval 1 (green); Interval 2 (blue); and Interval 3 (red) interpreted on the P and PS images shown in Figure 5.11. A high Vp/Vs (greater than 2.2) corresponds to shale-rich layers or poorly consolidated material. A low Vp/Vs (less than 1.6) is indicative of high sand and/or gas content. As indicated on the right-hand axis, *Vp/Vs* is related to Poisson's Ratio.

CHAPTER SIX
DISCUSSION AND CONCLUSIONS

6.1 Motivation for this Research

The significant advances in 2D and 3D high-resolution seismic imaging over the past two decades have seen seismic reflection become the preferred geophysical tool for accurate and cost-effective imaging of coal seams. However, the desire to locate and characterise increasingly subtle structures and lithological features continues to drive research into alternative seismic technologies. This project has investigated the feasibility of using converted-wave technology as a tool for improving sub-surface imaging in the coal environment. The motivation for this research is largely provided by the success of multi-component seismic experiments in the petroleum sector. In terms of petroleum-scale structural interpretation, PS images have provided the opportunity to independently validate structures interpreted on conventional P-wave sections. In certain large offshore oilfields converted waves have been able to produce clearer or more coherent reflections than P waves to assist with structural interpretation. In the context of lithological interpretation, PS imaging has been exploited in the petroleum industry to produce predictions of lithology, porosity, fracturing and the presence of fluids. By analogy, multi-component seismic methods in the coal environment have the potential to contribute to lithology mapping, gas detection and the enhanced delineation of small structural features. To date, however, the technology has not been seriously tested in the coal sector.

This project represents the first attempts in Australia to utilise shallow, high-resolution multi-component seismic data and converted-wave technology to image coal seams. The logical starting point has been to demonstrate that acquisition of converted waves is viable in the coal environment, and that PS images can be successfully produced to provide independent structural information. These objectives have been achieved through the acquisition, processing and interpretation of two trial multi-component datasets. These geophysical concepts have been tested here via 2D seismic experiments, although the results are expected to translate to 3D seismic applications. The significant conclusions drawn from this research, together with suggestions for future research and development into multi-component coal seismic, are presented in the following sections.

6.2 Converted-Wave Seismic Imaging of Coal Structures

Modelling

Numerical modelling suggests that coal seams are efficient converters of P waves to S waves (Section 1.3.2). In fact, it is theoretically predicted that PS reflections from the top of a coal seam will be stronger than P reflections on the mid- to far-offsets of a typical coal-seismic survey (Figure 1.6). This suggests converted-wave acquisition may have particular relevance in the coal environment. Multi-component data acquired from the first trial area, on which the modelling results were based, confirm that the numerical modelling results are realistic.

Acquisition

The successful recording of converted-wave reflection energy from both trial areas demonstrates the viability of acquiring shallow, high-resolution PS data in different geological environments. Only minimal changes to conventional acquisition equipment and seismic surveying procedures have been needed to record both P and PS energy. A conventional dynamite source has been used, with

a single 3-C geophone replacing the conventional array of vertical geophones at each receiver station. As for conventional P-wave recording, local geology does influence the quality of the recorded PS seismic signal. Converted-wave data from Dataset #1 exhibit a much greater frequency bandwidth than the PS data acquired at the second trial area (see Figures 4.3 and 5.4). This is believed to be due to the more consolidated and uniform near-surface geology at the first trial area.

Processing

Standard converted-wave processing algorithms (Section 3.2) developed within the petroleum sector have been successfully applied to the two shallow, high-resolution trial datasets. This has involved specialised approaches to S-wave receiver statics, PS normal moveout (NMO) correction and common-conversion point (CCP) binning. Some experimentation to fine tune processing parameters and the processing sequence has been necessary. Significant effort was required to compute receiver static corrections for the two trial datasets. The hand-picked receiver static approach (Section 3.2.3) is preferred. In addition, extraction of a suitable *Vp*/*Vs* function was non-trivial and required significant geophysical input. Horizon-based CCP binning (Section 3.2.5) proved satisfactory for Trial Dataset #1, since the data are dominated by a single reflection event. However, processing of the second trial dataset, in which multiple coal-seam reflection events exist, required use of the more computationally expensive dynamic binning algorithm (Section 3.2.5). Overall the processing of the PS data has been significantly more challenging, and has required more geological input, than conventional P-wave processing.

Structural Interpretation

Despite logistical problems associated with extracting a converted-wave image, the final results from this project provide significant geophysical encouragement. PS images have been successfully produced from both trial datasets (see Figures 4.6 and 5.11), demonstrating the potential for converted-wave technology to provide independent and complimentary information about the shallow sub-surface. For both datasets the PS image exhibits a reduced frequency bandwidth compared to the corresponding P-wave data. This is consistent with petroleum-sector experience. In the case of Dataset #2, the reduction in frequency is significant (Figure 5.12) and there is a net decrease in the vertical resolution (Appendix D) of the PS image when compared to the conventional P-wave section. The poor resolution of these PS data is believed to be associated with local near-surface geology conditions. Nevertheless, the PS image does provide complimentary structural information about the sub-surface.

In contrast, the frequency content of the PS image from Trial Area #1 (Figure 4.8) is sufficient to yield greater vertical resolution (Appendix D), than the corresponding P-wave image. This supports predictions that have evolved from the petroleum sector that PS resolution improvements are more likely in the shallow environment due to shorter raypath lengths. This has positive implications for enhanced imaging of coal structures. Both of the final PS images generated during this project strongly suggest that converted-wave seismology has a significant role to play in structural imaging of the shallow coal environment.

6.3 Future Research and Development

Acquisition and Processing

To date, the geophysical concepts of using converted-wave seismology in the coal environment have been tested via 2D seismic experiments. Ultimately, however, it is expected that converted-wave technology will be exploited as an enhancement to 3D coal-seismic surveys. 3D converted-wave acquisition will necessarily require some adjustments to the field logistics developed for the 2D trials conducted as part of this project. Most significantly, 3D multi-component data will require a number of modifications to the processing procedures established during the course of this research. It is expected that significant logistical issues will have to be overcome due to the high level of interactivity and geological input required to currently produce an onshore converted-wave image.

While the near-surface conditions at Test Area #1 were conducive to relatively high-frequency S energy reaching the surface, Test Area #2 suffered from significant attenuation of high frequencies as a result of local geological conditions. This, coupled with the fact that the 3-C geophones used to acquire the trial data for this project have a natural frequency of 40 Hz, has resulted in the 'ringiness' of the PS image from the second trial area. The only remedy for reducing this 'ringiness' in this situation is to record the PS waves using geophones with a lower natural frequency. This would effectively broaden the frequency bandwidth of the converted-waves at the lower-end of the frequency spectrum, and should perhaps be considered for future multi-component acquisition in areas where significant loss of high-frequency S energy could be expected.

During the course of this research, it has become apparent that converted waves are more significantly influenced by lithological factors than P waves. For example, PS reflection events in both datasets have been found to be non-symmetric (i.e. reflection times to geophones on opposite sides of the shot point are different). This is believed to be caused by inhomogeneities in the sub-surface. Reflector dip and/or seismic anisotropy may also contribute to this observed behaviour. While the PS processing flows implemented for this project have simply worked around this peculiarity by stacking only positive or negative offset traces, further investigation is needed. It may be possible that understanding and interpreting such peculiar PS-wave propagation behaviours will contribute to the geological characterisation of the sub-surface. Furthermore, advanced PS processing algorithms (such as PS dip moveout corrections or PS pre-stack migration) may be able to accommodate these types of peculiarities, and contribute to an improved PS image.

It is well documented that PS waves can split and rotate into fast and slow modes when propagating through near-vertical fractures. This would lead to PS energy being recorded on both the inline and crossline components of data. Only the inline component of data has been used to derive the PS images presented here since no significant energy was immediately obvious on the crossline component. However, further analysis is needed to determine whether the crossline component of data can contribute to the converted-wave image and/or be used for detecting zones of significant fracturing.

Recall that in some situations P-wave energy can leak onto the horizontal component(s) and S waves can leak onto the vertical component of data. Synthetic examples have been used here to demonstrate that vector-processing methods can remove such wavefield cross-contamination, resulting in cleaner P and PS pre-stack gathers. However, the stacking process itself has been

shown to be a very powerful tool for suppressing P/S cross-contamination. Since the structural interpretation of stacked images has been the focus of this project, vector processing has not been required in the PS processing flow. However, it is likely that vector processing may be relevant for future studies designed to extract lithological information from integrated P and PS interpretation where pre-stack analysis would play a more critical role.

Towards Integrated P and PS Lithological Interpretation

Based on previous experiences in the petroleum sector, PS images have the potential to yield a richer geological characterisation of the sub-surface, in addition to enhancing structural interpretation. While not the primary focus of this research project, some preliminary results from integrated P and PS interpretation, aimed at demonstrating the processes used to derive lithological information, have been presented here. Relative P and PS amplitudes have been extracted from the first trial dataset (Figure 4.7). Variations in the ratio of the P-to-S amplitudes are commonly used in the petroleum sector as gas/fluid indicators. The amplitude variations observed in the first trial dataset are considerable, and further investigation into their significance is warranted. Perhaps the most powerful integrated interpretation tool is the prediction of *Vp*/*Vs* (or equivalently, Poisson's Ratio) from correlated P and PS seismic sections. The *Vp*/*Vs* function can be used to map lithologies and has been demonstrated for the second trial dataset (where multiple reflection events are available) (Figure 5.13). Again, considerable variation of this attribute is observed along the line, indicating the potential this method has for mapping lithology away from boreholes. However, further investigation is required to assess the full significance of the *Vp*/*Vs* variations in terms of real geology.

6.4 Conclusion

The overall objective of this research has been to demonstrate the viability of using converted-wave technologies in the coal environment, and to assess the potential of PS images to contribute to imaging of the sub-surface. Prior to this study, converted-wave technologies had been untested in the context of coal-seismic imaging in Australia. The results achieved in this first study provide a compelling argument that converted-wave seismology will evolve to become a cost-effective enhancement to conventional 3D seismic reflection. From an acquisition viewpoint the technology is attractive in that relatively minor adjustments to current practice are needed. The development of a robust and cost-effective processing methodology is seen as a greater challenge. Prior geophysical history would, however, suggest that this will be achieved with further experience.

Future research should be aimed at understanding PS-wave propagation behaviour, tuning processing algorithms to improve PS image resolution, and demonstrating the practical implications of integrated P and PS interpretation. Such research will stimulate additional methodological advances, and ultimately lead to the use of converted-wave seismology as a standard coal-imaging tool.

REFERENCES

Barkved, O.I., Mueller, M.C., and Thomsen, L., 1999. Vector interpretation of the Valhall 3D/4C OBS dataset: EAGE 61st Conference and Technical Exhibition, Extended Abstracts, #6-42.

Begay, D.K., Miller, R.D., Watney, W.L., and Xia, J., 2000. High-resolution P- and S-wave reflection to detect a shallow gas sand in southeast Kansas: SEG 70th Ann. Int. Mtg., Expanded Abstracts (CD-ROM).

Brown, R.J., Stewart, R.R., and Lawton, D.C., 2002. A proposed polarity standard for multicomponent seismic data: Geophysics 67, 1028-1037.

Cary, P.W., and Eaton, D.W.S., 1993. A simple method for resolving large converted-wave (P-SV) statics: Geophysics **58**, 429-433.

Cohen, J.K., and Stockwell, Jr. J.W., 2002. CWP/SU Seismic Unix Release 36 - a free package for seismic research and processing: Centre for Wave Phenomena, Colorado School of Mines.

CREWES (Consortium for Research in Elastic Wave Exploration Seismology) Research Collection, 2002 – 2 CD Set: University of Calgary, Calgary.

Dasios, A., McCann, C., Astin, T.R., McCann, D.M., and Fenning, P., 1999. Seismic imaging of the shallow subsurface: shear-wave case histories: Geophys. Prosp. **47**, 565-591.

Engelmark, F., 2001. Using 4-C to characterize lithologies and fluids in clastic reservoirs: The Leading Edge, **20**, 1053-1055.

Fertig, J., and Müller, G., 1978. Computation of synthetic seismograms for coal seams with the reflectivity method: Geophys. Prosp. **26**, 868-883.

Garotta, R., 1999. Shear Waves from Acquisition to Interpretation: Distinguished Instructor Series #3, Society of Exploration Geophysicists, Oklahoma.

Granli, J.R., Arntsen, B., Sollid, A., and Hilde, E., 1999. Imaging through gas-filled sediments using marine shear-wave data: Geophysics, **64**, 668-677.

Greenhalgh, S.A., Suprajitno, M., and King, D.W., 1986. Shallow seismic reflection investigations of coal in the Sydney Basin: Geophysics **51**, 1426-1437.

Gochioco, L.M., 2000. High-resolution 3-D seismic survey over a coal mine reserve area in the U.S. – A case study: Geophysics **65**, 712-718.

Hanson, R.A., Macleod, M.K., Bell, C.R., Thompson, C.J., and Somod, J., 1999. Multicomponent seismic interpretation – data integration issues, Alba Field, North Sea: EAGE 61st Conference and Technical Exhibition, Extended Abstracts, #6-27.

Harris, J.B., Miller, R.D., Xia, J., Hunter, J.A., Park, C.B., Laflen, D.R., and Good, R.L., 2000. Near-surface shear wave reflection surveys in the Fraser River delta, B.C., Canada: SEG 70th Ann. Int. Mtg., Expanded Abstracts (CD-ROM).

Harrison, M.P., 1992. Processing of P-SV Surface-Seismic Data: Anisotropy Analysis, Dip Moveout, and Migration: PhD Thesis, The University of Calgary.

Hatherly, P., Poole, G., Mason, I., Zhou, B., and Bassingthwaighte, H., 1998. 3D seismic surveying for coal mine applications at Appin Colliery, NSW: Exploration Geophysics **29**, 407-409.

Hearn, S., and Hendrick, N., 2000. Demystifying coal seismic resolution: a modelling approach: *in* Beeston, J.W. (Ed) Bowen Basin Symposium 2000 – The New Millennium – Geology: Geological Society of Australia Inc. Coal Geology Group and the Bowen Basin Geologists Group, Rockhampton, October 2000, 243-248.

Hearn, S., and Hendrick N., 2001. Bandwidth requirements for shallow, high-resolution seismic reflection: ASEG 15th Geophysical Conference and Exhibition, Preview Abstracts, August 2001.

Hendrick, N., 2001. Integration and Demonstration of Parametric Techniques for Multi-Component Seismic Wavefield Separation: PhD, The University of Queensland.

Henson, H. Jr. and Sexton, J.L., 1991. Premine study of shallow coal seams using high-resolution seismic reflection methods: Geophysics **56**, 1494-1503.

Hoffe, B.H., Margrave, G.F., Stewart, R.R., Foltinek, D.S., Bland, H.C., and Manning, P.M., 2002. Analysing the effectiveness of receiver arrays for multicomponent seismic exploration: Geophysics **67**, 1853-1868.

Kendall, R.R., Gray, S.H., and Murphy, G.E., 1998. Subsalt imaging using prestack depth migration of converted waves: Mahogany Field, Gulf of Mexico: SEG 68th Ann. Int. Mtg., Expanded Abstracts (CD-ROM).

Kennett, B.L.N., 1991. Elastic Waves in Reflection Seismology: Research School of Earth Sciences, Australian National University, Canberra.

Lewis, C., Davis, T.L., and Vuillermoz, C., 1991. 3-D multicomponent imaging of reservoir heterogeneity, Silo Field, Wyoming: Geophysics, **56**, 2048-2056.

Li, X-Y., MacBeth, C., Hitchen, K., and Hanßen, P., 1998. Using converted shear-waves for imaging beneath basalt in deep water plays: SEG 68th Ann. Int. Mtg., Expanded Abstracts (CD-ROM).

MacBeth, C., and Crampin, S., 1991. Comparison of signal processing techniques for estimating effects of anisotropy: Geophys. Prosp. **39**, 357-385.

MacLeod, M.K., Hanson, R.A., Bell, C.R. and McHugo, S., 1999. The Alba Field ocean bottom cable seismic survey: Impact on development: The Leading Edge, **18**, 1306-1312.

Metcalfe, T., 2002. An Evaluation of Wavefield Separation Techniques Applied to Multi-Component Seismic Data: Honours Thesis, The University of Queensland.

Potters, J.H.H.M., Groenendaal, H.J.J., Oates, S.J., Hake, J.H., and Kalden, A.B., 1999. The 3D shear experiment over the Natih field in Oman. Reservoir geology, data acquisition and anisotropy analysis: Geophys. Prosp. **47**, 637-662.

Rognø, H., 1999. The Statfjord 3-D, 4-C OBC survey: The Leading Edge, **18**, 1301-1305.

Sheriff, R.W., 1991. Encyclopedic Dictionary of Exploration Geophysics, Society of Exploration Geophysicists, Oklahoma.

Sheriff, R.E., and Geldart, L.P., 1995. Exploration Seismology: Cambridge University Press, Cambridge.

Stewart, R.R., Gaiser, J.E., Brown, R.J., and Lawton, D.C., 2002. Tutorial: Converted-wave seismic exploration – Methods: Geophysics **67**, 1348-1363.

Thomsen, L., 1988. Reflection seismology over azimuthally anisotropic media: Geophysics **53**, 304-313.

Thomsen, L., 2002. Understanding Seismic Anisotropy in Exploration and Exploitation: Distinguished Instructor Series #5, Society of Exploration Geophysicists, Oklahoma.

Tselentis, G.A. and Paraskevopoulos, P., 2002. Application of a high-resolution seismic investigation in a Greek coal mine: Geophysics **67**, 50-59.

Urosevic, M., and Evans, B.J., 1996. The role of 3-C seismic in longwall mine planning: SEG 66th Ann. Int. Mtg., Expanded Abstracts, 642-645.

Urosevic, M., Evans, B.J., and Hatherly, P.J., 1992. Application of 3-D seismic methods to detection of subtle faults in coal seams: SEG 62nd Ann. Int. Mtg., Expanded Abstracts, 254-256.

Walton, C.H., Evans, B.J. and Urosevic, M., 1999. Seismic methods for delineating complex structures in coal seams: SEG 69th Ann. Int. Mtg., Expanded Abstracts (CD-ROM).

Yilmaz, 0., 1987. Seismic Data Processing: Society of Exploration Geophysicists, Oklahoma.

Zhang, Y., 1992. Common Conversion Point Stacking for P-SV Converted Waves: PhD, The University of Tulsa.

Zhang, Y., 1996. Nonhyperbolic converted wave velocity analysis and normal moveout: SEG 66th Ann. Int. Mtg., Expanded Abstracts, 1555-1558.

GLOSSARY

This glossary contains explanations of technical terms and acronyms commonly used to describe multi-component seismic processing and interpretation. More comprehensive explanations can be found in standard seismic texts and reference books (e.g. Sheriff, R.E. (1991) Encyclopedic Dictionary of Exploration Geophysics, Society of Exploration Geophysicists, Oklahoma).

2D	two-dimensional
3D	three-dimensional
3-C	three-component; typically refers to the vertical and two orthogonal horizontal components of ground motion recorded by a 3-C geophone
AGC	automatic gain control; data dependent scaling designed to normalise trace amplitude within a running time window
anisotropy	variation of seismic velocity depending on the direction in which it is measured; a sequence of sedimentary bedding produces polar anisotropy (where seismic velocities are symmetric about axis perpendicular to the bedding); non-horizontal fracturing and microcracks produces azimuthal anisotropy (where seismic velocities are symmetric about the axis perpendicular to the fracturing)
angle of incidence	the angle (with respect to the vertical axis) at which seismic energy arrives at a geological boundary
bandpass filter	attenuation of seismic energy outside of a user-defined frequency bandwidth
binning	the process by which all traces sharing the same sub-surface reflection point are grouped together; typically referred to as CMP binning for conventional P data, and CCP binning for PS data
CCP stacking	the summation of all traces within a CCP gather
CMP stacking	the summation of all traces within a CMP gather
common conversion point (CCP) gather	a collection of (usually horizontal component) seismic traces sharing the same sub-surface P-to-S conversion point; the location of the wavefield conversion point is a function of Vp/Vs and the depth of the boundary at which the conversion occurs
common midpoint (CMP) gather	the set of (usually vertical component) seismic traces that share the same midpoint between their sources and receivers
common receiver gather (CRG)	a collection of seismic traces recorded at the same geophone (receiver) location, generated by sources at a variety of locations
converted waves	seismic waves that travel down to a geological boundary as a P wave, get partially converted to S energy at the boundary, and then travel back to the surface as an S wave; also referred to as PS waves

CRG stack	the resultant seismic section produced by summing all traces within each CRG, and displaying the summed traces in receiver-location order
crossline component	seismic energy recorded using a geophone that measures the horizontal component of ground motion perpendicular to the line of recording
dominant frequency	the predominant frequency of a seismic dataset determined by measuring the time between successive peaks or troughs of the recorded seismic pulse, and taking the reciprocal
dominant wavelength	the seismic wavelength associated with the dominant frequency; for P waves, equivalent to Vp divided by the dominant frequency; for S waves a more complicated expression involving both Vp and Vs, and P- and S-wave dominant frequencies is required
frequency	the repetition rate of a periodic waveform, measured in 'per second' or Hertz (Hz)
frequency bandwidth	range of frequencies over which the recorded seismic signal has maximum power
geophone	the recording device or receiver used to transform seismic energy into an electrical voltage for input into the seismic recording system; a single vertically-oriented geophone is used for conventional seismic acquisition; three mutually orthogonal geophones are used when recording 3-C data
geophone array	see receiver array
groundroll	a type of seismic wave that travels along or near the surface of the ground; characterised by relatively low velocity, low frequency and high amplitude; seen as a steeply dipping, linear event on a seismic shot record
inline component	seismic energy recorded using a geophone that measures the horizontal component of ground motion parallel to the line of recording
lithological interpretation	used here to describe efforts to extract more detailed geological character in terms of lithology, fluids and fractures etc
magnitude spectrum	amplitude of seismic recording as a function of frequency
multi-component acquisition polarity standard	right-handed coordinate system where z (vertical direction) is positive downward; x (inline direction) is positive in the forward line direction for a 2D survey; and y (crossline direction) is positive in the direction 90^{o} clockwise from x.
multi-component recording	seismic recording that measures both the vertical and horizontal components of ground motion at the receiver; also referred to as 3-C recording
mute	elimination of unwanted energy from seismic traces; typically used over certain time intervals to remove groundroll or noise bursts out of the final stack

normal moveout (NMO)	the variation of the arrival time of reflection energy with offset; NMO corrections compensate for this variation in traveltime so that reflection energy from each geological boundary is properly aligned prior to stacking; for horizontal reflectors, P-wave NMO can be described as hyperbolic; the NMO for PS-waves is always non-hyperbolic
offset	the distance from the source point to the receiver location
P waves	longitudinal or compressional seismic waves; characterised by particle motion in the direction of travel; acquired using conventional (single-component) seismic acquisition surveys
receiver array	a group of geophones planted in a linear or areal pattern connected to a single recording channel; generally used to attenuate unwanted surface-wave noise and boost the signal-to-noise ratio
residual static corrections	corrective time shifts applied to the data to compensate for remnant statics associated with incomplete weathering static corrections
resolution	the ability to separate two features which are very close together
resolution limit	for discrete seismic reflectors, the minimum separation so that one can ascertain that more than one interface is involved; the commonly used Rayleigh resolution limit is defined as one quarter the dominant wavelength; the Widess limit is defined as one eighth the dominant wavelength
S waves	transverse or shear seismic waves; characterised by particle motion perpendicular to the direction of travel; acquired using multi-component (3-C) seismic acquisition
seismic waves	sound waves that propagate through the earth
seismic modelling	generation of a synthetic seismic record given an earth model
seismic reflection	a geophysical method to image the sub-surface using artificially-generated sound waves; typically the arrival times of various seismic waves are used to map sub-surface structure
seismic source	an artificial device that releases energy or seismic waves into the ground; typical coal-seismic sources include small dynamite explosions, MiniSOSIE and Vibroseis
seismic velocity	the propagation rate of a seismic wave through a particular material
shot record	a collection of seismic traces recorded from the release of seismic energy at a single source location
signal-to-noise ratio (S/N)	the ratio of desired signal to all other recorded energy (noise) in a seismic recording; difficult to determine in practice
single-component recording	conventional seismic acquisition that records only the vertical component of ground motion at the receiver

spherical divergence correction	a scaling correction to compensate for decrease in wave strength with distance as a result of geometric spreading
stacking	process by which a set of seismic traces are summed
static corrections	corrective time shifts applied to seismic data to compensate for the effects of variations in elevation, weathering thickness, weathering velocity or reference to datum; the objective is to determine the arrival times which would have been observed if all measurements had been made on a flat plane with no weathering or low-velocity material present
structural interpretation	involves the mapping of geological interfaces and discontinuities (such as faults)
trim statics	corrective time shifts applied to NMO-corrected CMP or CCP gathers prior to stacking; designed to optimally align flattened reflection events
TWT	two-way traveltime; refers to the time it takes for seismic energy to travel from the seismic source, down to a reflector, and back to the surface receiver
vector processing	simultaneous use of two or more components of multi-component seismic data to separate P and S energy
velocity analysis	calculation of a velocity that will accurately compensate for the effects of NMO; typically involves flattening reflection events in a CMP or CCP gather
vertical component	the seismic energy recorded using a geophone that measures the vertical component of ground motion
Vp	P-wave seismic velocity
Vs	S-wave seismic velocity
Vp/Vs	ratio of P-wave to S-wave seismic velocity; directly related to Poisson's Ratio

APPENDIX A
RESEARCH TEAM

Research team members who contributed to the results of ACARP Project C10020:

Dr Steve Hearn (*Project Leader*)	(Chief Geophysicist – Velseis Pty Ltd)
Dr Natasha Hendrick	(Research & Development Geophysicist – Velseis Pty Ltd)
John McMonagle	(Research & Development Geophysicist – Velseis Pty Ltd)
Daryn Voss	(Geophysicist – Velseis Pty Ltd)
Mike Reveleigh	(Operations Manager – Velseis Pty Ltd)
Tim Beale	(Field Operations Manager – Velseis Pty Ltd)
Gerard Wells	(Senior Observer – Velseis Pty Ltd)
Thabo Metcalfe	(Honours Student – University of Queensland)

APPENDIX B
P AND PS PROCESSING FLOWS

The P and PS processing flows shown here outline the general approach used to process the P and PS wave data presented in this report. Precise details on the processing sequences used to produce the converted-wave images from the two project trial areas can be found in Chapters 4 and 5. Further information on conventional P-wave processing can be found, for example, in Yilmaz (1987).

Conventional P-Wave Processing Flow

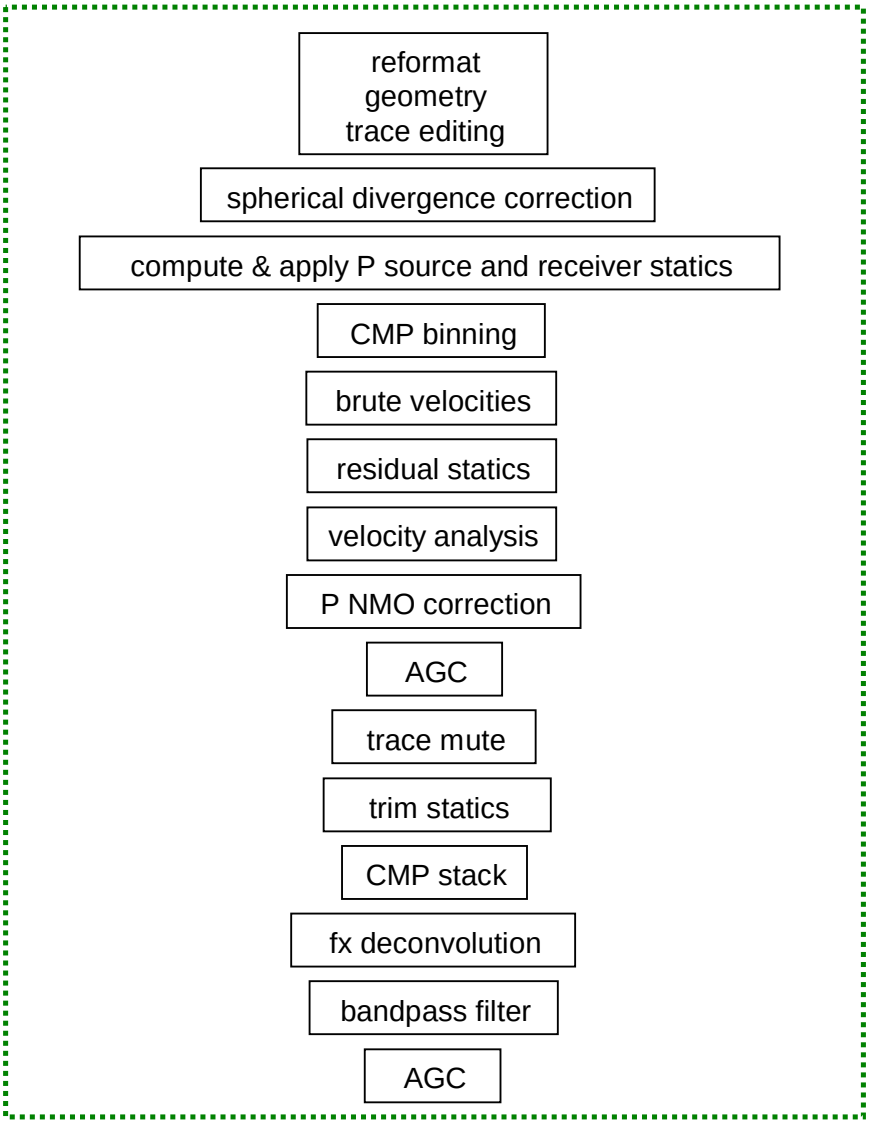

Converted-Wave Processing Flow

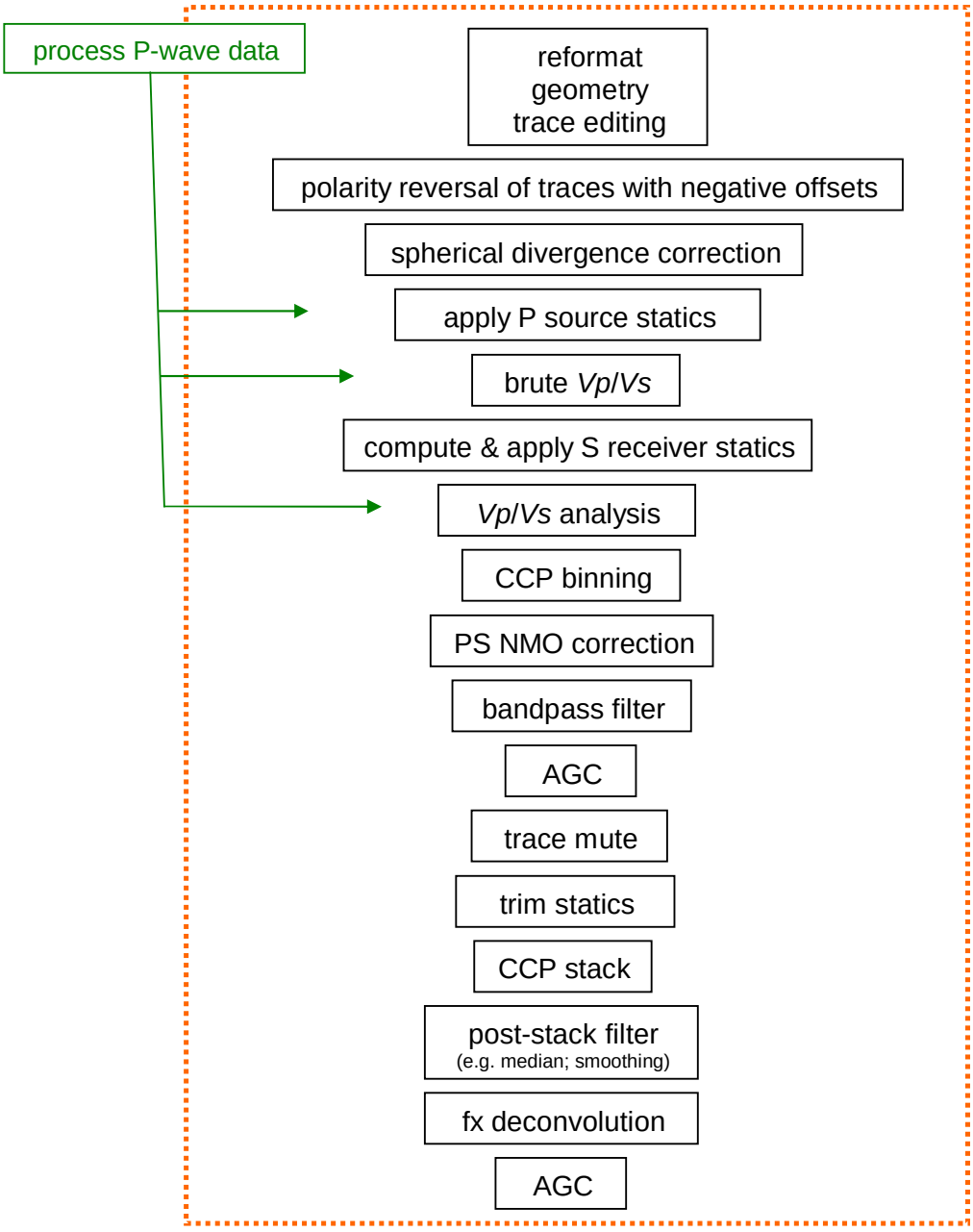

APPENDIX C
PS-WAVE VELOCITY ANALYSIS, NORMAL MOVEOUT AND COMMON-CONVERSION POINT BINNING

This summary of converted-wave velocity analysis, normal moveout (NMO) and common-conversion point (CCP) binning is largely based on Zhang (1996).

Figure C-1 illustrates the asymmetric raypath geometry of a PS wave.

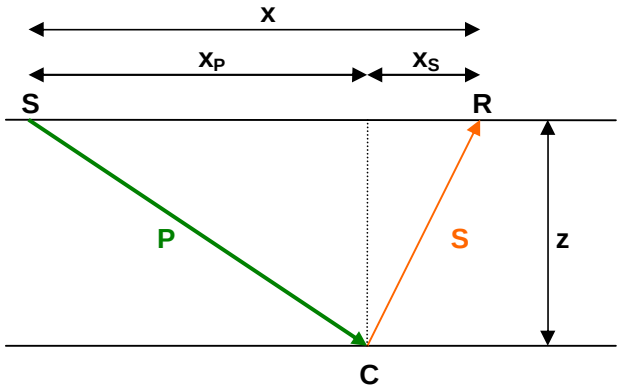

Figure C-1 Raypath geometry of PS wave. A P wave travels down from the source (S) to a geological boundary where it is partially converted to an S wave (at point C), before travelling back to the surfaces as an S wave to the receiver (R). (After Zhang,1996).

The non-hyperbolic PS-wave traveltime equation can be written as:

$$t_{PS}(x) = \frac{1}{Vp}\sqrt{x_P^2 + z^2} + \frac{1}{Vs}\sqrt{(x - x_P)^2 + z^2}\ , \qquad (1)$$

where *Vp* and *Vs* are the P- and S-wave velocities, respectively, *x* is the source-to-receiver offset, x_P is the conversion distance (defined as the horizontal distance between the source point and the conversion point), and *z* is the depth of the reflector.

Equation (1) can also be written as:

$$t_{PS}(x) = \frac{1}{Vp}\left(\sqrt{x_P^2 + z^2} + \gamma\sqrt{(x - x_P)^2 + z^2}\right), \qquad (2)$$

where $\gamma = Vp/Vs$ is the ratio of the P-wave to S-wave velocity. Note that the P-wave velocities (*Vp*) are extracted from the conventional P-wave processing sequence (e.g. Yilmaz, 1987).

For the simple case of a single, horizontal layer, the depth of the reflector, z, can be expressed in terms of the zero-offset PS traveltime ($t_{PS}(0)$):

$$z = \frac{1}{\gamma + 1} t_{PS}(0) Vp \,. \tag{3}$$

The conversion distance, x_P, is given by the following equation (Zhang, 1992):

$$x_P = \frac{\sqrt{\gamma^2 + \left(\frac{x_P}{z}\right)^2 \left(\gamma^2 - 1\right)}}{1 + \sqrt{\gamma^2 + \left(\frac{x_P}{z}\right)^2 \left(\gamma^2 - 1\right)}} x \,. \tag{4}$$

Substituting Equation (3) into Equation (4) produces an expression that can be solved iteratively for the conversion distance, x_P. In practice, this requires an initial value of x_P to be substituted into the right-hand side of Equation (4). Generally the asymptotic approximation to x_P is used for this initial value:

$$x_P = \left(\frac{\gamma}{1+\gamma}\right) x \,,$$

where x is the source-to-receiver offset. The iterative process of computing a new x_P by inserting the previously calculated value of x_P into the right-hand side of Equation (4) is continued until the conversion criteria:

$$\frac{\left(x_{Pnew} - x_{Pold}\right)}{x_{Pold}} < \varepsilon$$

is met. Here ε is set to some small number.

The conversion distance, x_P, is the parameter that must be calculated when determining the location of the common-conversion points (CCPs) for trace binning. When performing 'horizon-based CCP binning', the zero-offset PS traveltime in Equation (3) is the traveltime to the target horizon, and γ is the P-wave to S-wave velocity ratio at that target-horizon time. This method allocates one CCP bin location for each seismic trace. When 'dynamic CCP binning' is implemented, the zero-offset PS traveltime is considered at each time sample in turn, and γ is the corresponding *Vp*/*Vs* value at that time. Thus each time sample in each trace is allocated to a CCP bin location.

If both Equations (3) and (4) are substituted into Equation (2), and the appropriate *Vp*/*Vs* information is available, it is possible to compute the offset-dependent traveltime of a PS reflection event. This in turn enables computation of the normal moveout (NMO) correction:

$$\Delta t_{PSNMO} = t_{PS}(x) - t_{PS}(0).$$

Note that the relevant *Vp*/*Vs* information required for computing $t_{PS}(x)$ via Equation (2) is the output of the PS-wave velocity analysis process. This essentially involves using trial and error to determine the optimal P-wave to S-wave velocity ratio.

The above derivation assumes a single horizontal layer. Similar expressions for x_P and $t_{PS}(x)$ can be derived for converted waves travelling through a more realistic, multi-layered medium (Zhang,1996).

APPENDIX D
SEISMIC RESOLUTION

Measurements of Resolution

There are a number of quasi-theoretical measures of vertical resolution which are often used to determine the vertical resolving power of P-wave seismic data.

The 'detectable limit' is defined as the minimum layer thickness required to produce an observable seismic reflection (Sheriff, 1991). This is generally taken to be of the order of $\lambda_D/30$, where λ_D is the dominant wavelength of the P wave:

$$\lambda_D = \frac{V_{int}}{f_D}, \qquad (1)$$

f_D is the dominant frequency of the seismic wave, and V_{int} is the interval velocity of the geological layer being considered. The dominant frequency in a seismic record is equivalent to 1/T, where T is the time between adjacent peaks on a display of the seismic data (Figure D-1). Note of course, that detection of a geological layer presupposes a sufficiently strong density and velocity contrast across the layer interfaces.

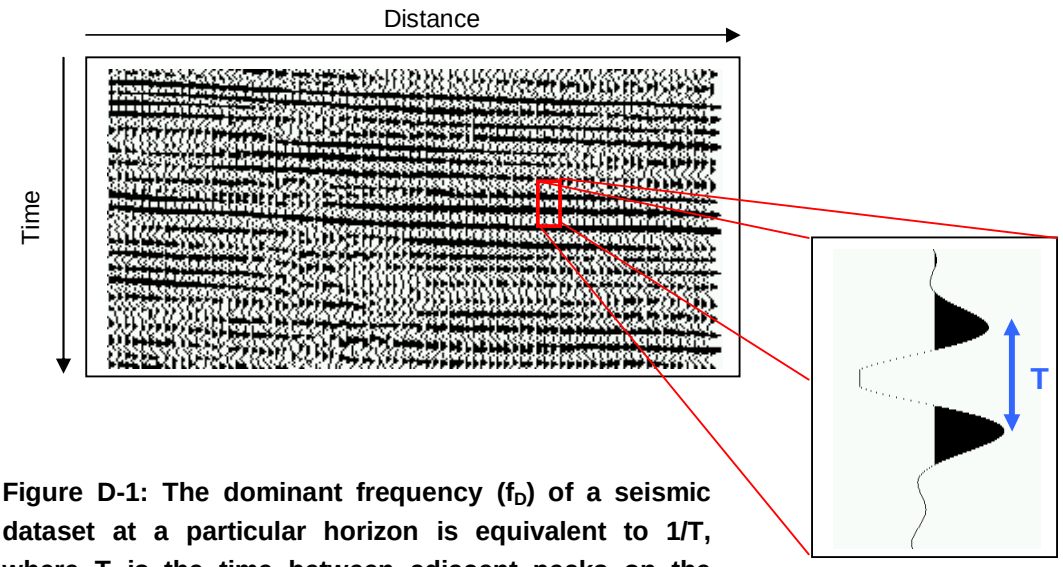

Figure D-1: The dominant frequency (f_D) of a seismic dataset at a particular horizon is equivalent to 1/T, where T is the time between adjacent peaks on the display of the seismic reflection event.

The commonly used 'Rayleigh resolution limit', defined as the minimum separation of discrete seismic reflectors at which one can ascertain more than one interface is present (Sheriff, 1991), is $\lambda_D/4$. The 'Widess limit' is an alternative, and more optimistic definition, which states that two interfaces are resolvable if their separation is greater than or equal to $\lambda_D/8$ (Sheriff, 1991).

Note that these rule-of-thumb measures for P-waves are approximate, and strictly derived for resolution issues relating to layer thickness. Nevertheless, they do provide some indication of the ability of a P-wave section to resolve other geological features (e.g. faults). Obviously these resolution measurements become over-optimistic in the presence of significant noise.

Example

Consider a hypothetical P-wave coal-seismic dataset with a dominant frequency of 150 Hz. If the coal interval P-wave velocity is taken to be 2200 m/s, then the seismic data will have a dominant wavelength (λ_D) of 14.5 m and :

(a) a detectable limit of 0.48 m;
(b) a Rayleigh resolution limit of 3.6 m; and
(c) Widess limit of 1.8 m.

This predicts that the seismic data should be able to detect coal seams with thicknesses greater than approximately 50 cm, and should be able to resolve the top and bottom of a coal seam provided it is thicker than approximately 4 m (or 2 m, depending on which resolution limit is preferred). In terms of defining structural resolution of a seismic dataset, the Rayleigh and Widess resolution limits are often equated to fault throws. For this example then, it might be possible for the data to detect faults with throws down to approximately 2 m.

P versus PS Resolution

According to the above discussion the vertical resolution of a P image is related to the interval velocity of the layer of interest, and the dominant frequency of the data. This also holds true for PS data, although it is necessary to take into account both *Vp*/*Vs* and the dominant P and PS frequencies when determining relevant resolution limits. It can be shown that the PS resolution limit is equivalent to the P resolution limit scaled by:

$$\frac{2}{\left(1+\frac{Vp}{Vs}\right)}\cdot\frac{f_{Dp}}{f_{Dps}}, \qquad (2)$$

where f_{Dp} and f_{Dps} are the dominant frequencies of the P and PS reflection events of interest, respectively. Note that, *Vp*/*Vs* will always be larger than one. Thus, for P and PS images exhibiting the same frequency content, the scale factor in Equation (2) will always be less than one and the PS image will be able to resolve thinner geological layers than the P-wave data. In the case where the dominant frequency of the PS energy is lower than for the corresponding P energy, it is still possible for the PS image to have greater vertical resolution. Based on the scale factor given by Equation (2), the dominant frequency of the PS data need only satisfy:

$$f_{Dps} \geq \frac{2f_{Dp}}{\left(1+\frac{Vp}{Vs}\right)} \qquad (3)$$

for the PS section to better or equal the vertical resolution of the P image.

Example

Consider a hypothetical multi-component coal-seismic dataset. As for the example above, the P-wave data has a dominant frequency of 150 Hz and a coal interval P velocity of 2200 m/s. If the average P-wave to S-wave velocity ratio (*Vp*/*Vs*) in the coal layer is 2.1, and the dominant S frequency is equivalent to that of the P-wave (i.e. 150 Hz), the PS data will have a Rayleigh resolution limit of 2.3 m, compared to 3.6 m for the P data.

If, on the other hand, the PS data have a dominant frequency of only 110Hz, the PS Rayleigh resolution limit is 3.1 m. Despite having a lower dominant frequency than the corresponding P-wave data, the S waves still exhibit greater vertical resolving power. In fact, for a *Vp*/*Vs* of 2.1, the dominant S-wave frequency for this example can drop down to 96 Hz before the PS section will no longer better the P data in terms of vertical resolution.

Previous onshore converted-wave studies in the petroleum sector have, unfortunately, consistently found that PS images have significantly reduced dominant frequencies, resulting in no net wavelength reduction. However, results from this project have provided evidence that high-frequency S-wave energy can be more persistent in the shallow, high-resolution environment, presumably due to the shorter raypath lengths.

Resolution Measurements for Dataset #1

Figure 4.6 shows the final P and PS sections for the first trial area. The average dominant frequency of the P-wave section along the target horizon is 80 Hz. [Note that this is lower than for the P data from the second trial area, despite the fact that the raw field records from the first trial area exhibit greater high-frequency content than the raw records from the second trial area (compare Figures 4.3 and 5.4). This is related to the different processing sequences that have been applied to produce the final sections from the two areas. Namely, deconvolution, which boosts high-frequency content through wavelet compression, has not been used on either the P or PS data from the first trial area.] The average dominant frequency of the corresponding PS target reflection is 65 Hz. The average P- and S-wave seismic velocities in the target coal seam are approximated to be 2200 m/s and 1050 m/s, respectively. Using Equation (1), the dominant wavelength for the P-wave section is 27.5 m. Thus the Rayleigh resolution limit for the P-wave section is approximately 7 m, while the corresponding PS data has a Rayleigh resolution limit of 5.5 m. This confirms what is visually apparent in Figure 4.6, that the PS image has greater vertical resolution than the P section.

Resolution Measurements for Dataset #2

Figure 5.12 shows the final P and PS images from the second trial area. The average dominant frequencies for the P and PS data along the target reflector are 110 Hz and 40 Hz, respectively. The average P- and S-wave interval velocities are approximated to be 2200 m/s and 1050 m/s, respectively. Using Equation (1), the dominant wavelength for the P-wave section is 20 m. This implies that the P-wave section has a Rayleigh resolution limit of 5 m. The corresponding PS Rayleigh resolution limit for this dataset is approximately 9 m. Thus, in this case, the PS image exhibits lower vertical resolving power than the P image. Note however, that the PS stack (Figure 5.12(b)) does image a number of the very small faults observed on the P section, as well as a small feature not detected by the P wave data (Section 5.4.2). Recall that the resolution

measurements discussed here are strictly related to layer thickness, and only give approximate indications of the structural resolving power of a dataset. Obviously there must be other factors coming into play that enable the PS image to provide supplementary information about the sub-surface in this area.

APPENDIX E
CORRELATING P AND PS SEISMIC SECTIONS

The process of correlating P-wave reflectors with PS reflectors from identical sub-surface horizons is critical for interpreting multi-component data. Recall that the slower propagation velocities of S waves mean that a PS wave will arrive at a later time than the P wave from the same geological boundary. If the two-way time of a P reflection event is known (t_P), the approximate arrival time for the corresponding PS reflection (t_{PS}) can be computed via:

$$t_{PS} = \left(\frac{1+\gamma_E}{2} \right) t_P \ , \qquad (1)$$

where γ_E is the effective *Vp*/*Vs* to the horizon of interest. Note that this assumes that the P and PS data have been processed relative to the same datum.

Once reflection events on the P and PS sections have been matched, it has evolved as standard practice in the petroleum sector to visually correlate the seismic images to assist with integrated P/PS interpretation. This involves compressing the time axis of the PS section such that the effective depth extent of the two sections is approximately the same. That is, the maximum time on the PS section represents the same depth as the maximum time on the P section. The PS section times will always be greater because the slower moving S waves take longer to propagate across the same distance.